NASA TECHNICAL NOTE

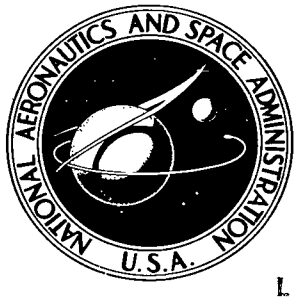

NASA TN D-8448

EXPERIMENTAL INVESTIGATION OF THE VIBRATION CHARACTERISTICS OF A MODEL OF AN ASYMMETRIC MULTIELEMENT SPACE SHUTTLE

Ulysse J. Blanchard, Robert Miserentino, and Sumner A. Leadbetter

Langley Research Center
Hampton, Va. 23665

NATIONAL AERONAUTICS AND SPACE ADMINISTRATION • WASHINGTON, D. C. • SEPTEMBER 1977

1. Report No.	2. Government Accession No.	
NASA TN D-8448		

4. Title and Subtitle	5. Report Date
EXPERIMENTAL INVESTIGATION OF THE VIBRATION CHARACTERISTICS OF A MODEL OF AN ASYMMETRIC MULTIELEMENT SPACE SHUTTLE	September 1977
	6. Performing Organization Code
7. Author(s) Ulysse J. Blanchard, Robert Miserentino, and Sumner A. Leadbetter	8. Performing Organization Report No. L-11211
9. Performing Organization Name and Address NASA Langley Research Center Hampton, VA 23665	10. Work Unit No. 506-17-31-02
	11. Contract or Grant No.
12. Sponsoring Agency Name and Address National Aeronautics and Space Administration Washington, DC 20546	13. Type of Report and Period Covered Technical Note
	14. Sponsoring Agency Code

15. Supplementary Notes

16. Abstract

Experimental results are reported for vibration investigations of a model of the asymmetric multielement space shuttle. Major findings include the influence on overall motions of local deformations in the vicinity of element interfaces, high modal density, low structural damping, and high responsiveness in the crew cabin. Mode frequencies generally increase with decreasing propellant masses and staging of elements.

17. Key Words (Suggested by Author(s))
Structural dynamics
Vibrations
Multielement vehicle modes
Shuttle structural dynamics

18. Distribution Statement
Unclassified - Unlimited

Subject Category 39

19. Security Classif. (of this report)	20. Security Classif. (of this page)	21. No. of Pages	22. Price*
Unclassified	Unclassified	112	$5.50

* For sale by the National Technical Information Service, Springfield, Virginia 22161

CONTENTS

EXPERIMENTAL INVESTIGATION OF THE VIBRATION CHARACTERISTICS OF A MODEL OF AN ASYMMETRIC MULTIELEMENT SPACE SHUTTLE

Ulysse J. Blanchard, Robert Miserentino,
and Sumner A. Leadbetter
Langley Research Center

SUMMARY

Experimental results are reported for vibration investigations of a 1/8-scale dynamic model of an asymmetrical multielement space shuttle. Natural frequencies, mode shapes, and structural damping are presented for modal tests of the model at several flight conditions which include a four-element configuration and a two-element configuration. Results of limited transfer-function tests also are presented.

Major findings include the large influence on overall motions of local deformations in the vicinity of element interstages, high modal density in the low frequency regime, low structural damping, and relatively high responsiveness of the orbiter crew-cabin area to dynamic-force inputs. Resonant frequencies generally increase with decreasing propellant masses and staging of elements.

INTRODUCTION

The structural dynamic characteristics (resonant frequencies, mode shapes, and damping) of launch vehicles must be understood during vehicle development, because these are fundamental to the prevention of aeroelastic and pogo instabilities and for the prediction of dynamic loads during flight operations. Analytical representations used to determine the vehicle structural dynamic characteristics must be verified to insure their adequacy. Test data, to evaluate these analyses, are often obtained from ground vibration tests of prototype flight vehicles relatively late in the development program. A more expedient method for validating analytical representations is the use of dynamically scaled models as described in references 1 and 2. This method has been used with a high degree of success on several launch vehicles, as indicated in references 3 to 7.

Composed of four large elements joined asymmetrically at discrete interstages, this space shuttle vehicle presents several new challenges to the analyst. To assess the analytical modeling procedures and to provide test data to improve the understanding of the static and dynamic behavior of shuttle-type configurations, a 1/8-scale dynamic model of an early shuttle-vehicle concept was designed and fabricated for investigations at the NASA Langley Research Center. Model details are given in reference 8. Results from vibration studies of the 1/8-scale solid rocket booster (SRB) elements are reported in references 9 and 10, of the external tank (ET) element in reference 11, and of the orbiter (Orb.) element in references 12 to 16.

Since the vibration characteristics of the individual elements have been determined separately, it now is necessary to define the overall dynamic characteristics of the mated-vehicle elements for several flight conditions. Therefore, a vibration investigation of mated configurations of the model was conducted to determine the possible effects of interstage geometry, individual element motions, and flexibilities of local structure. Additionally, transfer functions were obtained for one flight condition to determine response sensitivity of critical locations on the vehicle.

This paper describes the model, the model suspension system, and the equipment used to conduct vibration tests of the mated-vehicle model. Vibration data are presented for two mated-vehicle configurations (a four-element configuration and a two-element configuration) at five mass conditions. These conditions represent flight times from lift-off to preorbit. The experimental results and some of their relationships are discussed.

SYMBOLS AND ABBREVIATIONS

A,B,C	mode response
g	gravitational acceleration
M_X	roll moment
q_{max}	maximum dynamic pressure
t	thickness
X,Y,Z	longitudinal, lateral, and vertical axes, respectively
x,y,z	distances along longitudinal, lateral, and vertical axes, respectively

Abbreviations:

AS	mode shape antisymmetric to X-Z plane
ET	external tank
L	left
LH_2	liquid hydrogen
LO_2	liquid oxygen
OMS	orbital maneuvering system
Orb.	orbiter
R	right
S	mode shape symmetric to X-Z plane

SRB solid rocket booster

sta. station, point on longitudinal axis of element

MODEL DESCRIPTION

The complete 1/8-scale dynamic model is shown in figure 1. Nonstructural plastic fairings, which are removed during tests, complete the general contours of the vehicle. The general arrangement and overall dimensions of the mated-vehicle model are shown in figure 2. The assembled model has a lift-off mass of 3975 kg, is 7.3 m long, and consists of four major elements; two solid rocket boosters (SRB's), one external tank (ET), and one orbiter (Orb.). The model design is based on an early space shuttle concept. The model is unpressurized. Design details, including construction drawings, of the model elements are presented in reference 8. Photographs and descriptions of structural features of the model elements are available as follows: SRB's in references 9 and 10, ET in reference 11, and orbiter in references 12 to 16. Brief descriptions of the model elements and details of features or areas of the model pertinent to the present investigation are presented herein.

Scaling

The dynamic scaling relationships between the models (SRB, ET, and Orb.) and the full-scale vehicle are shown in table I. These relationships are obtained from a dimensional analysis of the parameters that affect the dynamic behavior of the structure. Extrapolation from model test data to full-scale vehicle is accomplished by using these scaling relationships directly. It should be noted that some scaling representations have been compromised because of simplifications of the model. The model was designed to retain the significant structural dynamic characteristics although many local structural details were omitted. Detailed structural representation in the elements diminishes in the following order: ET, Orb., and SRB's. Some examples of simplifications are

(1) In most cases constant skin thicknesses were used in lieu of stepped thicknesses or ring-reinforced skins.

(2) Some liberty was taken in representing stiffness characteristics to avoid the expense of modeling exactly scaled small parts.

(3) Aluminum is used in place of steel for the SRB propellant cylinder (noted in table I).

(4) The SRB model consists of a forward skirt, a continuous propellant section, and an aft skirt; whereas, the full-scale version consists of a forward nose cone and skirt, six propellant sections, and an aft propellant segment which also contains the engine section.

As noted in table I, hydrostatic pressure in the model tanks is one-eighth of the full-scale value. For proper scaling of the hydrostatic pressure, the

model would have to be tested in an 8g gravity field. Pressure can have a substantial effect on the vibration frequency of shell modes (ref. 17). Because of this scaling of hydrostatic pressure, resonant shell frequencies of the liquid-containing tank will be lower in relation to overall mode frequencies.

Model Elements

Assembly of the SRB and ET elements is shown in figures 3, 4, and 5. A photograph of the orbiter with the cargo-bay door removed is shown in figure 6. The assembly sequence is as follows: erection and alignment of the SRB's (fig. 3), attachment of the intertank skirt between the SRB's and connection of the LH_2-tank/aft-skirt assembly to the bottom of the intertank skirt (fig. 4), connection of the orbiter to the LH_2 tank (connection points indicated in fig. 4), and finally, attachment of the LO_2 tank atop the intertank skirt as illustrated by figure 5. Sketches of the SRB, ET, and orbiter elements showing the location of pertinent stations, components, element interstages, and overall dimensions are presented in figures 7, 8, and 9. These figures also show the orientation of orthogonal axes for the elements. The axes for the mated-vehicle model are designated in figure 2. Loads, deflections, or accelerations will be discussed in terms of longitudinal, lateral, and vertical directions. Typical gages of structural material for the three elements are presented in table II, and masses of major components are listed in table III.

Solid rocket booster.- The solid rocket booster elements consist of three structural components: a forward skirt, a propellant cylinder, and an aft skirt (see figs. 3, 4, and 7), each made of aluminum. A propellant cylinder is composed of an outer casing, an interior inert cylindrical propellant layer, and two machined end rings for attachment to the skirts. The outer casings are four preformed cylindrical sectors welded together to form a cylinder having two longitudinal welds and one midpoint circumferential weld. The skirts are riveted structures consisting of cylindrical and conical skins covering ring frames, with local reinforcement in the regions of external tank connections and at the support carriage tie-down points (figs. 1 and 3). The reinforcements for improved load distribution are generally skin doublers, built-up frames, or longerons. The support carriage is used only during model reconfiguration operations. Additional structural details are presented in references 8, 9, and 10.

External tank.- The external tank element consists of four major components which are separable as indicated schematically in figure 8: liquid-oxygen (LO_2) tank, intertank skirt, liquid-hydrogen (LH_2) tank, and aft skirt. The LO_2 tank, shown in figure 5, is a monocoque, welded aluminum structure. The intertank skirt, LH_2 tank, and aft skirt (figs. 4 and 5) are ring-frame stiffened cylinders of riveted aluminum construction. The intertank skirt contains the forward ET/SRB interstage connections. The LH_2 tank provides interstage connection points for the orbiter element. (See figs. 4 and 8.) The aft skirt contains the aft ET/SRB interstage connections. Additional structural details are presented in references 8 and 11.

Orbiter.- The orbiter element, shown in figure 6, is primarily a riveted aluminum structure consisting of thin sheets supported by frames, longerons, spars, or ribs. There is a minimum use of intermediate skin stiffeners. The

primary component assemblies, shown schematically in figure 9, are the fuselage/fin, cargo-bay door, wing, and payload simulation. The fuselage component, constructed mainly of sheet aluminum attached to frames and longerons, also has ballast masses installed to represent miscellaneous crew-cabin components and the orbital manuevering system (OMS) modules as shown in figures 6 and 9. The fin structure of the model represents the structure from the fuselage juncture to the center of gravity of the full-scale orbiter fin. A mass attached to the tip of the fin (fig. 9) represents the remaining fin structure. The cargo-bay door (fig. 9) is comprised of seven sheet segments attached to semicircular frames to form a semicylindrical shell. The design of the eight doorframes allows expansion in the longitudinal direction and thereby offers little resistance to fuselage bending but provides resistance to fuselage torsion. The wing panels each consist of sheet aluminum attached to six spars and four ribs. Internal ballast, attached to the spars and ribs, provides the properly scaled wing mass including items such as thermal protection system (TPS) panels, landing gear, and wing flaps. A payload is represented by a simple box beam equipped with cargo-bay attachment brackets. The simulated payload represents the maximum full-scale mass capacity (58.17 kg). Additional structural details of the orbiter element are presented in references 8 and 12 to 16.

Model Element Interstages

An interstage includes all the structure connecting two elements and their attachments. Points of load application and load direction at the Orb./ET and SRB/ET interstages are shown schematically on the ET in figure 10. Photographs of the assembled Orb./ET and SRB/ET interstages are shown in figures 11 and 12, respectively.

Orbiter/external-tank interstages.- The Orb./ET interstages, forward and aft, are located within the liquid-hydrogen tank component of the ET. The forward interstage at ET sta. 3.778 m is a universal joint (fig. 11(a)) which transmits vertical and lateral loads. At the Orb./ET aft interstage (fig. 11(b)) the drag link fitting, extending from ET sta. 5.821 m to 6.242 m, transmits longitudinal and lateral loads. Also, at ET sta. 6.242 m of the same interstage, outboard roll struts connecting the orbiter wing root to the sides of the ET transmit vertical loads and roll moments. Figure 13 shows internal members of the partially fabricated liquid-hydrogen tank and the three major ring frames, located at ET sta. 3.778, 5.821, and 6.242 m, which provide support for the orbiter. The major aft frames at ET sta. 5.821 and 6.242 m are reinforced by internal struts in a triangular pattern to distribute the orbiter load. The tank skin is chemically milled to be thicker on the side adjacent to the orbiter (top skin sector in fig. 13). The area of thick upper skin expands from a small, rectangular area at the forward orbiter connection to cover about one-third of the tank circumference at the aft connection.

Solid-rocket-booster/external-tank interstages.- The SRB/ET interstages, forward and aft, are at the intertank skirt and aft skirt of the ET, respectively. The forward SRB/ET interstage located at ET sta. 2.539 m (fig. 10) is a pin and ball arrangement which transfers vertical, lateral, and longitudinal loads. Photographs in figures 14 and 15 show structural details of the SRB and ET, respectively, in the vicinity of this interstage.

Loads are distributed through the SRB forward skirt by the cantilevered interstage pin, a longeron, a ring frame, and the stepped skin thicknesses shown in figure 14. The longeron has a variable cross-sectional area which is a maximum at the forward interstage frame in the vicinity of the connection pin. (See fig. 14.) Skin thickness varies in this area from the basic 0.102 cm to 0.478 cm at the pin. The interstage frame is formed of back-to-back channel members cylindrically reinforced by a partial inner spacer.

Loads are distributed through the intertank structure of the ET by a self-aligning bearing, a partial longeron, the stepped skin thicknesses, and an internal frame and strut arrangement shown in figure 15. The skin of the intertank skirt increases in thickness near the bearing of the SRB/ET connection. A machined partial longeron transmits load from the skin to both the model suspension lug and the interstage pin bearing. A heavy frame consisting of back-to-back channels is located within the intertank skirt (lower photograph of fig. 15) at the SRB/ET forward interstage. This frame also has a lateral strut extending between the interstage points to distribute the forward SRB loads.

The aft SRB/ET interstage connection (fig. 12(b)) located at ET sta. 6.883 m (fig. 10) is a three-link combination (two parallel and one diagonal) which transmits vertical and lateral loads and roll moments. All strut ends have self-aligning bearings. The aft ET skirt has a major frame (back-to-back channels) at ET sta. 6.883 m and a pair of internal lateral struts which distribute aft SRB loads.

Propellant and Fuel Simulations

Inert solid propellant (UTI-610), manufactured by Chemical Systems Division of United Technologies Corporation, is used to represent various propellant-mass conditions of the SRB's during flight. (See table III.) Cylindrical propellant layers are bonded to the inner walls of six propellant cylinders. The lift-off, mid-boost, and end-boost mass conditions are each represented by a pair of cylinders. The inert propellant material consists of essentially the same binder-curative components as the flight propellant (UTP-3001). In the inert UTI-610 propellant, sodium chloride and ammonium sulfate are substituted for ammonium perchlorate (oxidizer of the flight propellant). Detailed discussions of the viscoelastic properties of the inert propellant are presented in references 9, 10, and 18.

Liquid oxygen, which has a specific gravity of 1.14, was simulated with deionized water in the 1/8-scale tank. Because water has a lower density than liquid oxygen, the dimensions of the LO_2 tank were adjusted to provide scaled LO_2 weight. This adjustment was considered an adequate and manageable representation for the purposes of the test program.

The very low density of liquid hydrogen (specific gravity, 0.071) usually makes precise simulation unnecessary (ref. 7). However, a simulated mass and mass distribution were provided by filling the 1/8-scale liquid-hydrogen tank with polystyrene beads having the desired bulk density (specific gravity, 0.072).

The LO_2 and LH_2 tanks were unpressurized for all of the tests.

TEST APPARATUS AND PROCEDURE

Vibration tests were conducted in the Langley structural dynamics research laboratory (SDRL). The 1/8-scale shuttle model is shown installed in the test facility (fig. 16). The suspension and handling system, data acquisition and reduction system, test procedure, and test conditions are described in the following sections.

Model Suspension and Handling System

Unlike most previous launch-vehicle models, the geometry of the present configuration is asymmetric; as a result, the center of gravity shifts in the X-Z plane (see fig. 2) with variations in fuel load and staging of elements. Vertical suspension of the model is necessary to obtain proper hydroelastic interactions in the ET. Various support concepts and techniques were evaluated, including those described in references 7 and 19, but none of these met all the requirements.

The suspension and handling system developed for the present investigation is shown schematically in figure 17. It is an adaptation of the concept described in reference 20. This system supports the model at the forward SRB/ET interstages, minimizes the effects of the suspension loads on the model, permits the model to assume its own equilibrium pitch attitude at any flight-mass condition, optimizes suspension-system mass, and provides an integral method of reconfiguring the model.

Two air springs, mounted in the model suspension cables, provide vertical isolation. The air springs are rolling-diaphragm vibration isolators connected to large-volume reservoirs. Rigid-body frequencies of the model, suspended on the air springs, are less than 1 Hz. Because the rigid-body frequencies are well below the lowest natural frequencies of the model, the suspension-system effects can be neglected.

The model is lifted off the support carriage to conduct simulated free-flight vibration tests and returned to a secured position (SRB tie-down) on the support carriage to be serviced or reconfigured. In order to accomplish these tasks, the main suspension cable connected to the air springs (see fig. 17) is routed through an arrangement of sheaves to the main hydraulic cylinder used to lift or lower the model. The model is maintained in a vertical attitude during transfer operations by a leveling cable system, indicated by dashed lines in figure 17. The leveling cable is connected to the orbiter nose and routed parallel to the main suspension cable. The leveling cable and the main suspension cable are connected through a floating-hydraulic-cylinder and sheave arrangement which changes the model pitch attitude by varying the distance between two sheaves. During simulated free-flight vibration tests, the leveling cylinder is fully extended to permit the model to assume its equilibrium attitude. The slack leveling cable is then disconnected from the orbiter.

Data Acquisition and Reduction

The data acquisition system provides a means for controlling exciter input force to the model, for monitoring signals from output accelerometers and input-force gages on the model, and for performing onsite data reduction of model signals. A diagram of the data acquisition system network is shown in figure 18. The system diagram is divided into three primary functions: excitation control, response measurement, and data reduction.

Excitation control.- Typical exciter apparatus and installations are shown in figure 19. Electromechanical shakers, which provide variable-frequency, sinusoidal excitation force, were connected to the model by a flexible link. A force gage, used to monitor the input force, is shown installed at the shaker attachment to the model. A servocontrol and oscillator (fig. 18) were used to maintain a constant exciter force. Each exciter was aligned with an orthogonal axis (X, Y, or Z).

Response measurement.- Measurements of model response were obtained by using piezoelectric accelerometers mechanically attached to the model at selected locations. A typical triaxial accelerometer arrangement is shown in the photograph of figure 20(a). Ninety-three fixed-position accelerometers were used to provide overall coverage. Their locations and directions of measurement are illustrated in the isometric sketch of the model in figure 20(b). Most response measurements were made in the z-direction and the least were made in the x-direction. Supplementary response measurements were made with a movable, vacuum-attached accelerometer. Input and response data were recorded in groups of 14 channels. There were 10 prearranged groups which could be selected in any desired sequence.

Data reduction.- Selected analog signals from accelerometers and force gages could be displayed on meters, oscilloscopes, or plotted on a dual-pen recorder for test control information. Additionally, a desk-top calculator/plotter system was programmed to accept, process, and plot normalized-response and phase data during dwell at a selected resonant frequency. Data transfer was accomplished through an interface which multiplexed analog signals sequentially, on command from the computer, through an ac-dc converter, a phase meter, and a coincident-quadrature (co-quad) analyzer to the calculator/plotter. Isometric sketches of the resonant mode shape were automatically plotted.

Modes of interest were identified by either the co-quad method, discussed in references 21 and 22, or the Kennedy Pancu (phase-plane) method discussed in references 23, 24, and 25. Some logarithmic-decrement damping data were taken, but structural damping was determined from the phase-plane diagrams. For selected modes, mode-shape plots were made from the measured response data. Visual interpretation was enhanced by convenient scaling of the data.

Test Procedure

Two vibration-test procedures were used during the investigation, modal tests and transfer-function tests. Modal tests were conducted for all the

flight conditions of the investigation, whereas transfer-function tests were conducted at lift-off only.

Modal tests.- The modal tests were conducted by slowly sweeping the excitation from 10 Hz to 130 Hz. The maximum frequency, 130 Hz, is equivalent to approximately 16 Hz for the full-scale vehicle. Responses of transducers located on each of the model elements were recorded as plots of the variation in the quadrature component of the output acceleration (out of phase with respect to input force) as a function of frequency. Typical co-quad plots are shown in figure 21. Resonant frequencies were identified by use of these plots. As required, phase-plane plots of the response data were made over a small frequency range in the vicinity of selected resonant peaks as shown in figure 22. In this case, the quadrature component and the frequency are plotted as functions of the coincident component of the output acceleration referred to input force. The phase-plane data were used to evaluate modal purity, to more precisely determine resonant frequencies of closely spaced modes, to determine modal amplitude, and to determine damping (ref. 22). The mode identification and evaluation process is illustrated by the responses labeled A, B, and C in figures 21 and 22. The responses labeled A and B are examples of interactive modes with closely spaced frequencies (coupled responses). The response labeled C is relatively uncoupled and due primarily to an SRB element mode.

This general test procedure was repeated for several exciter locations and directions to excite both symmetric and antisymmetric modes. The exciter configurations utilized for the mated-vehicle-model vibration tests are listed in table IV. In general, three techniques of excitation were used; one shaker, two shakers in phase, or two shakers 180° out of phase. Constant input-force levels in the range of 1 to 22 N were used during these tests.

Normalized acceleration vector plots were obtained during dwell at each resonant frequency determined from the co-quad and phase-plane data. The acceleration vectors were plotted on a simplified isometric sketch of the model (fig. 20) using the desk-top-calculator program. These plots illustrate the characteristic motions.

Transfer-function tests.- Transfer-function tests were conducted by slowly sweeping the excitation frequency through the range of 10 to 100 Hz and recording responses at four selected model locations. Sinusoidal input force was applied in areas considered to be potential sources of excitation during flight of the full-scale vehicle; these sources are the orbiter main engines, orbiter wings, and booster engines. Single- and dual-shaker configurations, similar to those of the modal tests (table IV), were used to excite symmetric and antisymmetric responses. Eleven exciter configurations were used. Transfer functions were measured at locations considered to be important with respect to the installation of navigation and flight control equipment; these are forward bulkhead of orbiter cabin, rear bulkhead of orbiter payload compartment, and both SRB aft interstages. The measured responses were plotted as the variation in the quadrature component of the output acceleration as a function of frequency.

Test conditions.- Vibration tests of the mated-vehicle model were conducted for five conditions representing various stages of space shuttle flight from lift-off to orbit insertion. The test conditions are shown in table V. A four-

element configuration consisting of two SRB's, the ET, and the orbiter was investigated at three mass conditions: lift-off, mid-boost (q_{max}), and end-boost (before SRB separation). A two-element configuration consisting of the ET and the orbiter was investigated at two mass conditions: end-boost (after SRB separation) and end-burn (before ET jettison). The corresponding masses of the fuel and the element structure and the total mass for each test condition are also shown in table V. Modal tests were conducted at each mass condition and transfer-function tests were conducted at lift-off condition.

RESULTS AND DISCUSSION

Modal Data

The modal data (natural frequencies, mode shapes, and damping) obtained during vibration tests are presented. The natural frequencies and mode shapes are presented for the five flight conditions of the investigation. Modal-density and structural-damping data are presented for typical conditions.

Natural frequencies and mode shapes.- The natural frequencies and mode shapes are presented for three flight conditions of the mated four-element configuration consisting of two SRB's, the ET, and the orbiter and for two flight conditions of the two-element configuration consisting of the ET and the orbiter. Selected modes are discussed in the following sections. The remaining modes are illustrated in the appendix.

Lift-off: The natural frequencies measured for lift-off mass are presented in table VI. Also included in the table are the associated exciter configurations (input code) and brief descriptions of the mode shapes obtained, with applicable figure references. The descriptions are based on the more prominent characteristics of the isometric plots of normalized acceleration obtained at each resonant frequency during the tests. Figure 23 presents a sample of these plots for selected symmetric and antisymmetric modes. The exciter configurations used to obtain each mode are indicated by large arrows. The first mode identified during sinusoidal tests of this configuration (mode 1) at 14.03 Hz, shown in figure 23(a), is an antisymmetric mode in which three of the elements (two SRB's and the ET) are rotating as rigid bodies in a coordinated manner about their longitudinal axes much as a train of meshed gears (gear-train rotation). The orbiter motion is a unitary rotation in phase with the ET. This mode is probably unique for this type of multielement configuration in that it is largely the result of local distortions in the vicinity of the element interfaces.

The first symmetric mode (mode 3) at 17.50 Hz, shown in figure 23(b), is the first bending mode of the ET in the pitch plane (X-Z) with rigid-body pitching of the SRB's and the orbiter in phase with the ET. The next mode (mode 4) at 17.86 Hz, shown in figure 23(c), is also a symmetric mode and is unique in that the SRB's are essentially counterrotating about a longitudinal node line with simultaneous vertical translation (X-Z plane) of the ET and orbiter between the SRB's. The overall motion is similar to that of a double rack-and-pinion gear mechanism. There is also some bending distortion of the SRB's and the ET. The antisymmetric mode (mode 7) at 24.37 Hz, shown in figure 23(d), has out-of-

phase pitching of the SRB's and the first torsion mode of the ET. Combined roll and yaw motion of the orbiter results from the ET node-line location between the fore and aft orbiter connections. The first longitudinal mode (mode 8) at 25.32 Hz, shown in figure 23(e), is characterized primarily by inphase longitudinal translation of the two SRB's and opposing longitudinal translation of the ET and the orbiter. There is considerable pitching of the orbiter in the X-Z plane.

Many of the modes involve relative rotations or axial translations between the mated elements about their interfaces and are probably accentuated by local distortions of adjacent structure. Significant local deformations in the vicinity of element interfaces would suggest the criticalness of their influence on overall motions. Such local deformations are illustrated by modes 8, 12, 23, and 29 shown in figures 23(e), 23(f), 23(h), and 23(j), respectively. Several modes, such as mode 8 in figure 23(e), exhibit large pitching motions of the orbiter nose about the aft interstage connection. A lateral (y-direction) transducer, located on the right side of the ET on the forward Orb./ET interstage ring frame, indicates a significant deformation in the local frame area. By use of a movable transducer, a brief survey verified circumferential deformation of the ET ring frame occurring coincidentally with the forward orbiter motions. Indications of similar local deformations near SRB/ET interstages are demonstrated by the modes shown in figures 23(f), 23(h), and 23(j). These modes are generally characterized by out-of-phase yaw or bending of the SRB's with the ET and orbiter relatively stationary. Large lateral (y-direction) motions are indicated by transducers at the forward and aft interstages of the SRB's relative to similar motions of the ET structure at the corresponding points. This suggests considerable distortion of the SRB skirt structure near the interstage connections.

There was evidence of shell modes in the liquid-oxygen tank participating in the response at several lift-off longitudinal or transverse modes. (See, for example, fig. 23(g).) The shell modes are indicated by the vector patterns in the mode-shape plots of transducers installed on the liquid-oxygen tank. In some cases, shell responses tended to mask overall mode deflections. Results of separate liquid-oxygen-tank shell mode studies verified the existence of many shell modes within the frequency range of this investigation.

Mid-boost (maximum dynamic pressure): The measured natural frequencies and predominant modal characteristics are summarized in table VII for the mid-boost (maximum dynamic pressure q) mass condition. (See table V.) The tests were conducted primarily below 100 Hz. The mode at 140.88 Hz (bottom of table VII) was obtained specifically to provide a data point for SRB first torsion. Generally, the mode characteristics at the mid-boost condition are the same as at the lift-off condition but at higher frequencies because of reductions in fuel mass. For comparison with the lift-off condition, some of the transverse and longitudinal mode shapes at mid-boost are shown in figure 24. The symmetric mode at 15.84 Hz (mode 2), shown in figure 24(a), is predominantly the opposing lateral displacement (and bending) of the SRB's. A secondary general motion noted is some counterrotation of the SRB's with coincidental vertical displacement (like a rigid body) of the ET and orbiter.

The mode at 19.39 Hz (mode 4), shown in figure 24(b), is the y-direction first bending mode of the ET with synchronous rigid-body yawing of the SRB's

and the orbiter. The z-direction first bending mode of the ET for the mid-boost condition occurs at 19.90 Hz (mode 5, shown in fig. 24(c)). There is a shift in node lines of the elements for this mode when compared with the same mode at the lift-off condition (mode 3, fig. 23(b)). The first longitudinal mode (mode 8), first ET torsion mode (mode 9), and the symmetric y-direction first bending mode of the SRB's (mode 23) at the mid-boost condition (shown in figs. 24(d), 24(e), and 24(f), respectively) are quite similar to the same modes at lift-off (fig. 23).

End-boost (before solid-rocket-booster separation): The measured natural frequencies and predominant mode characteristics are summarized in table VIII for the end-boost (before SRB separation) mass condition. Selected mode shapes are illustrated in figure 25. The z-direction first bending mode of the ET (mode 2) is shown in figure 25(a) for comparison with the corresponding mode at the previous test conditions of the four-element configuration. The mode shapes shown in figures 25(b), 25(c), and 25(d) are presented for illustration of a difficulty encountered occasionally during this investigation. There is coupling between an SRB lateral mode (mode 5, table VIII and fig. 25(b)), a vehicle longitudinal mode (mode 6, table VIII and fig. 25(c)), and an orbiter pitching mode (mode 8, table VIII and fig. 25(d)). In this frequency range it was not possible to clearly isolate the longitudinal modes and orbiter pitching modes (figs. 25(c) and 25(d)).

Mode characteristics at the end-boost condition are similar to those obtained for the two previous test conditions (lift-off and mid-boost), and the resonances occur typically at higher frequencies as propellant and fuel mass of the SRB's and ET decrease (orbiter mass remains constant). The resonant frequency for the principal modes of the elements generally increases with decrease in fuel mass of the element for the three flight conditions of the four-element configuration. Table V shows that the SRB mass decreases more rapidly than does the ET mass for these three flight conditions. This explains the more rapid increase in mode frequencies of the SRB when compared to the ET for this range of test conditions. (See tables VI, VII, and VIII.) It is also consistent that mode frequencies of the orbiter are relatively unchanged.

End-boost (after solid-rocket-booster separation): The measured natural frequencies and predominant mode characteristics summarized in table IX are for the two-element configuration (ET and Orb.) at the mass condition just after staging of the solid-rocket boosters (after SRB separation). The first mode for this condition at 21.76 Hz (mode 1), shown in figure 26(a), is the first bending mode of the ET in the X-Z plane (symmetric). The mode is quite similar to the corresponding mode at lift-off (see fig. 23(b)) and includes the large orbiter pitch rotation. There is evidence of distortion or bulging (out-of-phase y-direction vectors) of the ET frame at the orbiter forward interstage which coincides with the orbiter pitching motion. This local distortion is even more prominent for the first longitudinal mode at 33.00 Hz (mode 3) shown in figure 26(b). Orbiter first bending and orbiter-wing first bending occur at 45.28 Hz and 50.08 Hz, respectively. (See figs. 26(c) and 26(d).) These mated orbiter modes are in good agreement with the corresponding modes determined during orbiter tests (ref. 16). Several antisymmetric rotational modes with coupled torsional and beam-bending deflections are evident. (See, for example, figs. 26(e) and 26(f).) In many of these rotational modes, deflections of

the forward portion of the ET are greater than deflections of the aft portion where the orbiter is attached.

End-burn (before external-tank jettison): The measured natural frequencies and predominant mode characteristics determined for the before-ET-jettison condition (empty LO_2 and LH_2 tanks) are summarized in table X. Sample isometric mode-shape plots are shown in figure 27. The first mode at 32.13 Hz (mode 1) for this condition, shown in figure 27(a), shows large deflections (like a cantilever beam) of the forward portion of the ET and opposing pitch motion of the orbiter. This deflection characteristic also appears in several lateral and rotational modes (figs. 27(b) and 27(f)). The first bending modes of the orbiter fuselage (fig. 27(c)) and the orbiter wing (fig. 27(d)) are in good agreement with previously discussed test conditions. The first bending mode of the ET in the X-Z plane occurs at 63.16 Hz (mode 11), shown in figure 27(e). The five symmetric modes, 42.91 Hz to 63.16 Hz (table X, figs. 27(c) and 27(e)), show some longitudinal motion of the ET with opposing motion of either the orbiter, orbiter payload, or the orbiter vertical fin.

Frequency variation with flight condition.- The trend of mode frequency with change in vehicle mass (flight time) is shown in figure 28. The frequency at which a characteristic mode of an element or elements was first noted is plotted for each test condition of the simulated flight (1 to 5 on the abscissa). Conditions 1 to 5 are mated-vehicle-model conditions. Also shown for comparison is condition 6 which is the orbiter only case (ref. 16). Modes involving particular elements of the model (SRB's, ET, and orbiter) are shown in figures 28(a) and 28(b). Figure 28(c) shows multielement rotation and longitudinal modes which are unique for this mated configuration.

The SRB mode frequencies (fig. 28(a)) increase more rapidly relative to the other elements due to the propellant depletion schedule for the four-element configuration during boost (conditions 1, 2, and 3). The SRB propellant mass decreases most rapidly during this period of flight. The ET mode frequencies (fig. 28(b)) increase slightly to condition 3. The ET first torsion frequency increases substantially at burnout (condition 3) and at separation (condition 4) of the SRB's. At condition 5, the ET liquid-oxygen and liquid-hydrogen tanks are empty and the first bending mode frequencies increase by a factor of nearly 3 over frequencies at condition 4. Frequencies for the orbiter modes remained nearly constant throughout the range of conditions investigated (orbiter mass is constant).

In general, all the rotational and longitudinal modes presented in figure 28(c) show moderate increase in frequency for conditions 1 to 3. After separation of the SRB's (conditions 4 and 5), modes for rack-and-pinion motion and orbiter roll are not evident, whereas a mode for gear-train motion is evident at conditions 4 and 5 (two-element configuration) at about twice the frequency for the first three conditions. The first longitudinal mode frequency increases significantly with the empty ET (condition 5). An orbiter pitching-mode frequency remains constant over the entire range of conditions. These modes (fig. 28(c)) are closely grouped with near superposition in some cases. They are generally within a 15-Hz bandwidth (15 to 30 Hz) which also is in the same frequency range as many of the ET modes (fig. 28(b)). The small frequency separation of these

modes contributes to the difficulty of isolating the individual modes during vibration tests.

Results of the vibration tests indicate an effect of local flexibilities which unpublished static-load tests help to explain. The static-load tests were conducted to define the flexibility characteristics of local structure in the vicinity of the interstages of the SRB and ET elements. Some pertinent results should be mentioned here. It was determined that the deformation of structure surrounding the interstages, and not of the attachment fittings themselves, is the primary source of flexibilities which influence coupled vibration motions of the elements. Furthermore, the local distortion flexibility of the ET at the forward ET/Orb. interstage in the X-Z plane (312.7 nm/N) is the largest of all the interstage areas; whereas, the local distortion of the ET at the aft ET/Orb. interstage is comparatively very small (20.8 nm/N). As previously shown, the load-carrying frames of the ET at the aft interstage are reinforced (stiffened) by internal beams; whereas, the forward interstage frame has no such reinforcement. (See fig. 13.) Therefore, the combination of a soft supporting structure at the forward orbiter interstage with much stiffer support at the aft interstage amplifies pitching motions of the orbiter, as noted in vibration test results. (See figs. 23(e), 24(d), 25(d), 26(a), 26(b), and 27(a).)

Maximum distortions of the local structure in the vicinity of the SRB interstages are about half those of the ET. The largest distortion coefficient determined for the SRB was at the forward interstage in the X-Y plane (156.6 nm/N). This value is about four times that for the ET structure at the same interstage. An example of the influence of this flexibility is illustrated by mode 12 (table VI and fig. 23(f)) in which vibration measurements indicate large out-of-phase lateral displacement of the forward ends of the SRB's relative to indicated displacement of adjacent ET structure.

The interdependence of these results from static and vibration tests substantiate the importance of accurate determination of local flexibilities near element interstages. The local distortion flexibilities of the interstage areas could be critical to the definition and understanding of lateral, longitudinal, and rotational vibration modes of the mated shuttle model.

Modal density and structural damping.- Comparative mode-frequency spectrums and damping factors are shown in figures 29 and 30 for flight conditions ranging from lift-off through post ET jettison. Data are shown for three test conditions of the present investigation, for which damping data are available, and also for the orbiter-only case reported in reference 16. Modal density, which is shown in figure 29, is considered high, particularly at the low frequencies and for the four-element configuration. In general, modal density diminishes as the vehicle is staged from lift-off through post ET jettison.

Structural damping values are presented in figure 30 for the same four test conditions shown for modal-density comparisons (fig. 29). The damping factors measured over the range of test frequencies vary over a broad band from about 0.005 to 0.03. The data generally indicate that damping increases slightly with increase in frequency. Spot checks of the damping for the two test conditions not shown, mid-boost and end-boost, indicated that values of the damping factor are within the same range.

Transfer-Function Data

Vibration transfer functions were obtained on the model at the lift-off condition (four-element configuration). The relative response sensitivity of some critical locations on the mated vehicle was evaluated for excitations at places where dynamic-force inputs might be expected. Figure 31 shows comparisons of all responses measured at three locations of the model. Figure 32 shows the effects of the direction and location of the excitation on magnitude distributions of these responses.

Figure 31 shows the responses measured at response locations (a), (b), and (c), shown in the model sketch, for excitations applied at points 1, 2-2, and 3-3 in the model sketch. Results of measurements at a fourth location (d), which are not presented in the figure, are the same as for location (c). The responses, measured in the x-, y-, and z-directions (see shading code in model sketch) for excitations in the x-, y-, and z-directions, respectively, are presented as spectral curves in terms of gravitational units per newton (g units/N) of input force plotted against exciter frequency for each of the response locations of interest; (a) crew cabin, (b) payload aft compartment, and (c) the left SRB aft interstage. The curves are point-to-point fairings of the averages of the peak response levels in adjacent 0.5-Hz bandwidths. The orbiter cabin location is the most responsive, whereas the SRB aft interstage locations are the least responsive to the inputs.

The magnitude-distribution curves (fig. 32) have an ordinate which is a function of the abscissa, with the ordinate given as the percent of the peaks that exceed the magnitude of the peak response. Magnitude distribution curves are shown for response measurements in the same direction as the direction of excitation at the four locations of interest. The largest responses occur most often in the z-direction, and the smallest responses occur most often in the x-direction. Figure 32(b) shows distribution curves for only z-direction responses resulting from z-direction excitations. Only peaks above 0.04 g units/N are included. These responses are shown separately for each of the three excitation points: engine, wings, and SRB's. The largest responses occur most often for excitation at the wing tips, and the smallest responses occur most often for excitation at the SRB skirts.

CONCLUDING REMARKS

Vibration characteristics of a 1/8-scale dynamic model of a preliminary design for the multielement space shuttle vehicle have been determined experimentally for frequencies up to 130 Hz (about 16 Hz full scale). Vibration tests of the mated-vehicle model were conducted for five flight conditions representing stages from lift-off to before ET jettison. This test envelope included four-element (two SRB's, one ET, and one Orb.) and two-element (ET and Orb.) configurations. Experimental results obtained support the following conclusions:

1. Local deformations in the region of interstages are critical to many complex modes of the model.

2. Modal density is high in the low-frequency range, but is reduced by decreasing propellant masses and staging of elements.

3. In all cases the structural damping was found to be below 0.03.

4. Transfer-function data show that the cabin area of the orbiter element is highly responsive.

5. During boost (lift-off to SRB burnout), frequencies of the principal modes associated with the SRB elements increase more rapidly than those of the other elements.

6. Frequencies of principal modes associated with the ET element increase very rapidly after SRB separation.

7. Frequencies of principal modes associated with the orbiter element are nearly constant for all flight conditions.

8. Liquid-oxygen-tank shell responses and the close frequency spacing of modes make the isolation and definition of some modes difficult.

Langley Research Center
National Aeronautics and Space Administration
Hampton, VA 23665
July 13, 1977

APPENDIX

SUPPLEMENTARY MODE SHAPES

This appendix presents isometric sketches of the mode shapes obtained during vibration tests of the 1/8-scale shuttle model but not shown or discussed in the body of the paper. These mode shapes are presented without discussion to supplement the abbreviated mode descriptions in tables VI, VII, VIII, IX, and X. The supplementary mode shapes presented in the following figures are in the same order as are the discussions of results for the five test conditions in the section "Modal Data."

REFERENCES

1. Runyan, H. L.; Morgan, H. G.; and Mixson, J. S.: Use of Dynamic Models in Launch-Vehicle Development. AGARD Rep. 479, May 1964.

2. Guyett, P. R.: The Use of Flexible Models in Aerospace Engineering. Tech. Rep. No. 66335, British R.A.E., Nov. 1966.

3. Mixson, John S.; and Catherine, John J.: Comparison of Experimental Vibration Characteristics Obtained From a 1/5-Scale Model and From a Full-Scale Saturn SA-1. NASA TN D-2215, 1964.

4. Jaszlics, Ivan J.; and Morosow, George: Dynamic Testing of a 20% Scale Model of the Titan III. AIAA Symposium on Structural Dynamics and Aeroelasticity, Aug.-Sept. 1965, pp. 477-485.

5. Leadbetter, S. A.; and Raney, J. P.: Model Studies of the Dynamics of Launch Vehicles. J. Spacecraft & Rockets, vol. 3, no. 6, June 1966, pp. 936-938.

6. Pinson, Larry D.; and Leonard, H. Wayne: Longitudinal Vibration Characteristics of 1/10-Scale Apollo/Saturn V Replica Model. NASA TN D-5159, 1969.

7. Grimes, P. J.; McTigue, L. D.; Riley, G. F.; and Tilden, D. I.: Advancements in Structural Dynamic Technology Resulting From Saturn V Programs. Vol. II. NASA CR-1540, 1970.

8. Grumman Aerospace Corp.: Design of a Space Shuttle Structural Dynamics Model. NASA CR-112205, [1972].

9. Levy, A.; Zalesak, J.; Bernstein, M.; and Mason, P. W.: Development of Technology for Modeling of a 1/8-Scale Dynamic Model of the Shuttle Solid Rocket Booster (SRB). NASA CR-132492, 1974.

10. Leadbetter, Sumner A.; Stephens, Wendell B.; Sewall, John L.; Majka, Joe W.; and Barrett, Jack R.: Vibration Characteristics of 1/8-Scale Dynamic Models of the Space-Shuttle Solid-Rocket Boosters. NASA TN D-8158, 1976.

11. Bernstein, M.; Coppolino, R.; Zalesak, J.; and Mason, P. W.: Development of Technology for Fluid-Structure Interaction Modeling of a 1/8-Scale Dynamic Model of the Shuttle External Tank (ET). Vols. I and II. NASA CR-132549, 1974.

12. Mason, P. W.; Harris, H. G.; Zalesak, J.; and Bernstein, M.: Analytical and Experimental Investigation of a 1/8-Scale Dynamic Model of the Shuttle Orbiter. Volume I - Summary Report. NASA CR-132488, 1974.

13. Mason, P. W.; Harris, H. G.; Zalesak, J.; and Bernstein, M.: Analytical and Experimental Investigation of a 1/8-Scale Dynamic Model of the Shuttle Orbiter. Volume II - Technical Report. NASA CR-132489, 1974.

14. Mason, P. W.; Harris, H. G.; Zalesak, J.; and Bernstein, M.: Analytical and Experimental Investigation of a 1/8-Scale Dynamic Model of the Shuttle Orbiter. Volume IIIA - Supporting Data. NASA CR-132490, 1974.

15. Mason, P. W.; Harris, H. G.; Zalesak, J.; and Bernstein, M.: Analytical and Experimental Investigation of a 1/8-Scale Dynamic Model of the Shuttle Orbiter. Volume IIIB - Supporting Data. NASA CR-132491, 1974.

16. Pinson, Larry D., Coordinator: Analytical and Experimental Vibration Studies of a 1/8-Scale Shuttle Orbiter. NASA TN D-7964, 1975.

17. Mixson, John S.; and Herr, Robert W.: An Investigation of the Vibration Characteristics of Pressurized Thin-Walled Circular Cylinders Partly Filled With Liquid. NASA TR R-145, 1962.

18. Hufferd, William L.: Measured Properties of Propellant for Solid Rocket Booster of One-Eighth Scale Dynamic Shuttle Model. NASA CR-144938, [1976].

19. Herr, Robert W.: Some Cable Suspension Systems and Their Effects on the Flexural Frequencies of Slender Aerospace Structures. NASA TN D-7693, 1974.

20. Peele, Ellwood L.; Thompson, William M., Jr.; and Pusey, Christine G.: A Theoretical and Experimental Investigation of the Three-Dimensional Vibration Characteristics of a Scaled Model of an Asymmetrical Launch Vehicle. NASA TN D-4707, 1968.

21. Keller, Anton C.: Vector Component Techniques: A Modern Way To Measure Modes. Sound & Vib., vol. 3, no. 3, Mar. 1969, pp. 18-26.

22. Salyer, Robert A.; Jung, Ed J., Jr.; Huggins, Stacy L.; and Stephens, Barry L.: An Automatic Data System for Vibration Model Tuning and Evaluation. NASA TN D-7945, 1975.

23. Schoenster, James A.: Measured and Calculated Vibration Properties of Ring-Stiffened Honeycomb Cylinders. NASA TN D-6090, 1971.

24. Schoenster, James A; and Taylor, Nancy L.: A Sinusoidal-Vibration Analysis Program for Experimental Data. NASA TM X-2789, 1973.

25. Turner, Lloyd, J., Jr.: An Analytical Investigation of a Vector Technique for Determining Normal Mode Amplitudes From Vibration Data. M. S. Thesis, Virginia Polytech. Inst., 1968.

TABLE I.- PERTINENT SCALING RELATIONS FOR 1/8-SCALE SHUTTLE MODEL

[Subscripts: f denotes full-scale vehicle; m denotes 1/8-scale model]

Physical quantity	Magnitude		
	Solid-rocket booster		External tank and orbiter
	Propellant	Structure (a)	
Length or displacement, L	$8L_m = L_f$	$8L_m = L_f$	$8L_m = L_f$
Poisson's ratio, μ	$\mu_m = \mu_f$	$3\mu_m = \mu_f$	$\mu_m = \mu_f$
Mass density, ρ	$\rho_m = \rho_f$	$3\rho_m = \rho_f$	$\rho_m = \rho_f$
Modulus of elasticity, E	$E_m = E_f$	$3E_m = E_f$	$E_m = E_f$
Strain, ε	$\varepsilon_m = \varepsilon_f$	$3\varepsilon_m = \varepsilon_f$	$\varepsilon_m = \varepsilon_f$
Area, A	$8^2A_m = A_f$	$8^2A_m = 3A_f$	$8^2A_m = A_f$
Area moment of inertia, I	$8^4I_m = I_f$	$8^4I_m = 3I_f$	$8^4I_m = I_f$
Mass moment of inertia, I'	$8^5I'_m = I'_f$	$8^5I'_m = 3I'_f$	$8^5I'_m = I'_f$
Volume, V	$8^3V_m = V_f$	$8^3V_m = 3V_f$	$8^3V_m = V_f$
Mass	$8^3\rho_mV_m = \rho_fV_f$	$8^3\rho_mV_m = \rho_fV_f$	$8^3\rho_mV_m \approx \rho_fV_f$
Stress, σ	$\sigma_m = \sigma_f$	$3\sigma_m = \sigma_f$	$\sigma_m = \sigma_f$
Force, F	$8^2F_m = F_f$	$8^2F_m = F_f$	$8^2F_m = F_f$
Hydrostatic pressure, p	----------	----------	$8p_m = p_f$
Longitudinal stiffness, EA	$8^2E_mA_m = E_fA_f$	$8^2E_mA_m = E_fA_f$	$8^2E_mA_m \approx E_fA_f$
Bending stiffness, EI	$8^4E_mI_m = E_fI_f$	$8^4E_mI_m = E_fI_f$	$8^4E_mI_m = E_fI_f$
Torsional stiffness, [b]GJ	$8^4G_mJ_m = G_fJ_f$	$8^4G_mJ_m = G_fJ_f$	$8^4G_mJ_m \approx G_fJ_f$
Acceleration, a	$a_m = 8a_f$	$a_m = 8a_f$	$a_m = 8a_f$
Frequency, f	$f_m = 8f_f$	$f_m = 8f_f$	$f_m = 8f_f$

[a]Aluminum used in model to represent steel in full scale.
[b]G, modulus of elasticity in shear; J, polar moment of inertia.

TABLE II.- TYPICAL GAGES OF MATERIAL IN COMPONENTS OF 1/8-SCALE MODEL ELEMENTS

Element component	Thickness, cm
Solid rocket booster	
Propellant cylinder casing	0.476
Forward skirt:	
Frames	0.1016
Skin	0.1016
Aft skirt:	
Frame	0.157
Longerons	0.157
Skin	0.157
External tank	
Liquid-oxygen tank:	
Aft dome	0.0406
Aft dome (apex)	0.1016
Cylindrical and conical shell	0.0508
Upper dome	0.0635
Intertank skirt:	
Forward frame	0.1016
Interface frames	0.1016
Aft frame	0.1016
Skin	0.0635
Lateral strut	0.1016
Liquid-hydrogen tank:	
Forward and aft dome	0.0508
Stiffener frames (angles)	0.1016
Load frames (channels)	0.1016
Skin	0.0406

TABLE II.- Concluded

Element component	Thickness, cm
External tank	
Aft ET skirt:	
Stiffener frame	0.1016
Aft frames	0.1016
Skin	0.0508
Orbiter	
Fuselage:	
Bulkheads	0.1016
Frames	0.3175
Longerons (door)	0.0813
Keel beam (web)	0.1016
Wing deck (carry through)	0.0508
Engine-thrust deck	0.0406
Engine-thrust struts	0.0813
Skin -	
Sides	0.0508
Bottom	0.0635
Fin:	
Spars (web)	0.0813
Closure rib (web)	0.0813
Skin	0.0508
Cargo door:	
Frames	0.0813
Skin	0.0406
Wings:	
Spars	0.0813
Ribs	0.0813
Skin	0.0508

TABLE III.- MASSES OF COMPONENTS OF 1/8-SCALE SHUTTLE MODEL ELEMENTS

Component	Mass, kg
Solid rocket booster	
Propellant-cylinder assembly	78.24
Propellant, lift-off (17-cm-thick layer)	1066.17
Propellant, mid-boost (9-cm-thick layer)	698.65
Propellant, end-boost (2-cm-thick layer)	169.53
Forward-skirt assembly	6.99
Aft-skirt assembly	15.79
External tank	
Liquid-oxygen tank	14.33
Intertank skirt	16.33
Liquid-hydrogen tank and external-tank aft skirt, combined	49.90
Orbiter	
Fuselage and fin	44.40
Cargo-bay door	5.28
Wing panels (2), including ballast	29.14
Payload unit	58.17
Cabin ballast	26.65
OMS ballast	23.31
Fin ballast	2.72

TABLE IV.- EXCITER CONFIGURATIONS FOR VIBRATION OF 1/8-SCALE SHUTTLE MODEL

Input code	Exciter arrangement				
	Exciter direction	Number of exciters	Phase relation, deg	Model element	Element station, m
A	x	2	0	SRB skirts (2)	5.535
B	↓	2	180	SRB skirts (2)	5.535
C	↓	1		Orb. engine	4.572
D	↓	2	0	Orb. wing tips	4.115
E	↓	2	180	Orb. wing tips	4.115
F	y	1		SRB (1)	1.130
G	y (M_X)	2	180	SRB (1)	1.130
H	y	1		ET	2.129
I	↓	1		Orb. nose	1.189
J	↓	1		Orb. engine	4.572
K	z	2	0	SRB's (2)	1.130
L	↓	2	180	↓	1.130
M	↓	2	180	↓	4.872
N	↓	1		ET	2.129
O	↓	2	0	↓	2.129
P	↓	2	180	↓	2.129
Q	↓	1		Orb. nose	1.189
R	↓	2	0	Orb. wing tips	4.115
S	↓	2	180	Orb. wing tips	4.115
T	↓	1		Orb. engine	4.572
U	↓	2	180	Orb. nose	1.189

TABLE V.- MAJOR FUEL AND STRUCTURAL MASSES FOR 1/8-SCALE SHUTTLE MODEL TEST CONDITIONS

Model configuration	Test condition	Fuel mass, kg				Structure mass, kg			Total mass, kg
		SRB-L	SRB-R	LO_2	LH_2	SRB's (2)	ET	Orbiter	
Four-element	Lift-off	1067.3	1065.0	1170.3	199.6	201.8	80.7	190.0	3974.7
	Mid-boost (q_{max})	702.2	695.4	1049.6	174.6	201.8	80.7	190.0	3094.3
	End-boost (before SRB separation)	167.8	171.5	900.8	152.0	201.8	80.7	190.0	1864.6
Two-element	End-boost (after SRB separation)	0	0	900.8	152.0	0	80.7	190.0	1323.5
	End-burn (before ET jettison)	0	0	0	0	0	80.7	190.0	270.7

TABLE VI.- SUMMARY OF MEASURED VIBRATION MODES OF THE 1/8-SCALE SHUTTLE MODEL AT LIFT-OFF

Mode	Input code (a)	Frequency, Hz		Mode description	Figure
1	G	14.03	AS	Gear-train rotation	23(a)
2	B	16.60	AS	ET y-direction 1st bending	33(a)
3	Q	17.50	S	ET z-direction 1st bending	23(b)
4	G	17.86	S	Rack-and-pinion motion	23(c)
5	H	20.64	AS	Orb. roll, payload and wing not in phase	33(b)
6	G	22.25	AS	Orb. roll, payload and wing in phase	33(c)
7	M	24.37	AS	ET 1st torsion, Orb. wing and ET in phase	23(d)
8	A	25.32	S	1st longitudinal	23(e)
9	A	28.13	S	Orb. longitudinal	33(d)
10	G	32.27	S	Orb. pitch, SRB roll and ET z-direction translation are in phase	33(e)
11	K	35.25	S	Orb. pitch, SRB roll and ET z-direction translation are not in phase	33(f)
12	F	38.22	S	SRB y-direction yaw and bending	23(f)
13	L	43.29	AS	SRB z-direction 1st bending	33(g)
14	N	45.15	S	Orb. z-direction 1st bending	33(h)
15	A	48.50	S	ET z-direction 2nd bending	33(i)
16	S	51.39	AS	Orb. 1st wing bending	33(j)
17	R	51.66	S	Orb. 1st wing bending	33(k)
18	F	57.64	AS	Orb. y-direction 1st bending, SRB y-direction 1st bending	33(l)
19	B	58.65	AS	Fin y-direction, Orb. y-direction bending	33(m)
20	L	64.14	AS	ET 2nd torsion	33(n)
21	K	71.23	S	ET z-direction 3rd bending, and SRB 1st bending	23(g)
22	L	75.02	AS	ET torsion and SRB z-direction 1st bending	33(o)
23	F	76.39	S	SRB y-direction 1st bending	23(h)
24	Q	81.23	S	Orb. z-direction	33(p)
25	Q	86.58	AS	Orb. 1st torsion	33(q)
26	Q	96.99	S	Orb. payload pitch	33(r)
27	L	117.50	AS	ET torsion and SRB z-direction 2nd bending	33(s)
28	K	124.60	S	SRB 1st torsion and z-direction bending	23(i)
29	F	129.48	S	SRB y-direction 2nd bending and torsion	23(j)

[a]See table IV for input-code definitions.

TABLE VII.- SUMMARY OF MEASURED VIBRATION MODES OF THE 1/8-SCALE SHUTTLE MODEL AT MID-BOOST (q_{max})

Mode	Input code (a)	Frequency, Hz	Mode description		Figure
1	J	14.72	AS	Gear-train rotation	34(a)
2	F	15.84	S	SRB y-direction translation and bending	24(a)
3	C	18.68	S	Rack-and-pinion motion	34(b)
4	F	19.39	AS	ET y-direction 1st bending	24(b)
5	T	19.90	S	ET z-direction 1st bending	24(c)
6	J	23.08	AS	Orb. roll, payload and wing not in phase	34(c)
7	F	24.16	AS	Orb. roll, payload and wing in phase	34(d)
8	C	27.82	S	1st longitudinal	24(d)
9	J	28.50	AS	ET 1st torsion, Orb. wing and ET in phase	24(e)
10	C	29.93	S	Orb. longitudinal	34(e)
11	T	33.80	S	Orb. pitch, ET z-bending, and SRB roll	34(f)
12	J	35.52	AS	Orb. y-direction yaw, SRB's pitching out of phase, ET torsion	34(g)
13	T	41.98	S	Orb. z-direction 1st bending, ET z-direction 2nd bending	34(h)
14	F	45.49	S	SRB y-direction yawing and bending	34(i)
15	F	51.49	AS	Orb. 1st wing bending	34(j)
16	C	52.65	S	Orb. 1st wing bending	34(k)
17	J	53.84	AS	SRB z-direction 1st bending, fin y-direction	34(l)
18	J	59.12	AS	Fin y-direction, Orb. y-direction 1st bending	34(m)
19	I	74.71	AS	ET torsion, SRB y- and z-direction bending	34(n)
20	A	78.68	S	ET z-direction 3rd bending, SRB 1st bending, payload 1st bending	34(o)
21	T	83.30	S	Orb. z-direction and ET z-direction 3rd bending	34(p)
22	U	87.40	AS	Orb. 1st torsion	34(q)
23	A	89.08	S	SRB y-direction 1st bending	24(f)
24	Q	96.12	S	Orb. payload pitch	34(r)
	A	140.88	S	SRB 1st torsion and z-direction bending	34(s)

[a]See table IV for input-code definitions.

TABLE VIII.- SUMMARY OF MEASURED VIBRATION MODES OF THE 1/8-SCALE SHUTTLE MODEL AT END-BOOST (BEFORE SRB SEPARATION)

Mode	Input code (a)	Frequency, Hz	Mode description		Figure
1	F	18.39	AS	Gear-train rotation	35(a)
2	Q	20.40	S	ET z-direction 1st bending	25(a)
3	K	26.23	S	Rack-and-pinion motion	35(b)
4	F	26.27	AS	ET y-direction 1st bending	35(c)
5	F	27.46	S	SRB y-direction translation and bending	25(b)
6	C	27.68	S	1st longitudinal (high coupling with mode 5)	25(c)
7	F	30.13	AS	Orb. roll	35(d)
8	C	32.34	S	Orb. longitudinal and pitching	25(d)
9	A	32.42	S	Orb. pitch, ET z-bending, and SRB roll	35(e)
10	F	32.50	AS	Orb. roll, payload and wing in phase	35(f)
11	K	44.50	S	Orb. z-direction 1st bending	35(g)
12	L	45.33	AS	ET 1st torsion	35(h)
13	I	50.24	AS	Orb. wing 1st bending	35(i)
14	K	52.69	S	Orb. wing 1st bending	35(j)
15	I	61.58	AS	Fin y-direction, Orb. y-direction 1st bending	35(k)
16	F	74.87	S	SRB y-direction yawing and bending	35(l)
17	K	81.06	S	Orb. z-direction	35(m)
18	L	88.17	AS	SRB z-direction 1st bending	35(n)
19	U	89.30	AS	Orb. 1st torsion	35(o)
20	L	94.88	S	Orb. payload pitching	35(p)
	F	103.85	AS	SRB y-direction 1st bending	35(q)
	F	130.05	S	SRB y-direction 1st bending	35(r)

[a]See table IV for input-code definitions.

TABLE IX.- SUMMARY OF MEASURED VIBRATION MODES OF THE 1/8-SCALE SHUTTLE MODEL AT END-BOOST (AFTER SRB SEPARATION)

Mode	Input code (a)	Frequency, Hz	Mode description		Figure
1	Q	21.76	S	ET z-direction 1st bending, Orb. pitching, ET bulging	26(a)
2	E	28.59	AS	ET y-direction 1st bending, Orb. yawing, fin lateral	36(a)
3	D	33.00	S	1st longitudinal	26(b)
4	P	33.40	AS	ET and Orb. gear-train rotation	36(b)
5	I	41.14	AS	Orb. payload and fin lateral motion not in phase	36(c)
6	Q	45.28	S	Orb. z-direction 1st bending	26(c)
7	R	50.08	S	Orb. wing 1st bending	26(d)
8	P	51.75	AS	Orb. fin lateral motion, out-of-phase wing bending	36(d)
9	Q	53.97	S	Orb. fin pitching, payload translation, fuselage 2nd bending	36(e)
10	I	60.87	AS	Orb. and ET y-direction 1st bending, fin lateral motion	36(f)
11	P	61.30	AS	Orb. and ET gear-train rotation, out-of-phase y-direction bending	36(g)
12	E	67.40	AS	Orb. wing yawing, fuselage y-direction bending	36(h)
13	S	78.37	AS	ET and Orb. gear-train rotation and Orb. fuselage y- and z-direction bending. Wing yawing in phase with fuselage and wing bending not in phase with fuselage rotation	36(i)
14	I	80.10	AS	ET 1st torsion, Orb. motion similar to mode 13	26(e)
15	I	89.88	AS	Orb. 1st torsion, ET rotation with torsion	26(f)
16	J	94.90	AS		36(j)
17	J	107.60	AS	Orb. payload y-direction yawing and bending, fuselage torsion	36(k)

[a]See table IV for input-code definitions.

TABLE X.- SUMMARY OF VIBRATION MODES OF THE 1/8-SCALE SHUTTLE MODEL AT END-BURN (BEFORE ET JETTISON)

Mode	Input code (a)	Frequency, Hz	Mode description		Figure
1	T	32.13	S	Orb. and ET pitching not in phase, ET bulging	27(a)
2	J	35.65	AS	Orb. and ET gear-train rotation and out-of-phase yawing, fin lateral motion in phase with wing	27(b)
3	J	39.00	AS	Orb. and ET same as mode 2, fin lateral motion not in phase	37(a)
4	T	42.91	S	Orb. z-direction 1st bending	27(c)
5	J	44.76	AS	Orb. and ET yawing and bending out of phase, payload lateral motion	37(b)
6	Q	51.33	S	Orb. wing 1st bending	27(d)
7	I,J,S	51.81	AS	Orb. fin lateral motion	37(c)
8	D	54.86	S	1st longitudinal, payload and ET not in phase	37(d)
9	D	59.74	S	Longitudinal, Orb. and ET not in phase	37(e)
10	J	61.21	AS	Orb. y-direction 1st bending	37(f)
11	D	63.16	S	ET longitudinal and z-direction 1st bending	27(e)
12	P	73.82	AS	Orb. wing yaw and roll, fuselage y-direction bending	27(f)
13	S	77.45	AS	Orb. and ET gear-train rotation and wing bending not in phase with Orb. fuselage	37(g)
14	D	80.10	S	Orb. fin pitching not in phase with fuselage bending	37(h)
15	P	93.61	AS	ET y-direction 1st bending and payload yawing out of phase	37(i)

[a]See table IV for input-code definitions.

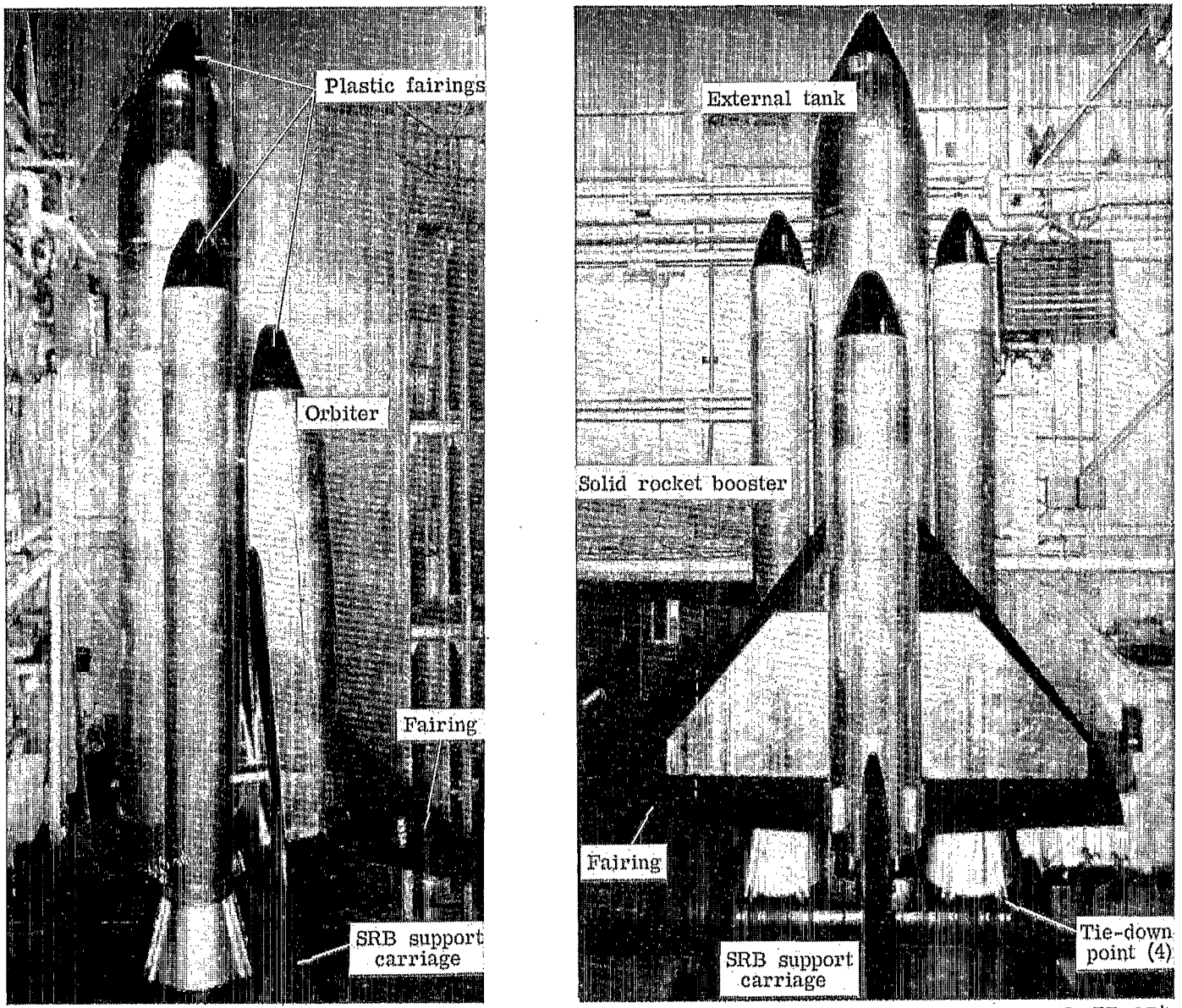

Figure 1.- 1/8-scale dynamic model of a space shuttle configuation.

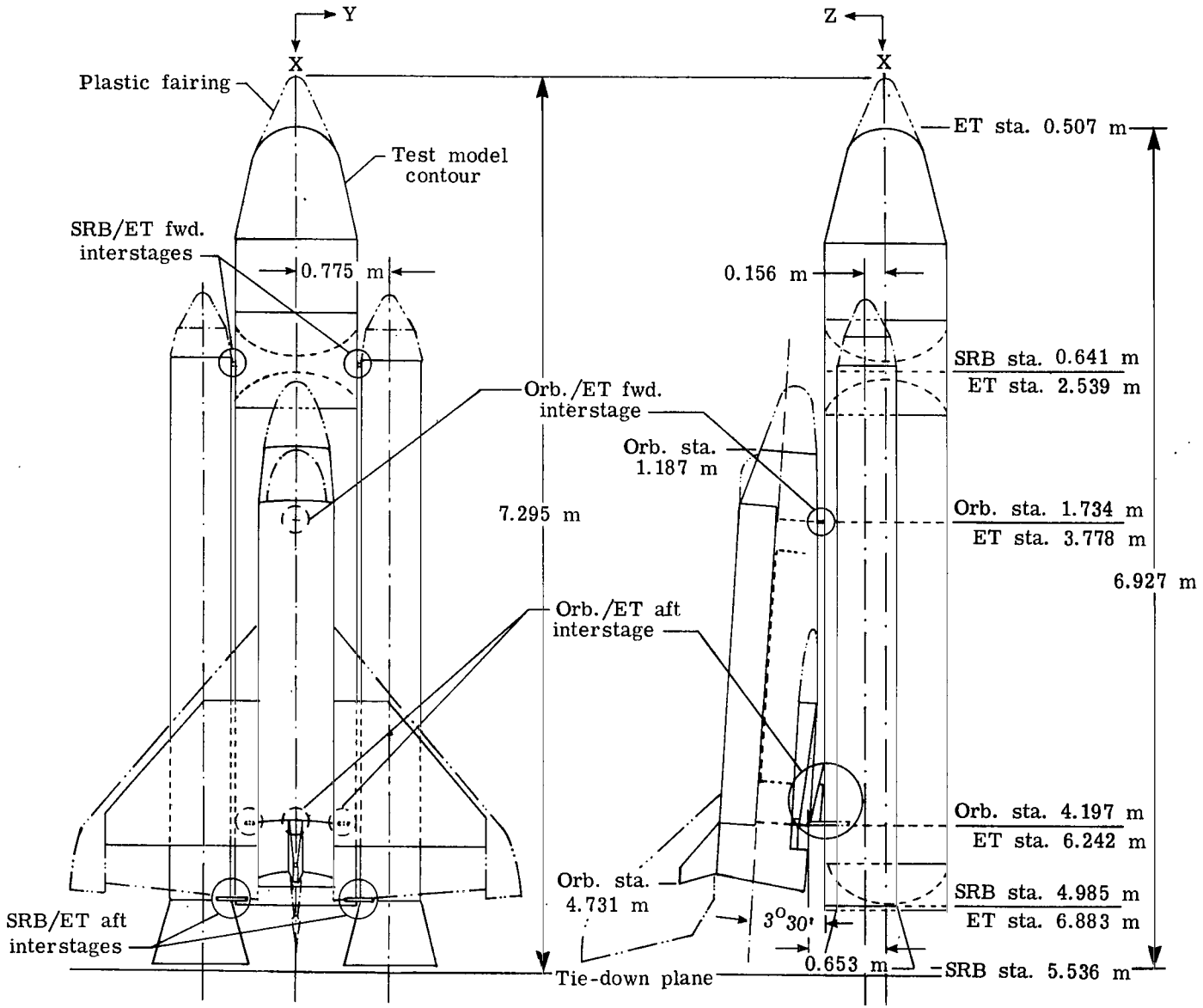

Figure 2.- General arrangement of 1/8-scale shuttle model.

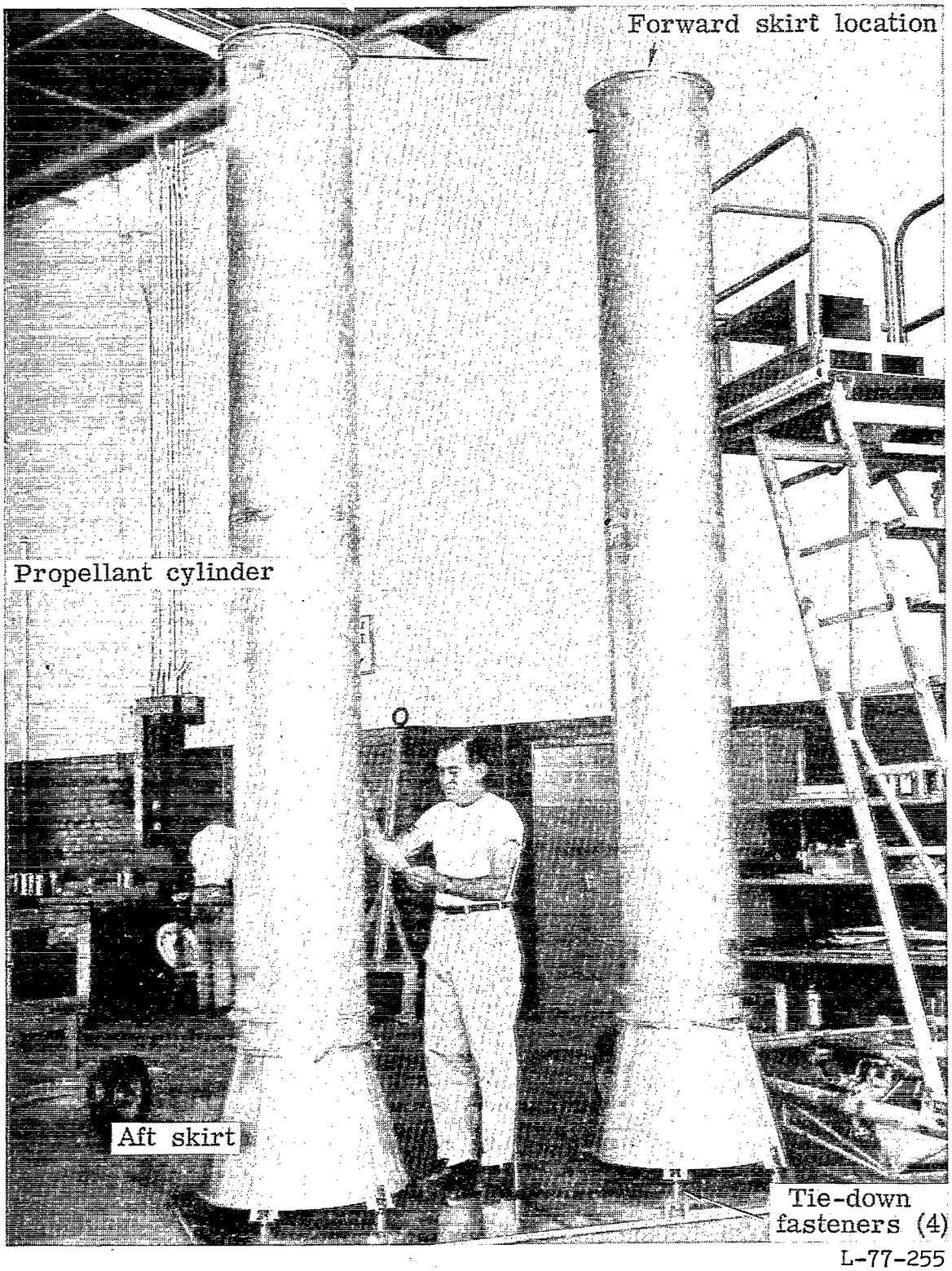

L-77-255

Figure 3.- Partially erected 1/8-scale SRB elements.

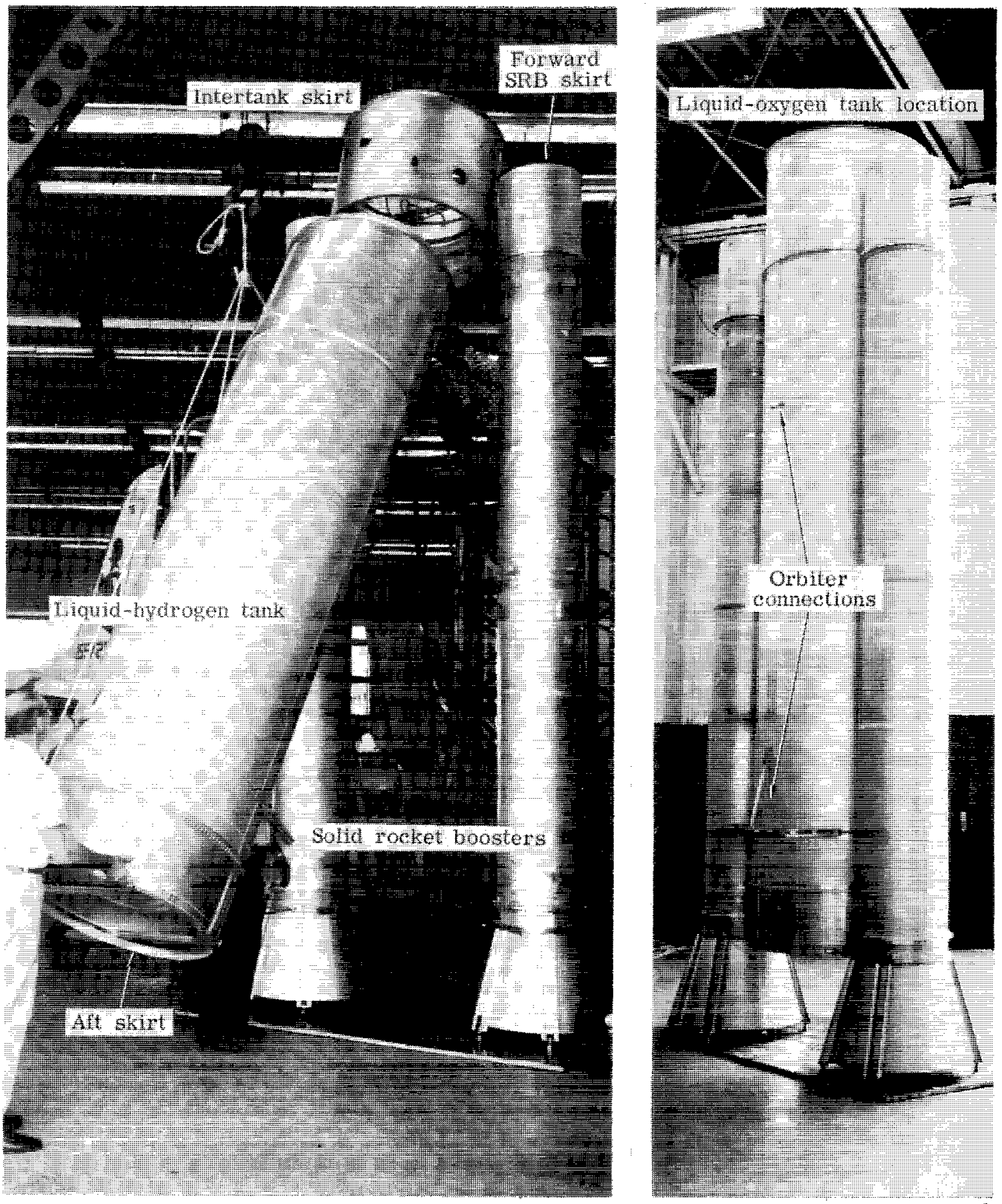

L-77-256

Figure 4.- 1/8-scale ET assembly with SRB elements.

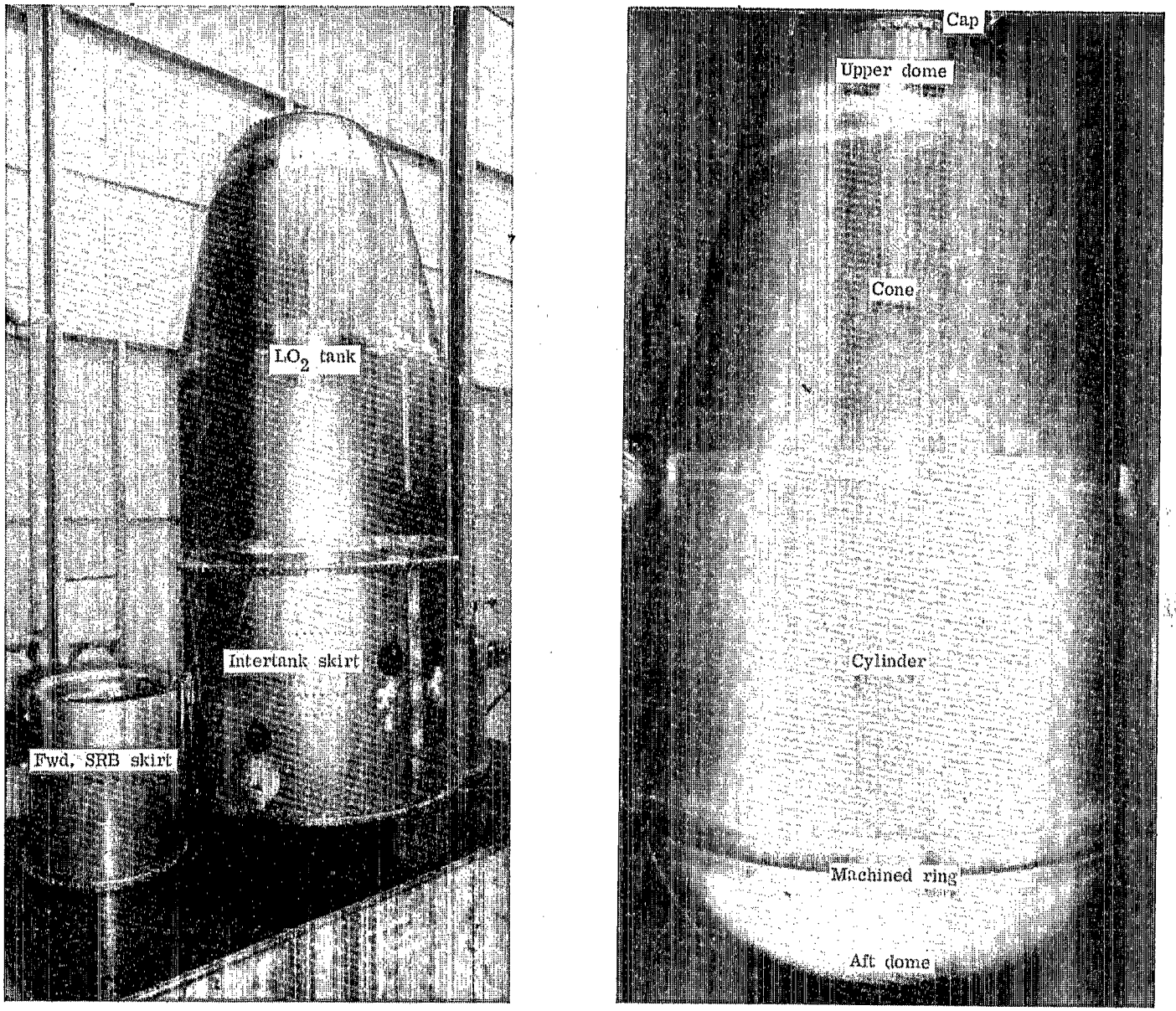

L-77-257

Figure 5.- 1/8-scale liquid-oxygen tank and assembly with intertank skirt of ET.

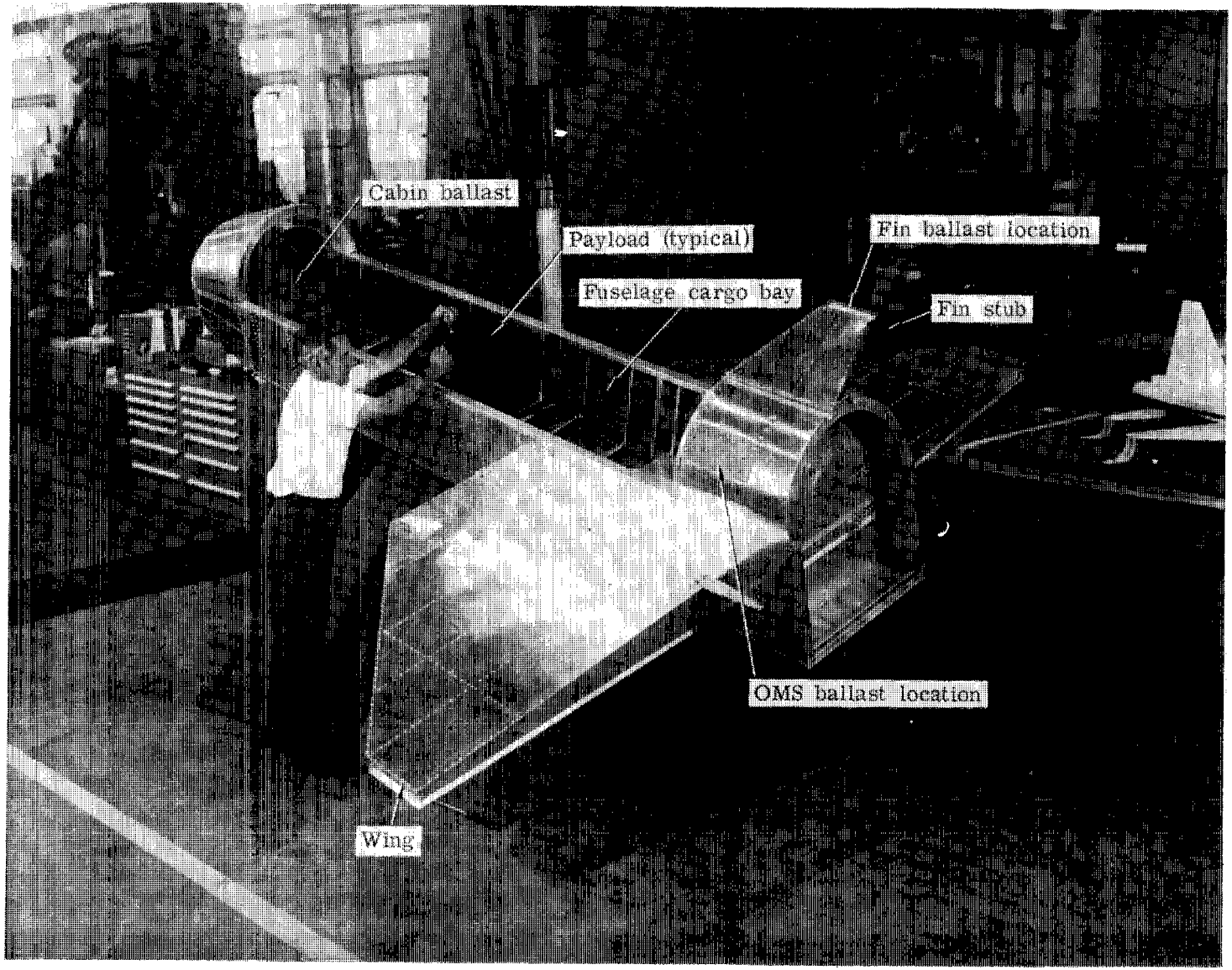

L-73-4241.1

Figure 6.- 1/8-scale orbiter element with cargo-bay door removed.

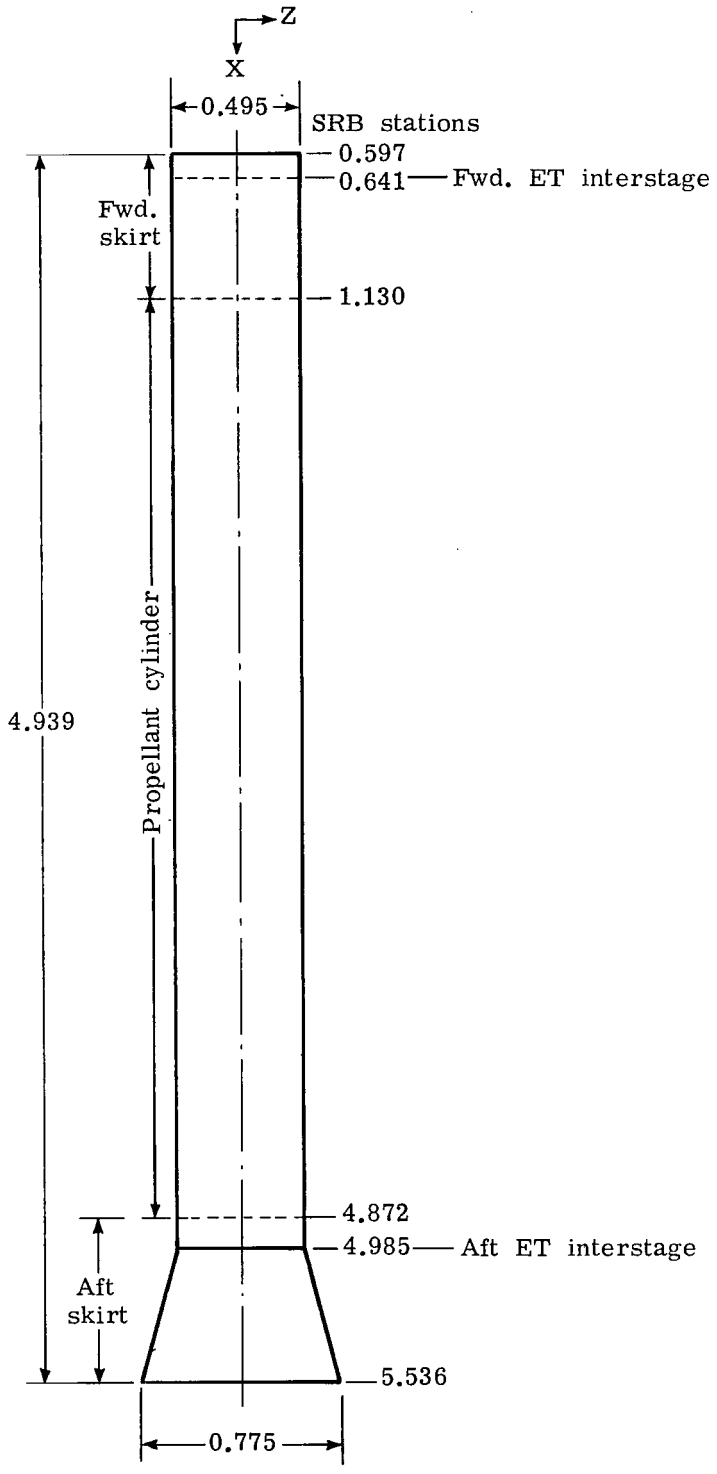

Figure 7.- Schematic drawing of assembled 1/8-scale SRB element. All dimensions and stations are in meters.

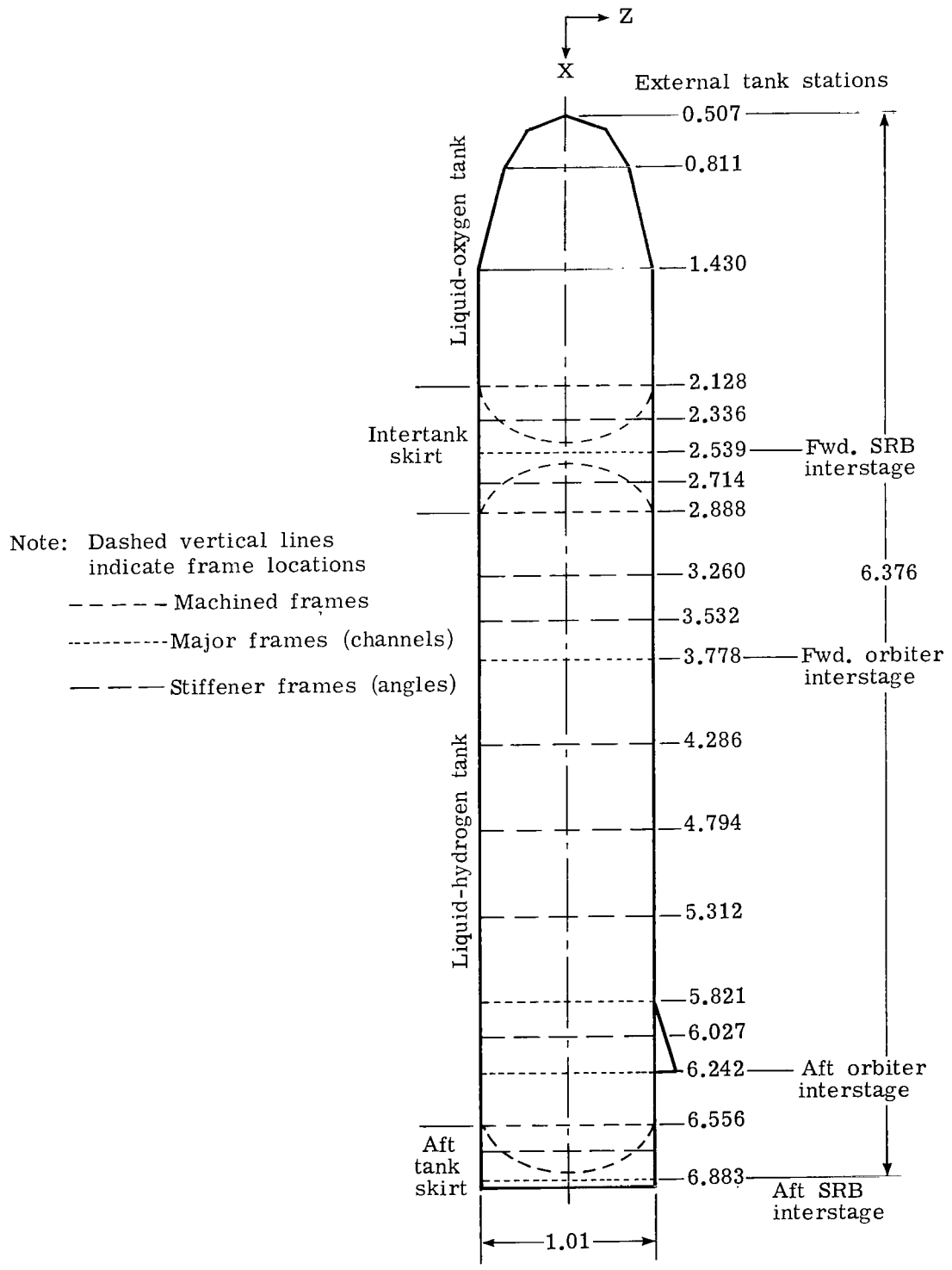

Figure 8.- Schematic drawing of 1/8-scale ET element. All dimensions and stations are in meters.

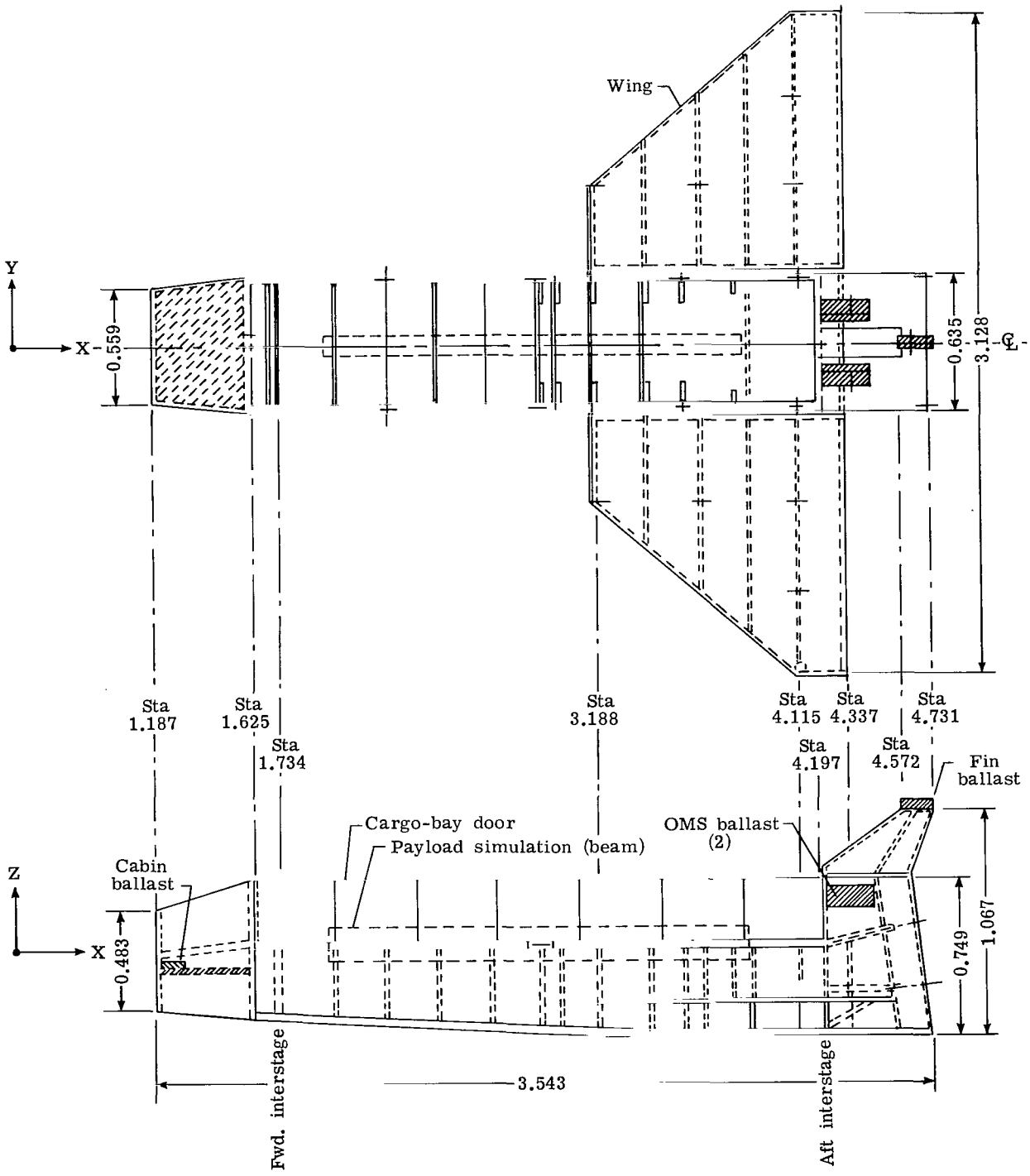

Figure 9.- Schematic drawing of 1/8-scale orbiter element. All stations and dimensions are in meters.

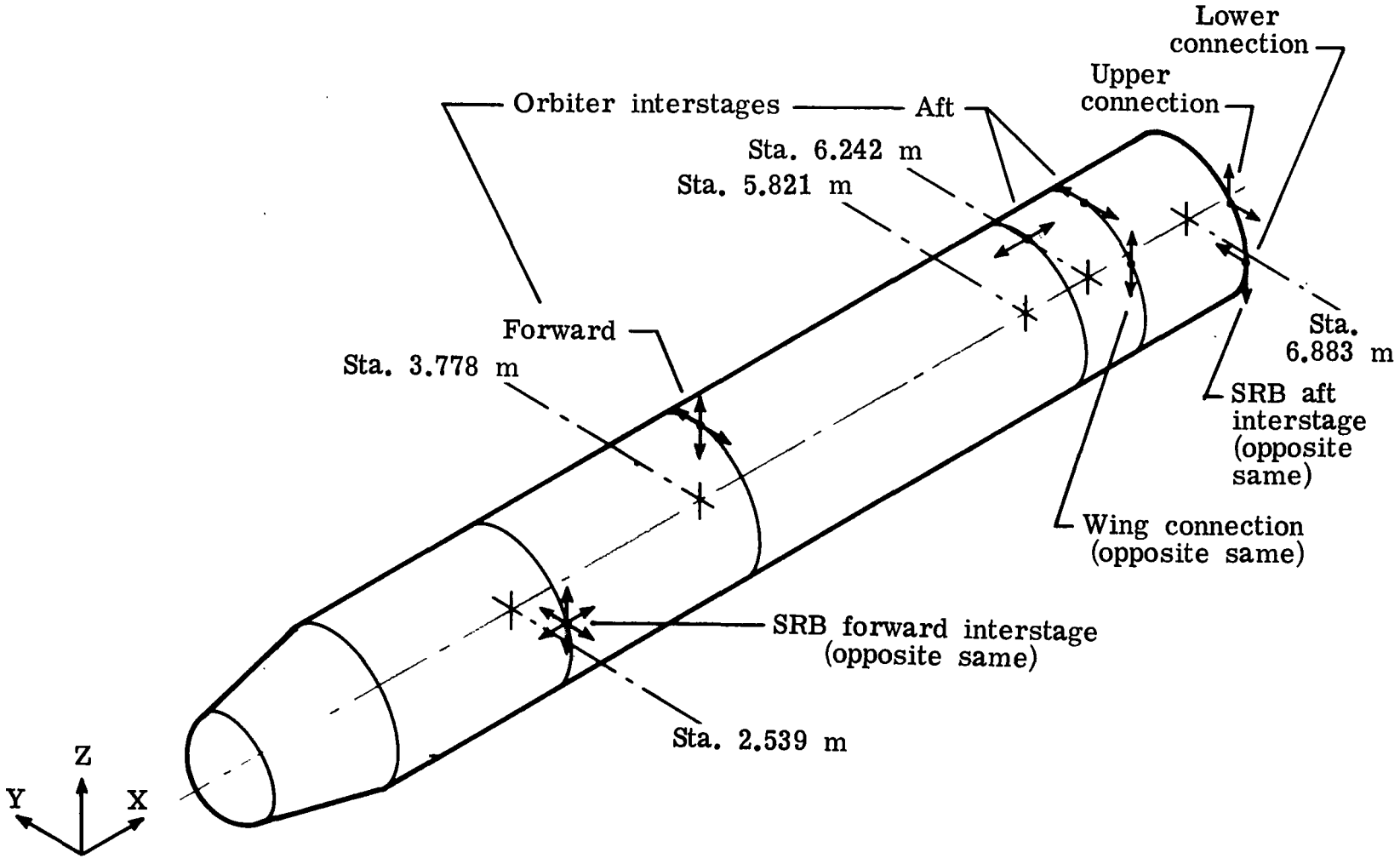

Figure 10.- Schematic diagram showing points of load application and direction at ET element for mated 1/8-scale shuttle model.

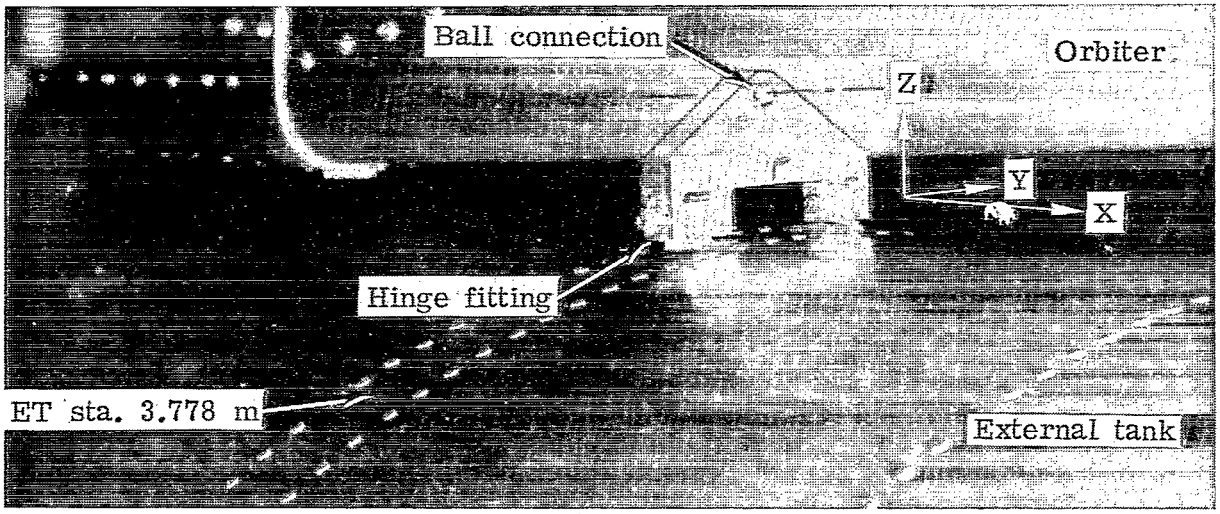

L-75-4779.1

(a) Forward interstage.

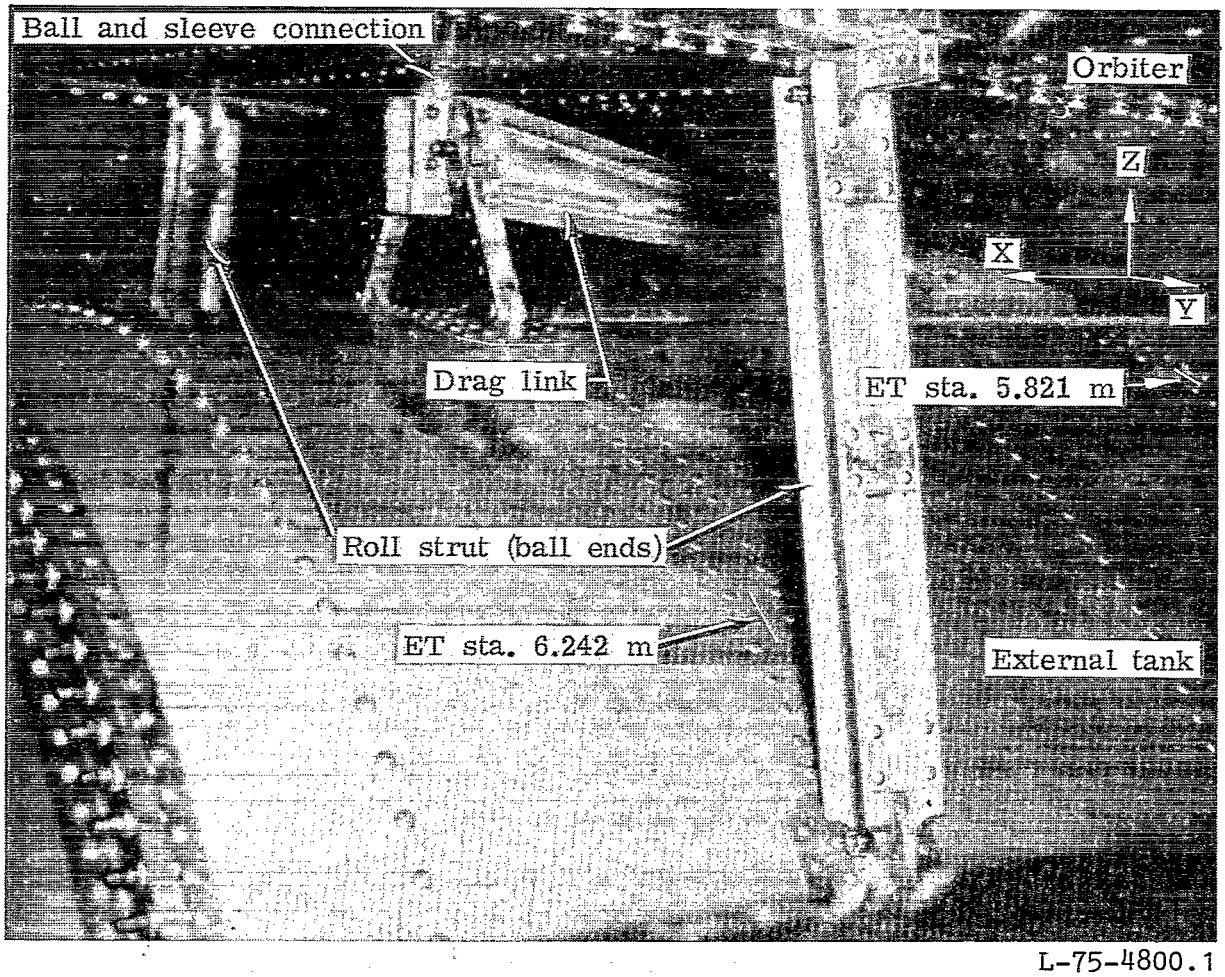

L-75-4800.1

(b) Aft interstage.

Figure 11.- Assembled Orb./ET interstage.

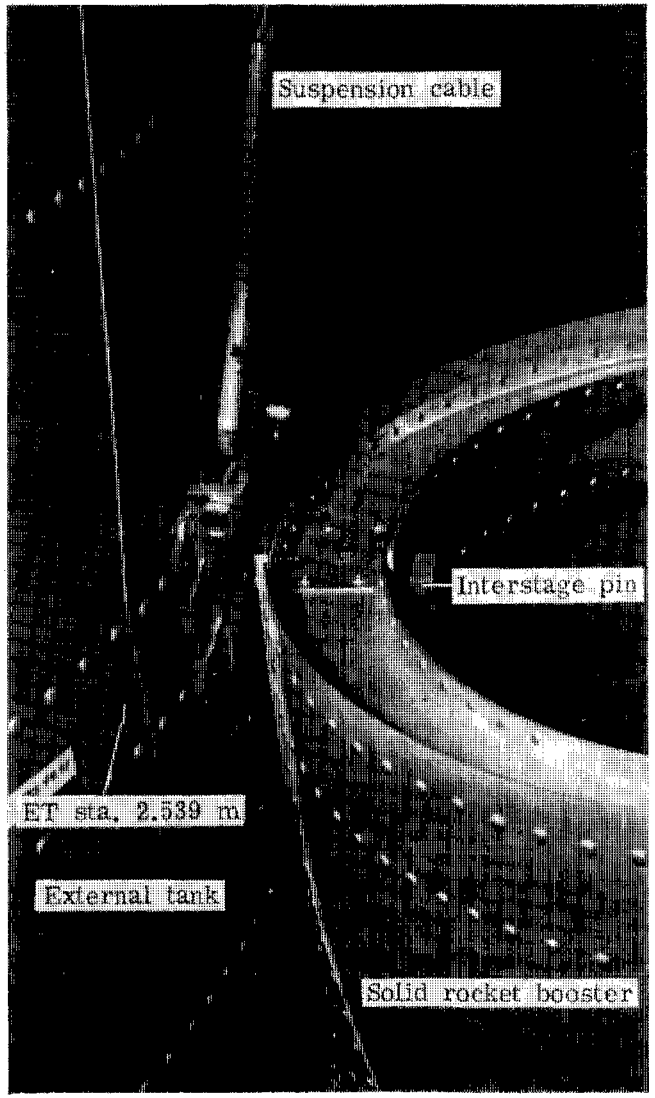

L-75-4778.1

(a) Forward interstage.

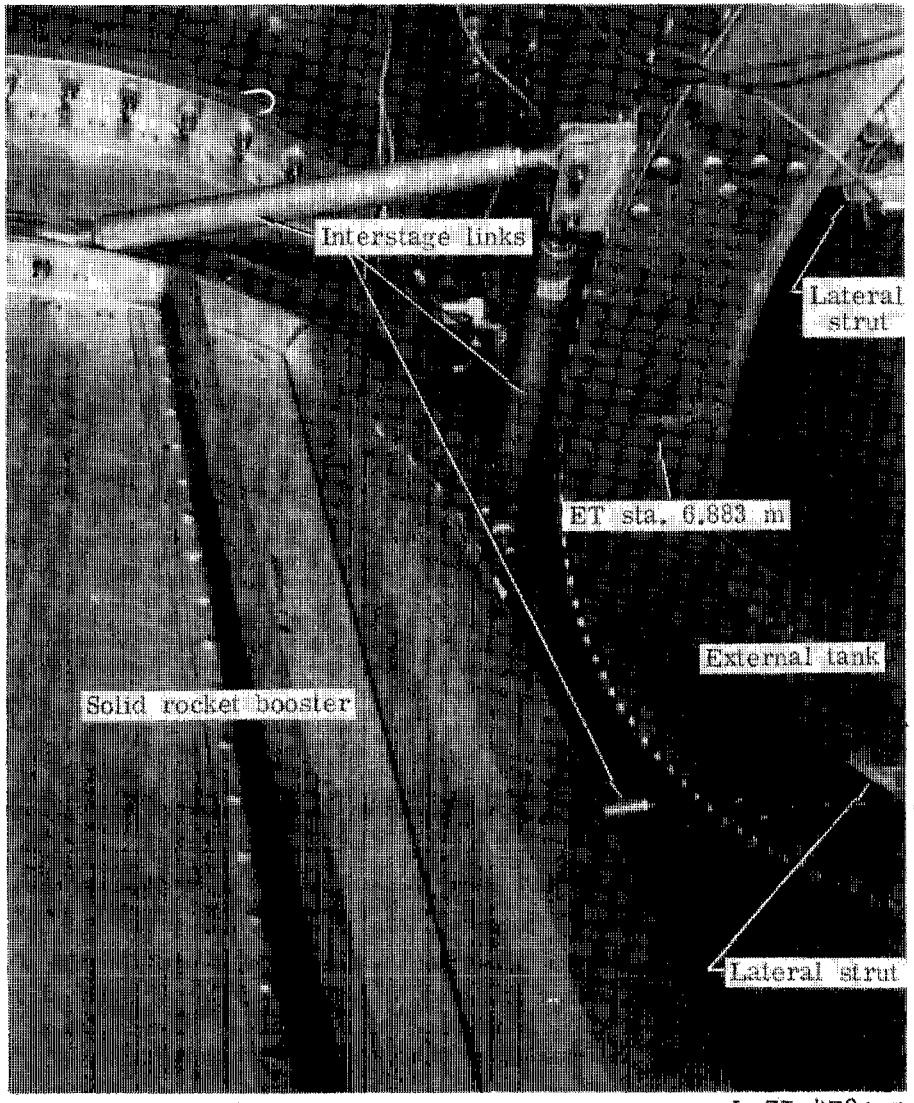

L-75-4781.1

(b) Aft interstage.

Figure 12.- Assembled 1/8-scale SRB/ET interstage.

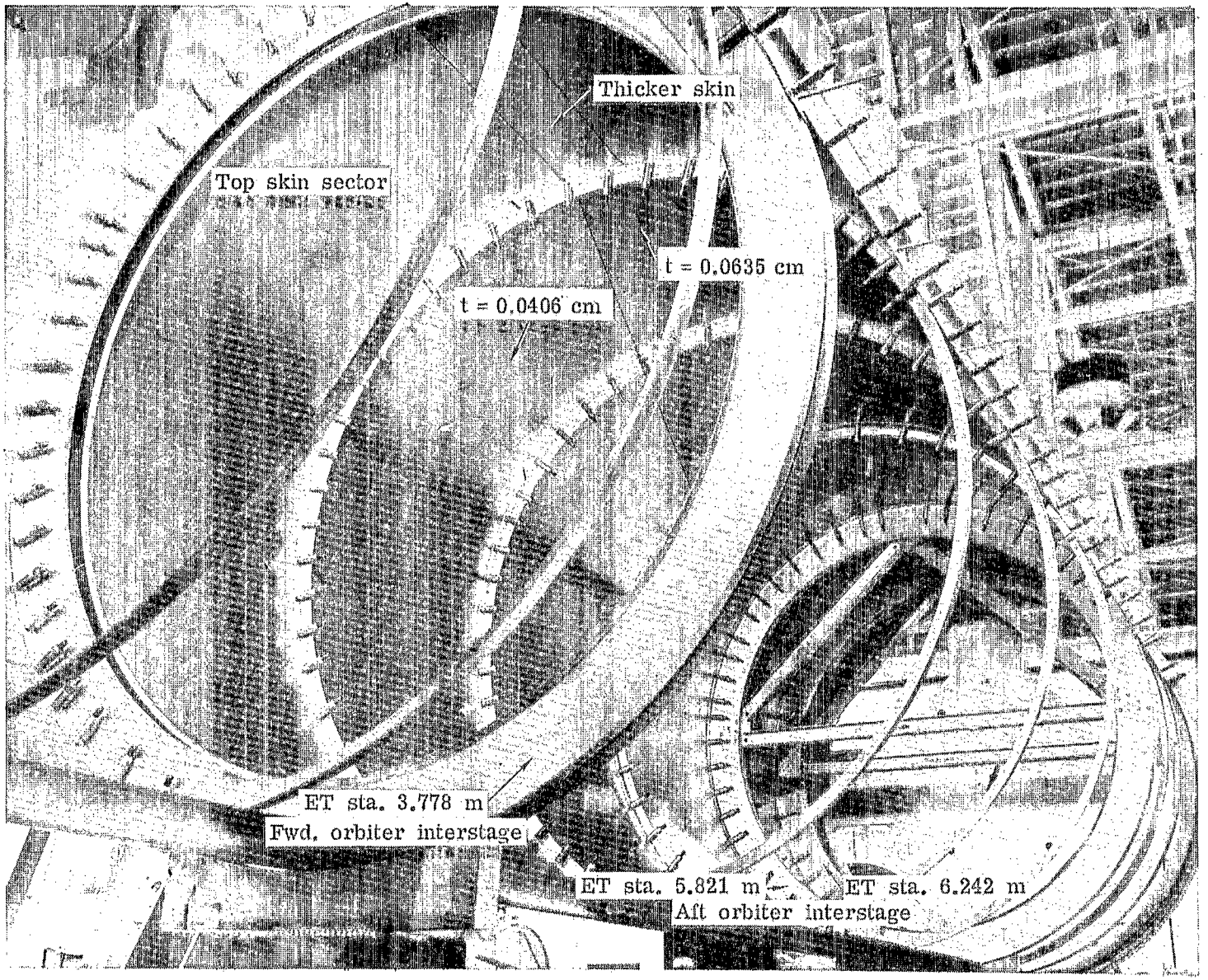

L-77-258

Figure 13.- Internal structure of partially fabricated liquid-hydrogen tank of ET.

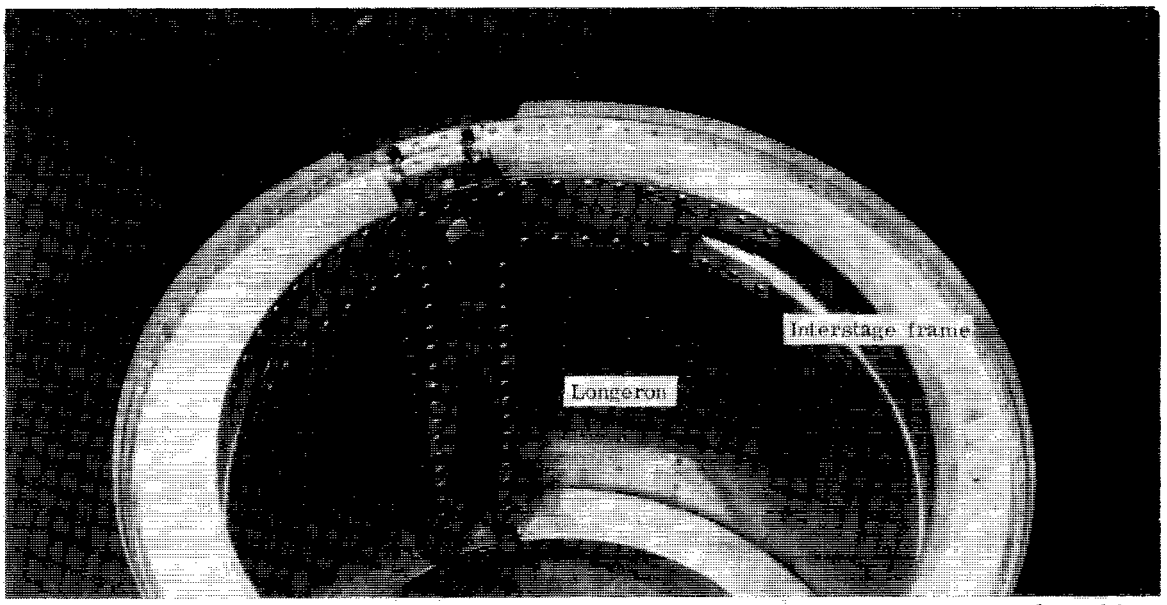

L-76-2766.1

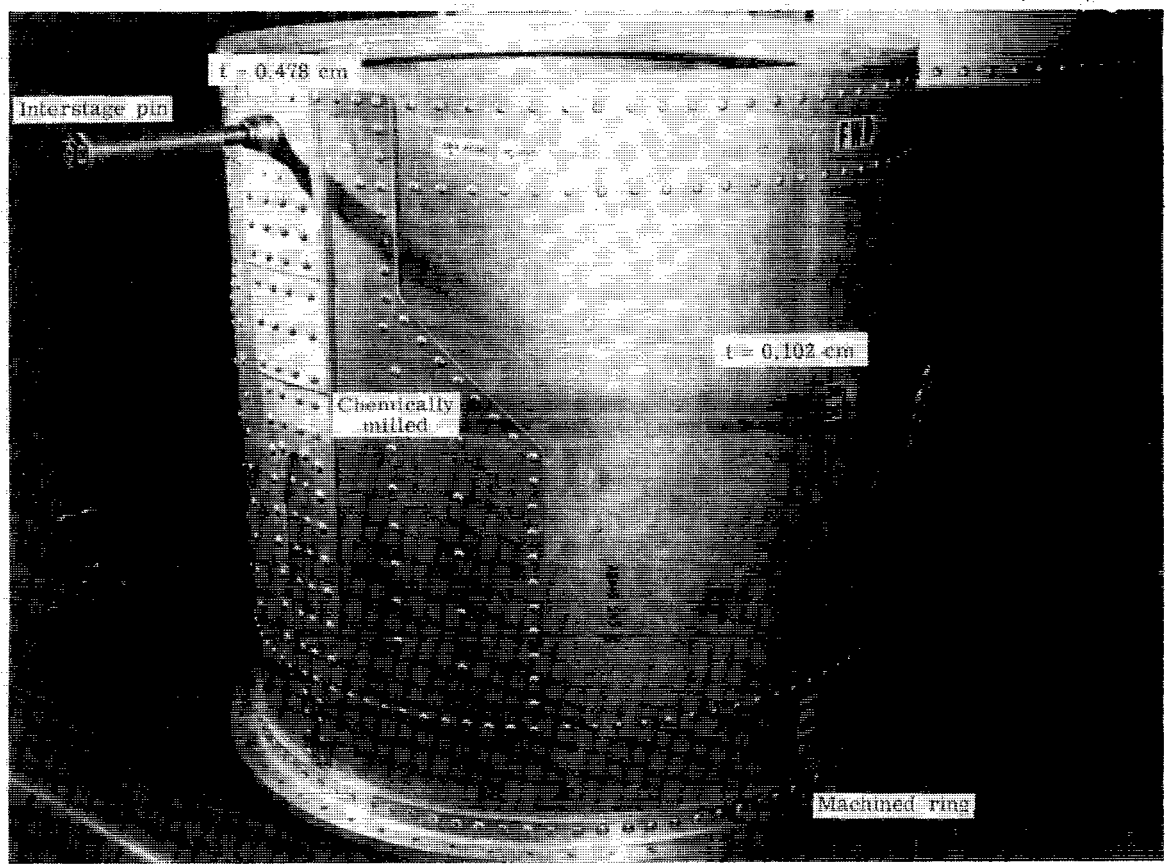

L-76-2763.1

Figure 14.- SRB interstage and foward skirt structure.

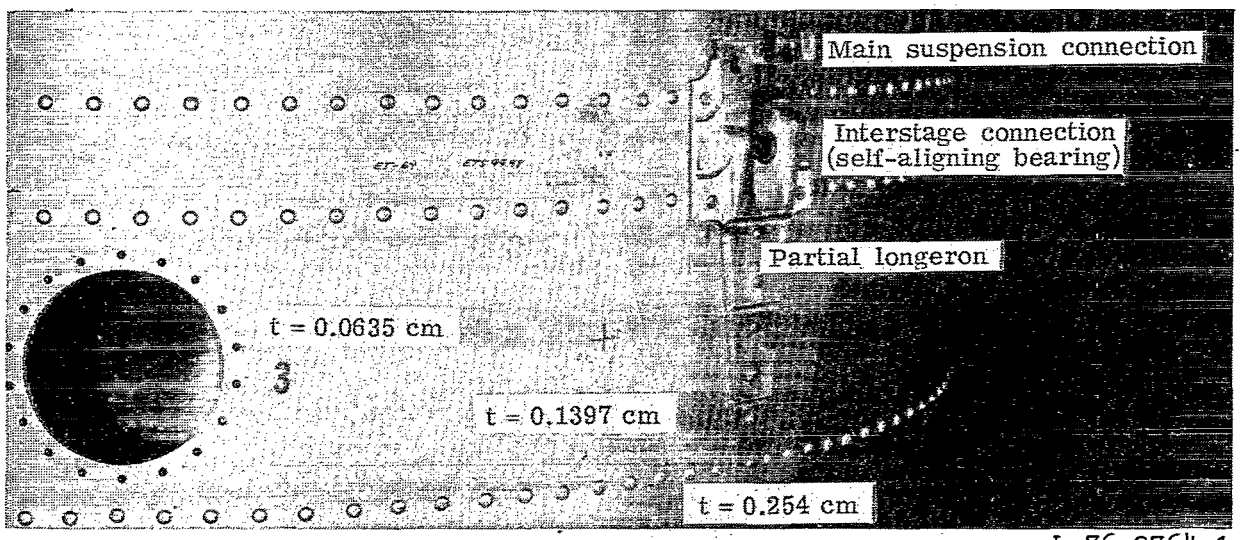

L-76-2764.1

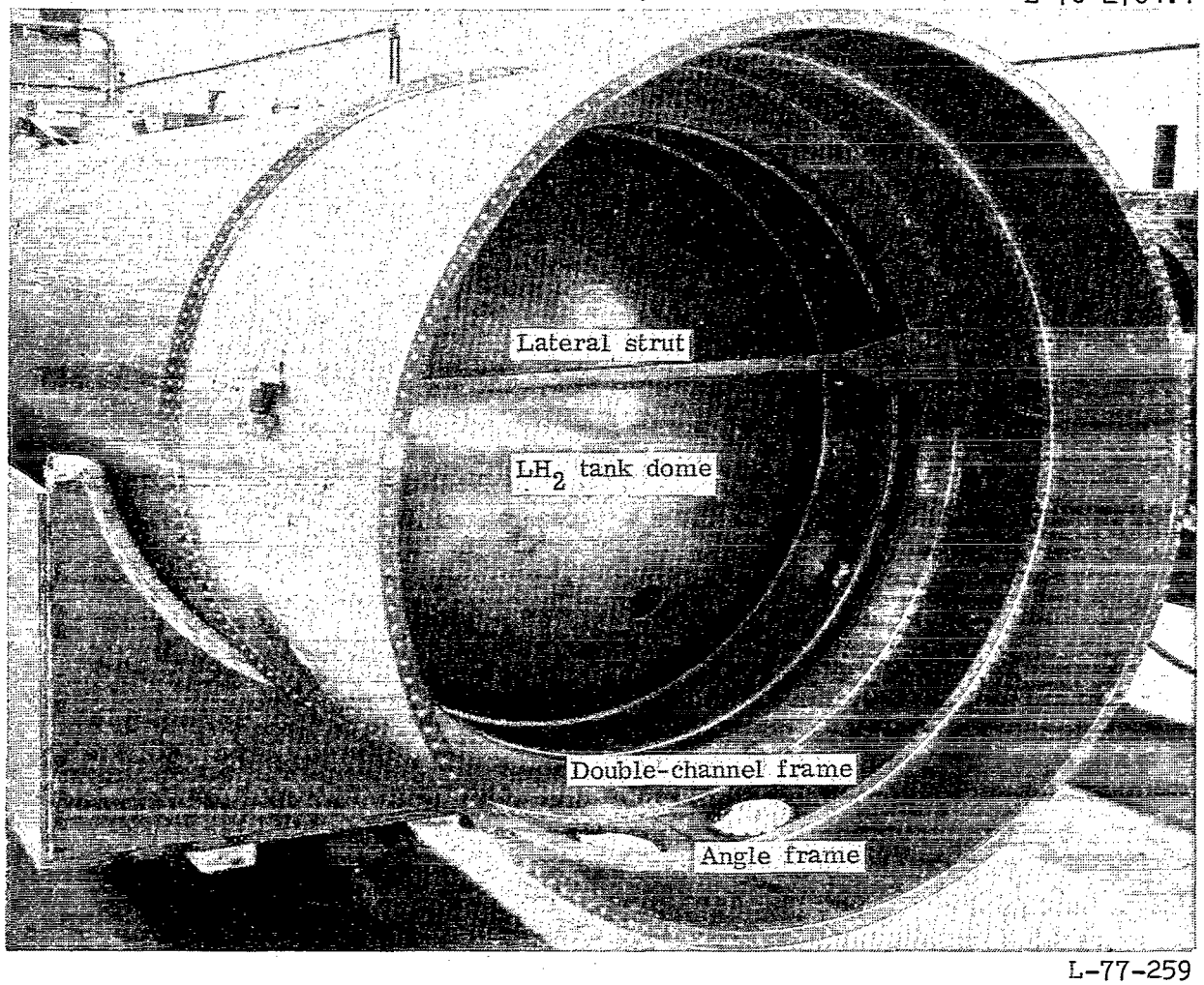

L-77-259

Figure 15.- SRB interstage and structure of ET intertank skirt.

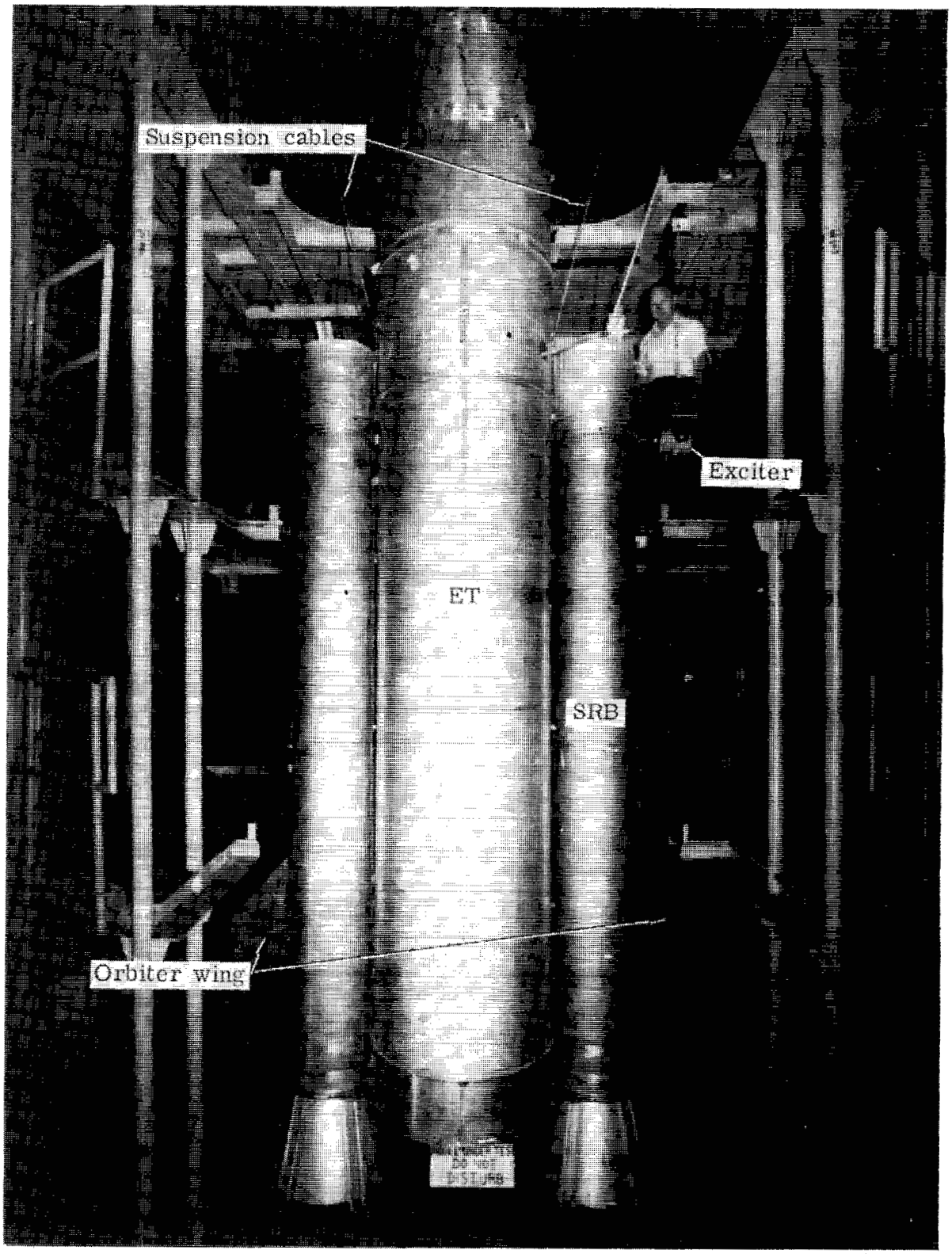

L-75-4777.1

Figure 16.- Mated 1/8-scale shuttle model installed in test facility.

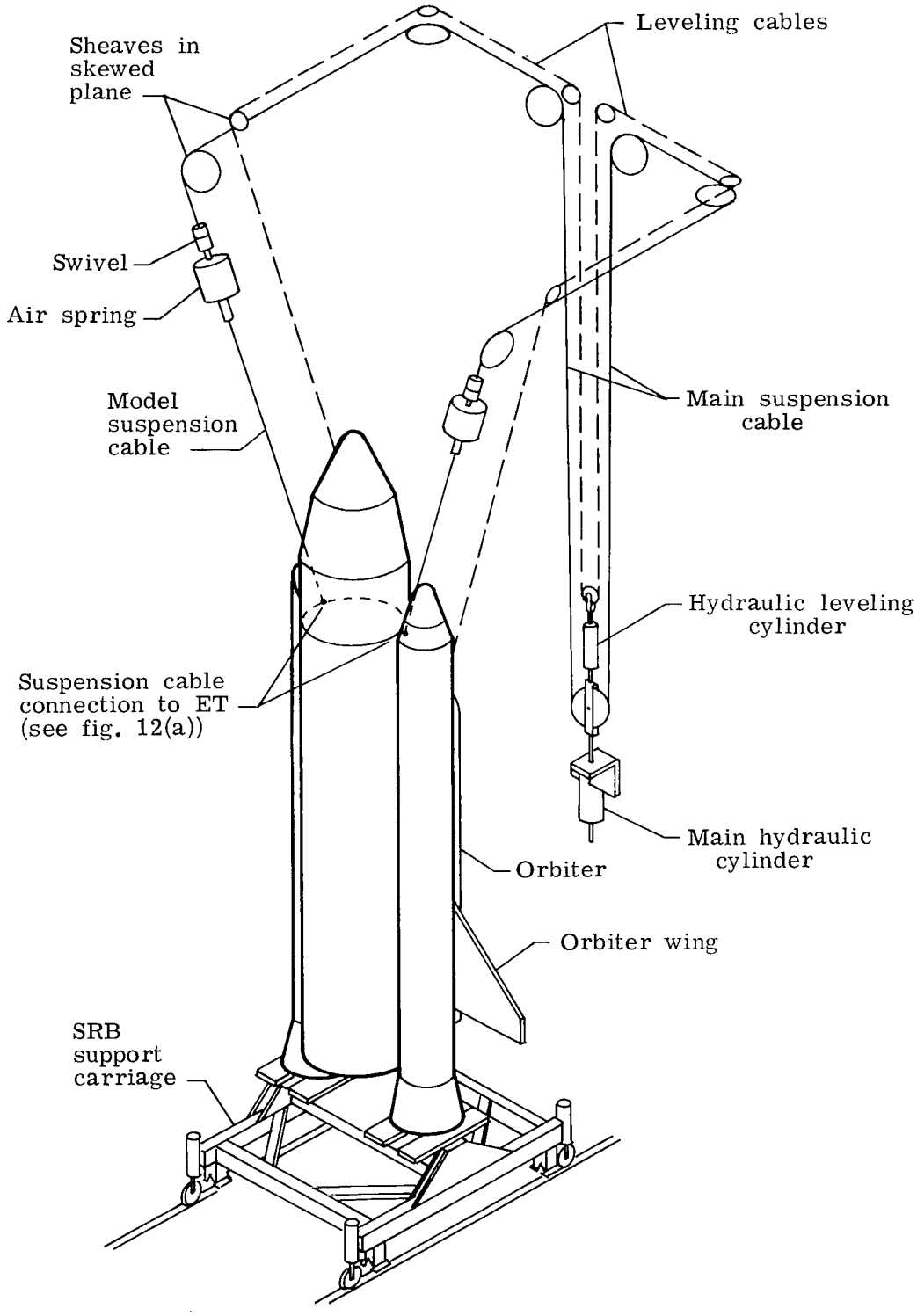

Figure 17.- Schematic drawing of suspension and handling system for vibration tests of 1/8-scale shuttle model.

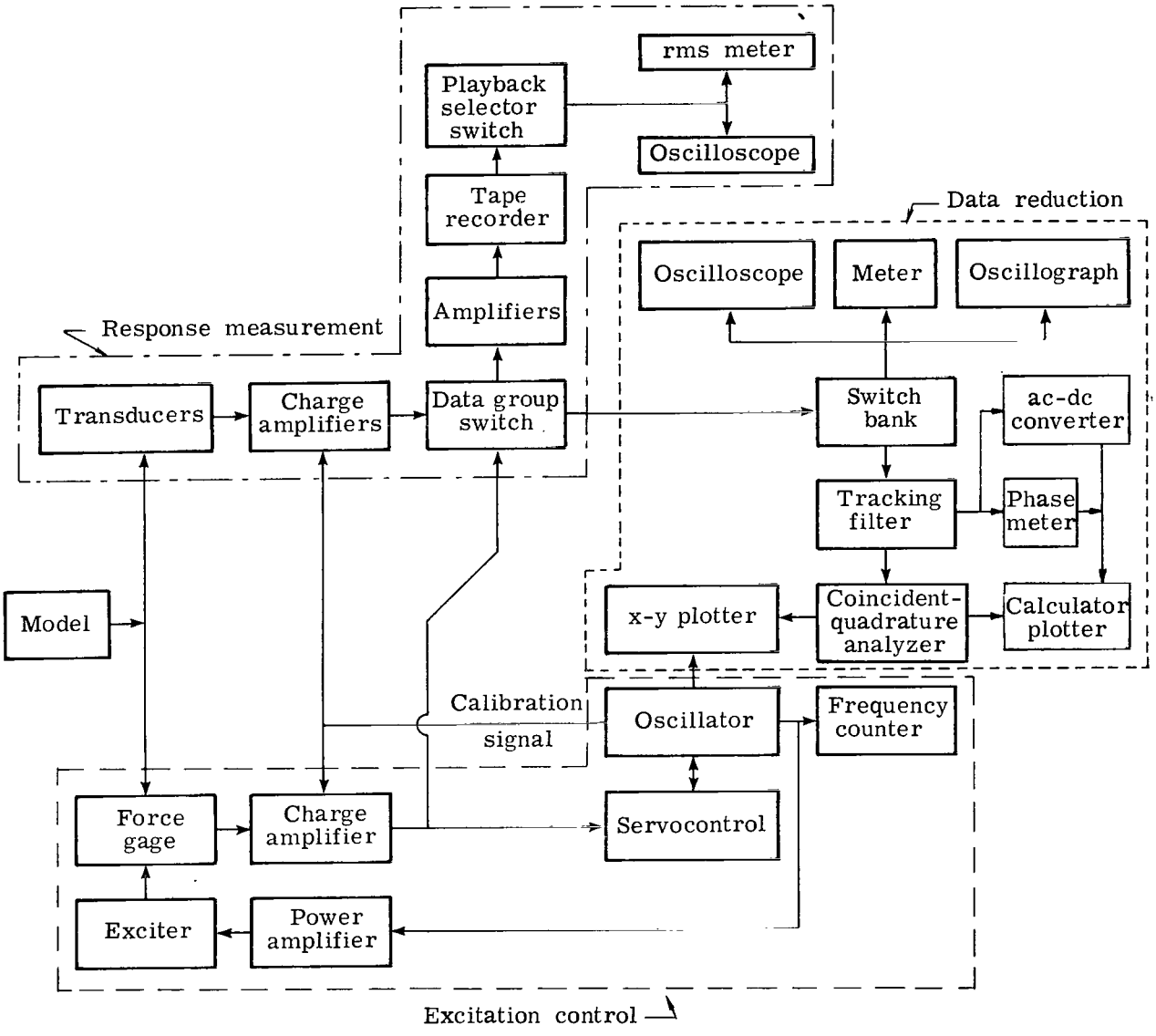

Figure 18.- Schematic diagram of data acquisition and reduction system.

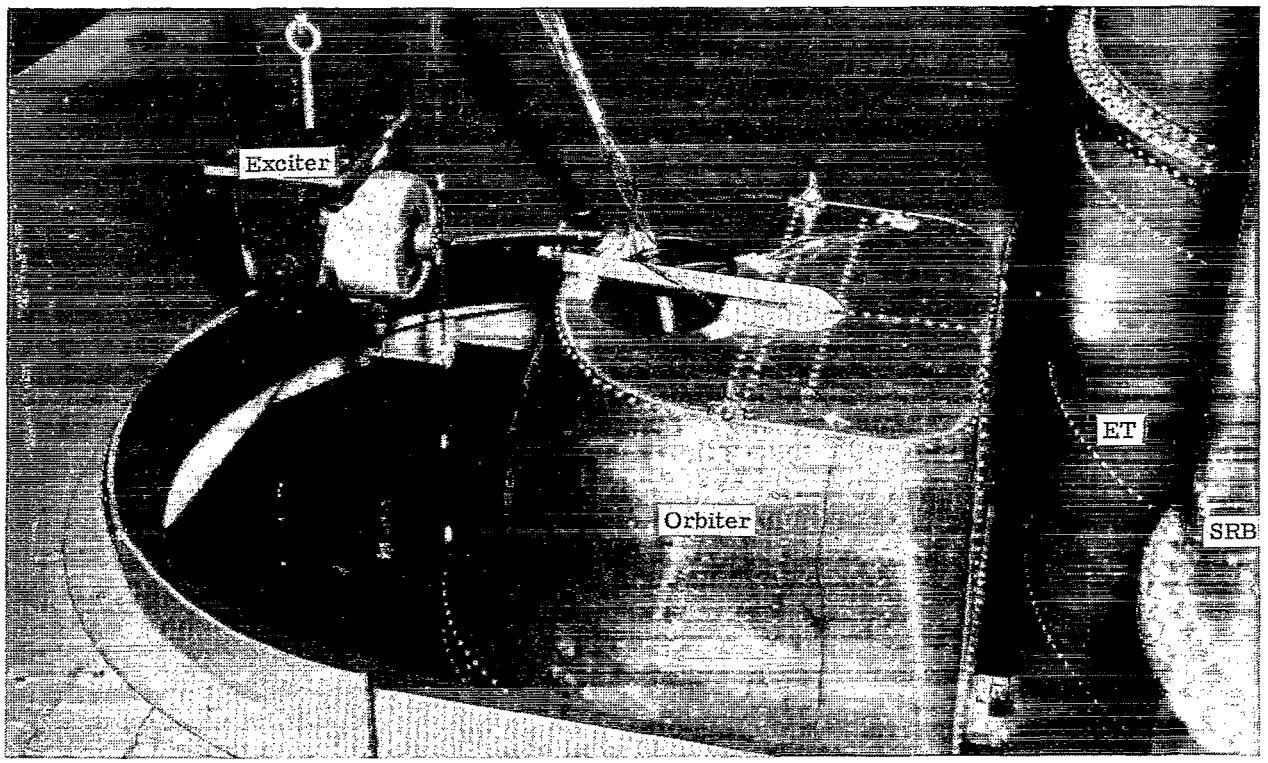

L-73-7741.2

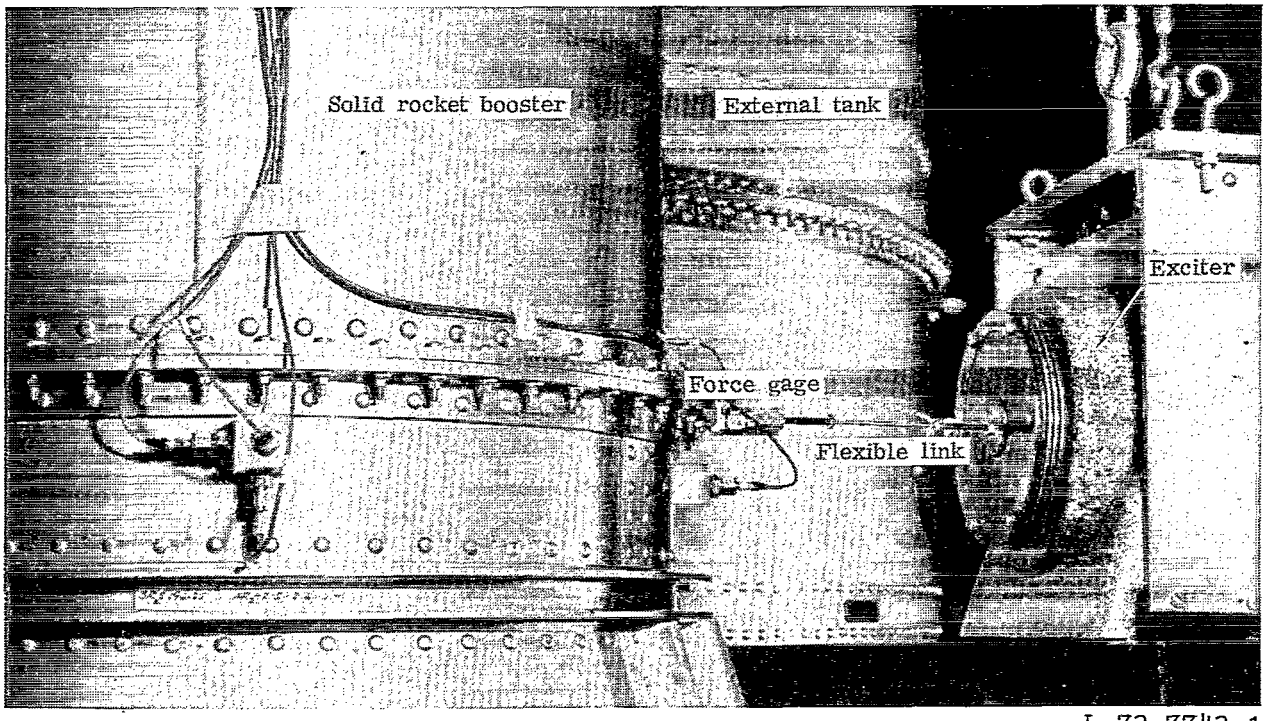

L-73-7743.1

Figure 19.- Typical exciter installations for vibration of 1/8-scale shuttle model.

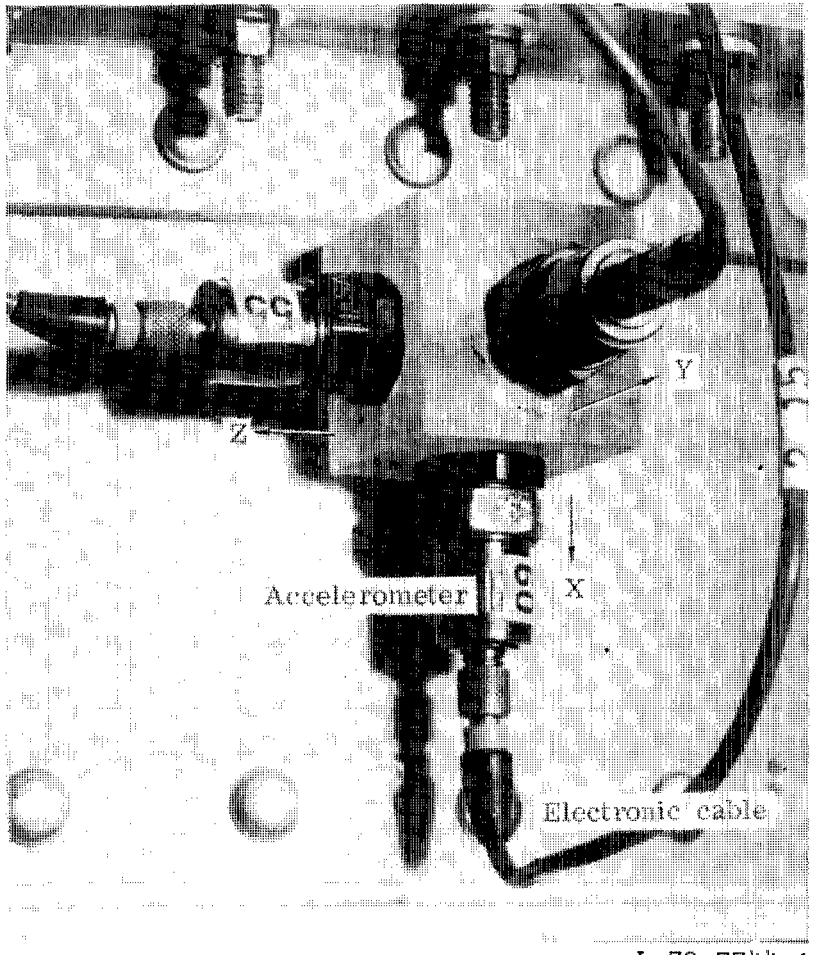

L-73-7744.1

(a) Typical triaxial arrangement.

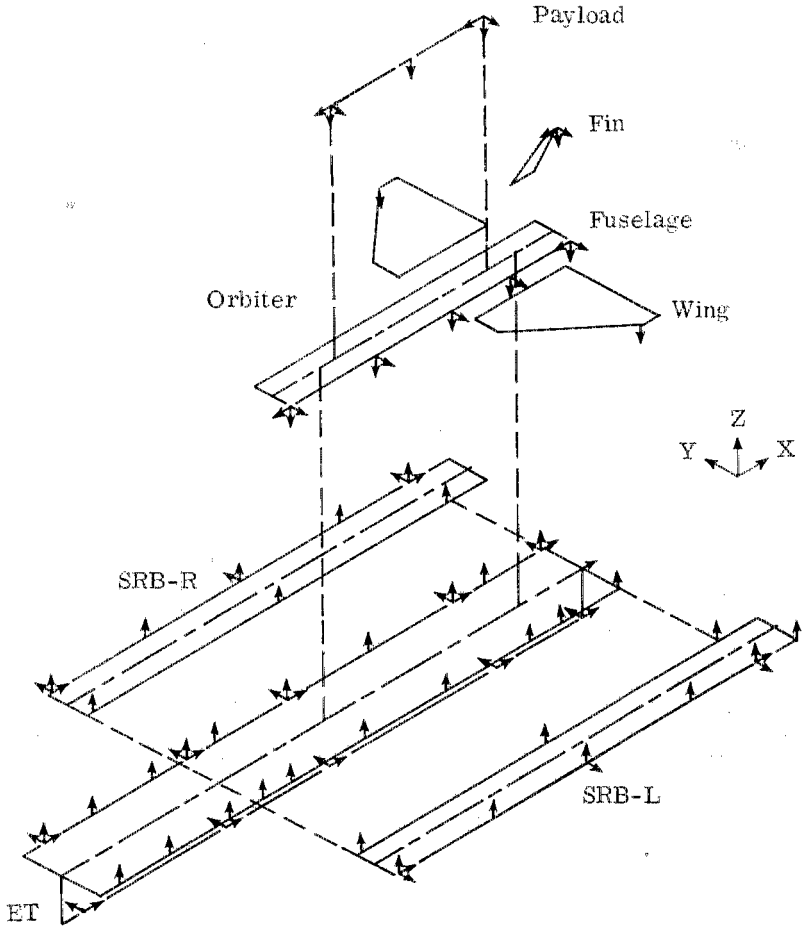

(b) Locations and directions of measurement.

Figure 20.- Installation of accelerometers on 1/8-scale shuttle model.

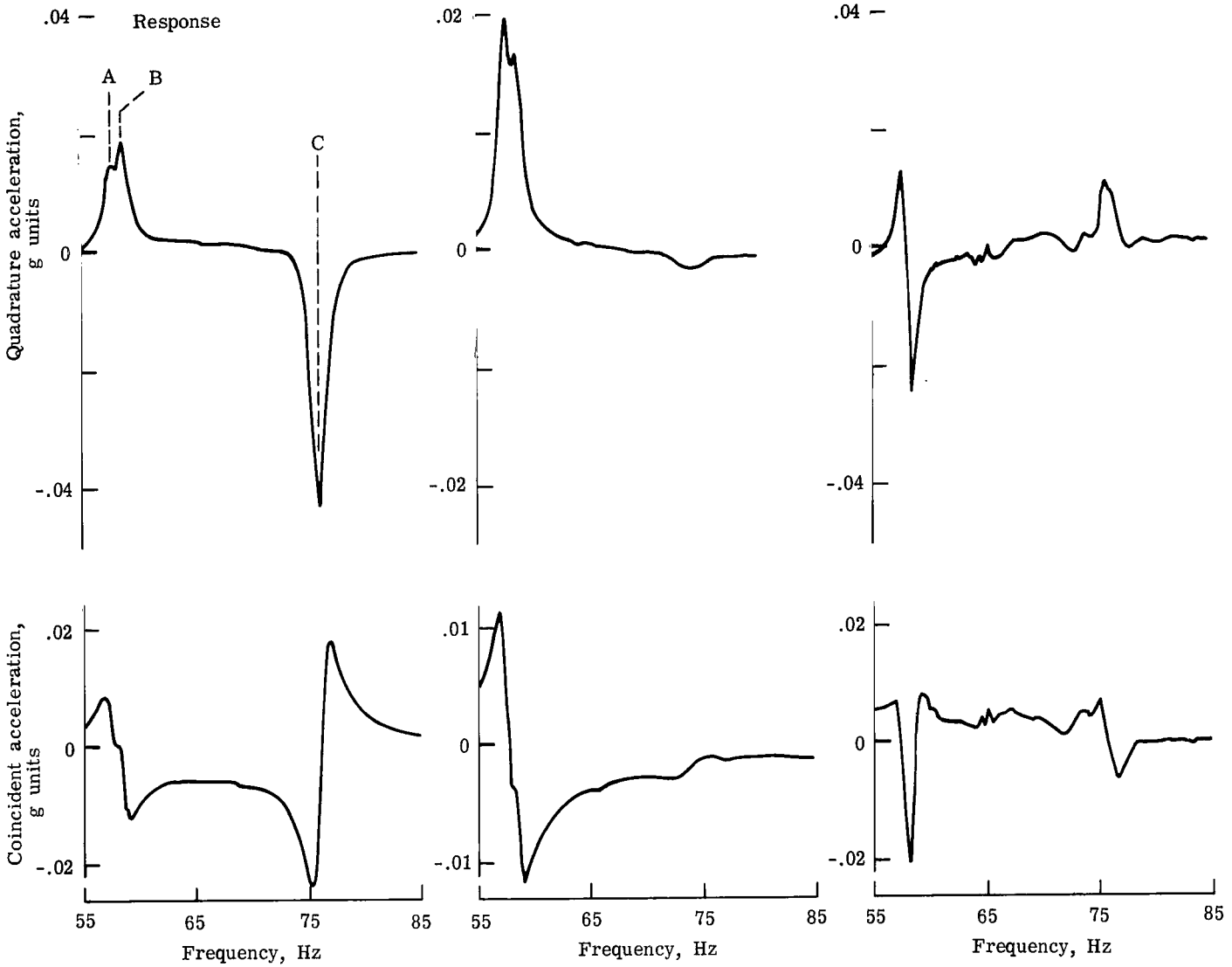

(a) Solid-rocket booster. (b) External tank. (c) Orbiter.

Figure 21.- Typical coincident-quadrature data for 1/8-scale shuttle model at lift-off.

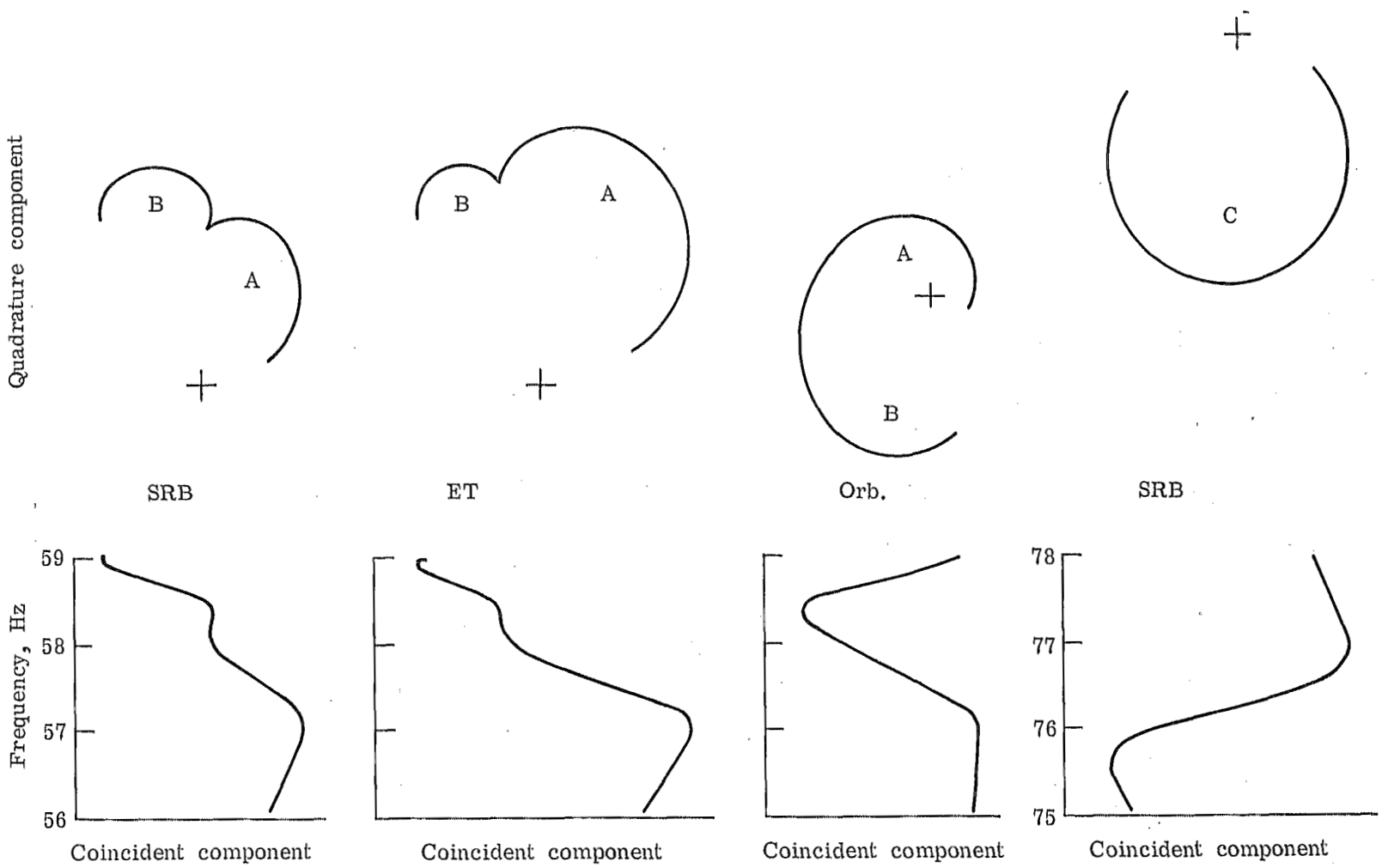

Figure 22.- Typical phase-plane data for 1/8-scale shuttle model at lift-off. Responses A, B, and C.

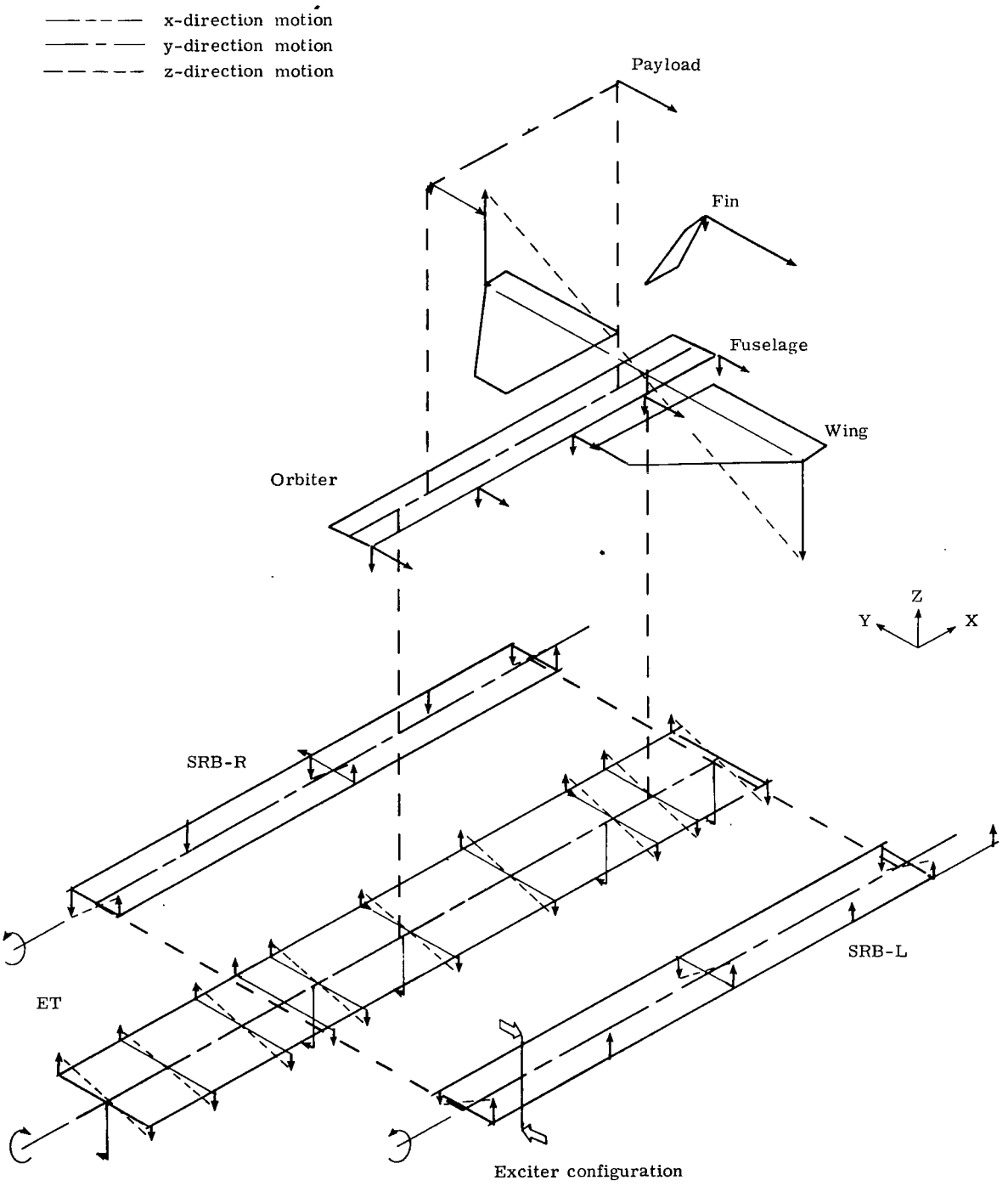

(a) 14.03 Hz, mode 1.

Figure 23.- Measured mode shapes for mated 1/8-scale shuttle model at lift-off.

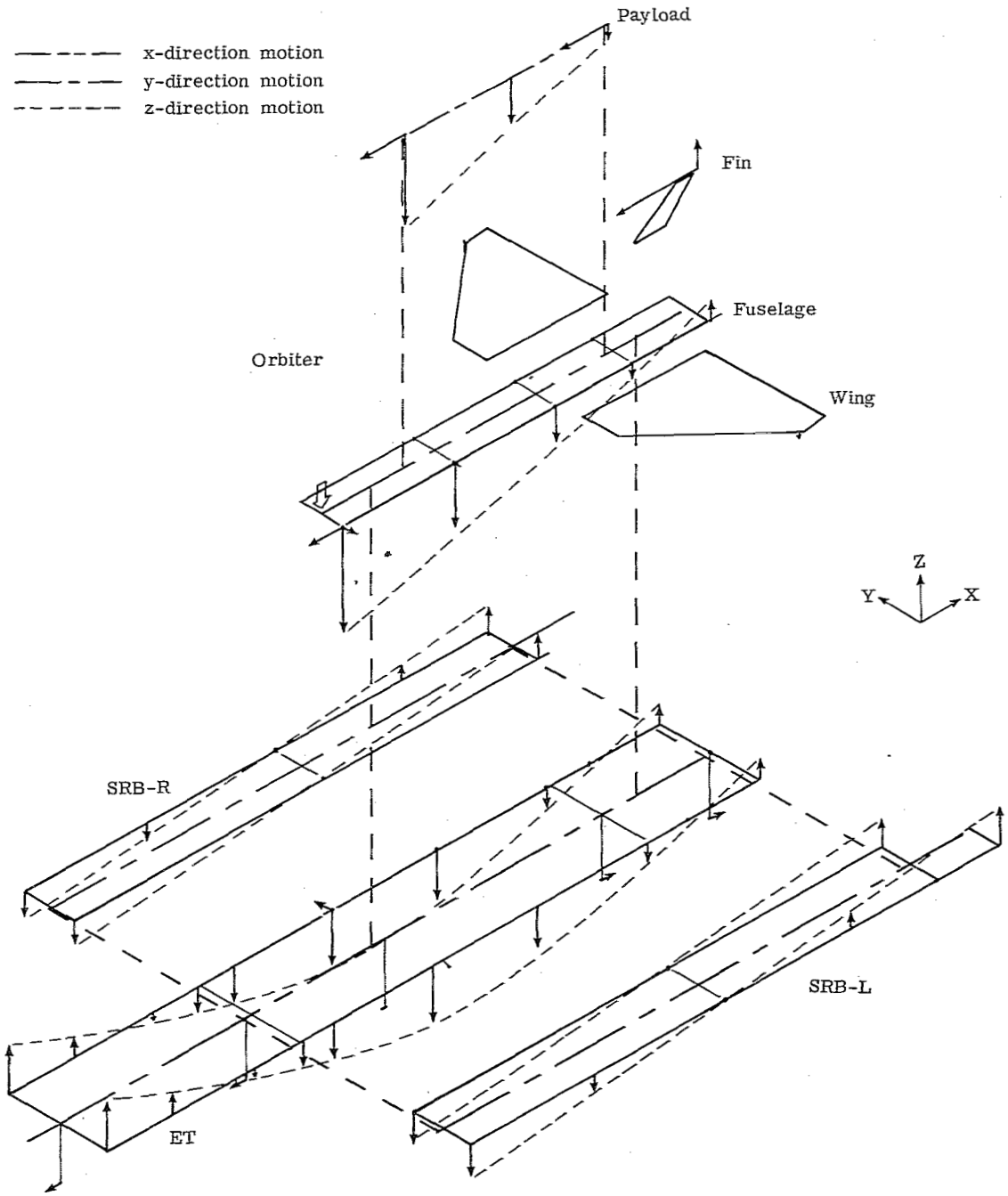

(b) 17.50 Hz, mode 3.

Figure 23.- Continued.

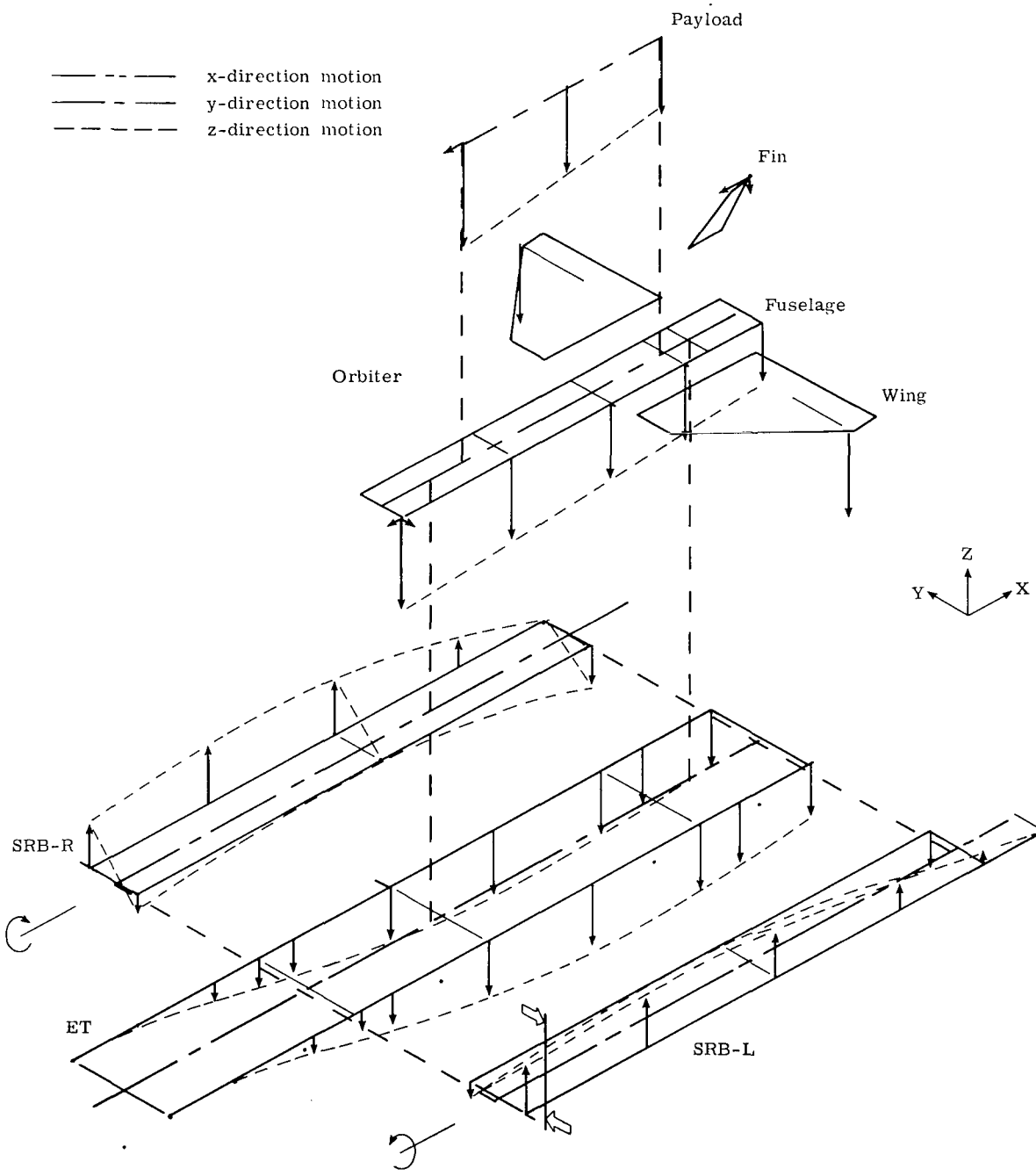

(c) 17.86 Hz, mode 4.

Figure 23.- Continued.

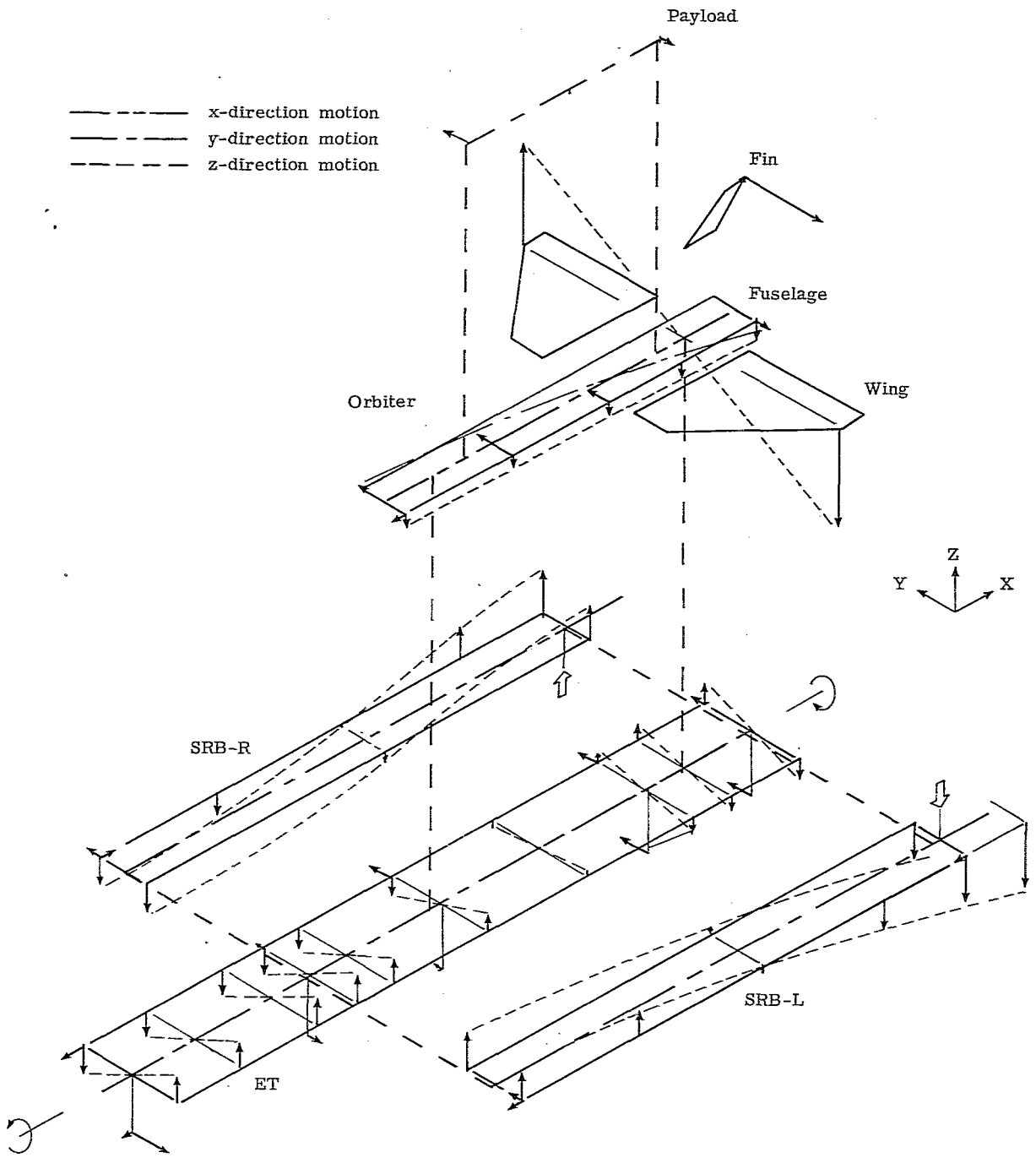

(d) 24.37 Hz, mode 7.

Figure 23.- Continued.

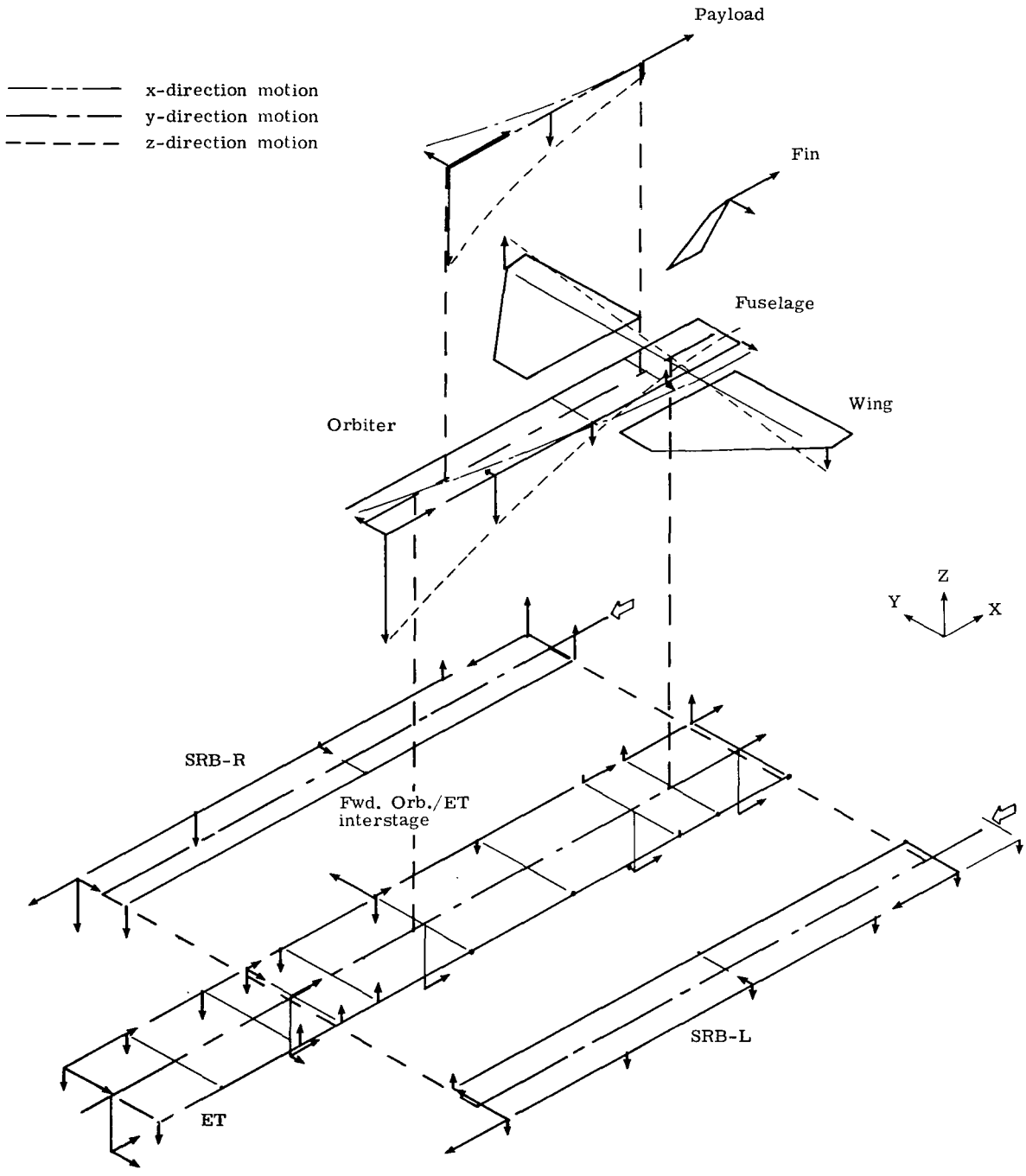

(e) 25.32 Hz, mode 8.

Figure 23.- Continued.

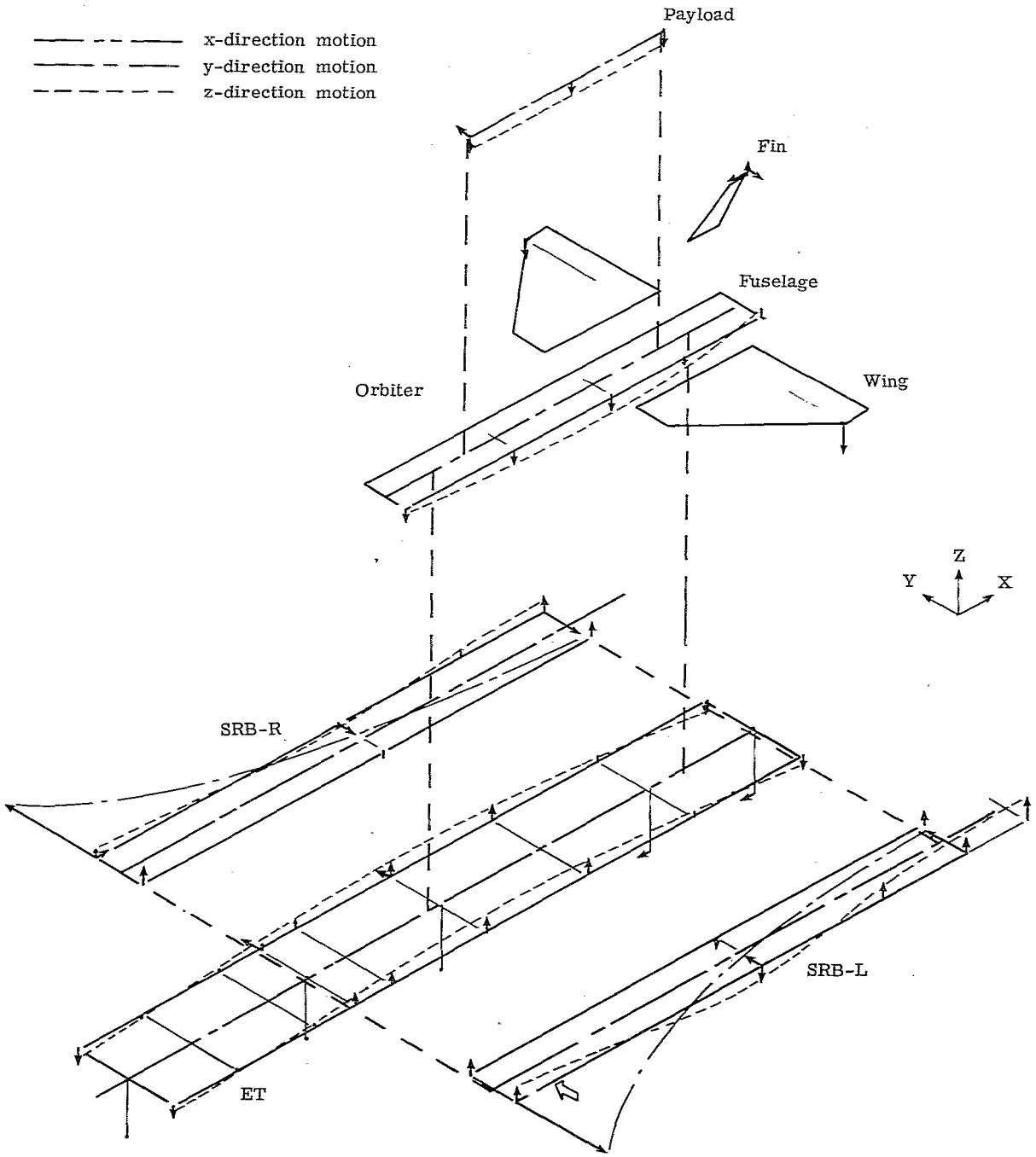

(f) 38.22 Hz, mode 12.

Figure 23.- Continued.

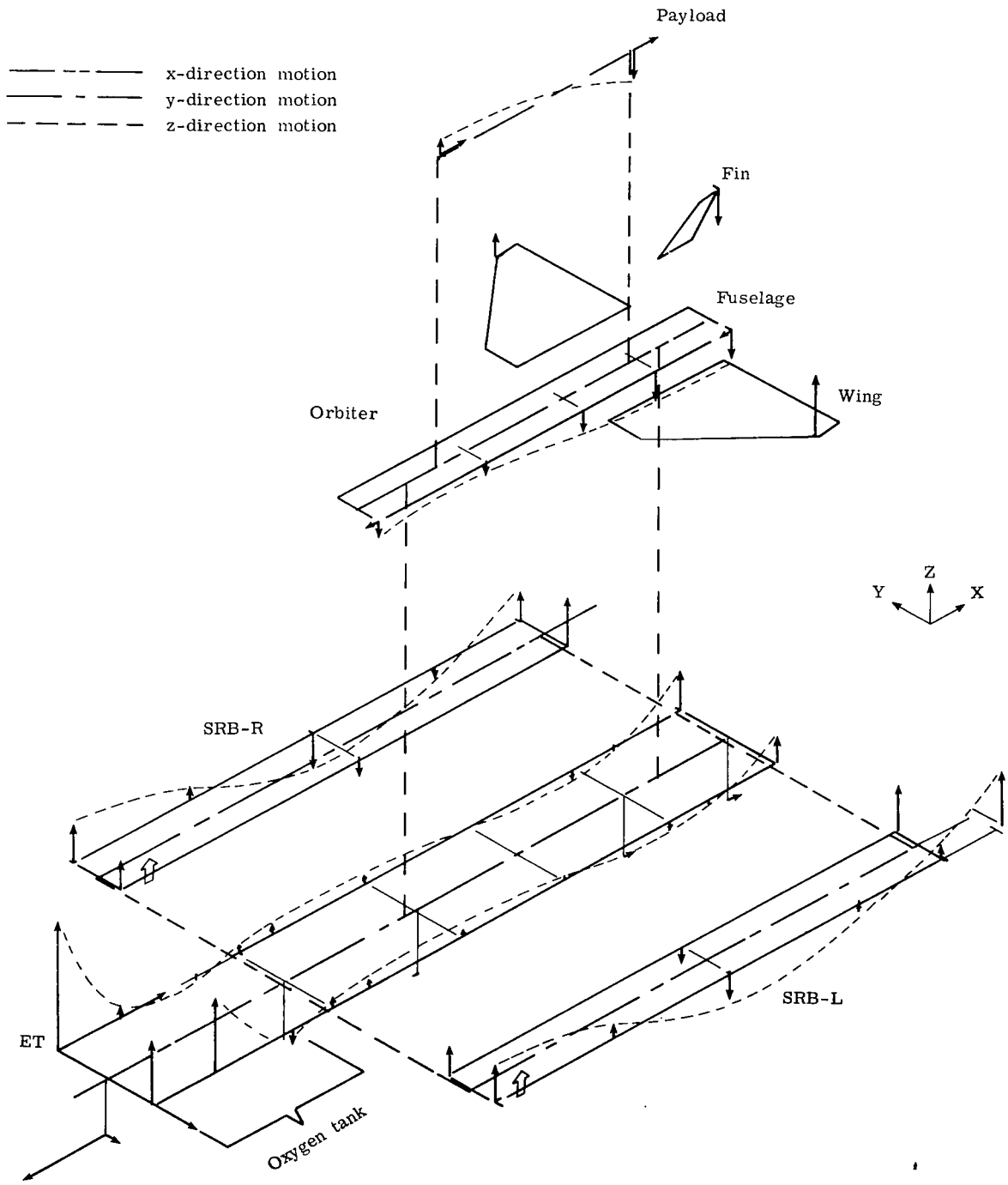

(g) 71.23 Hz, mode 21.

Figure 23.- Continued.

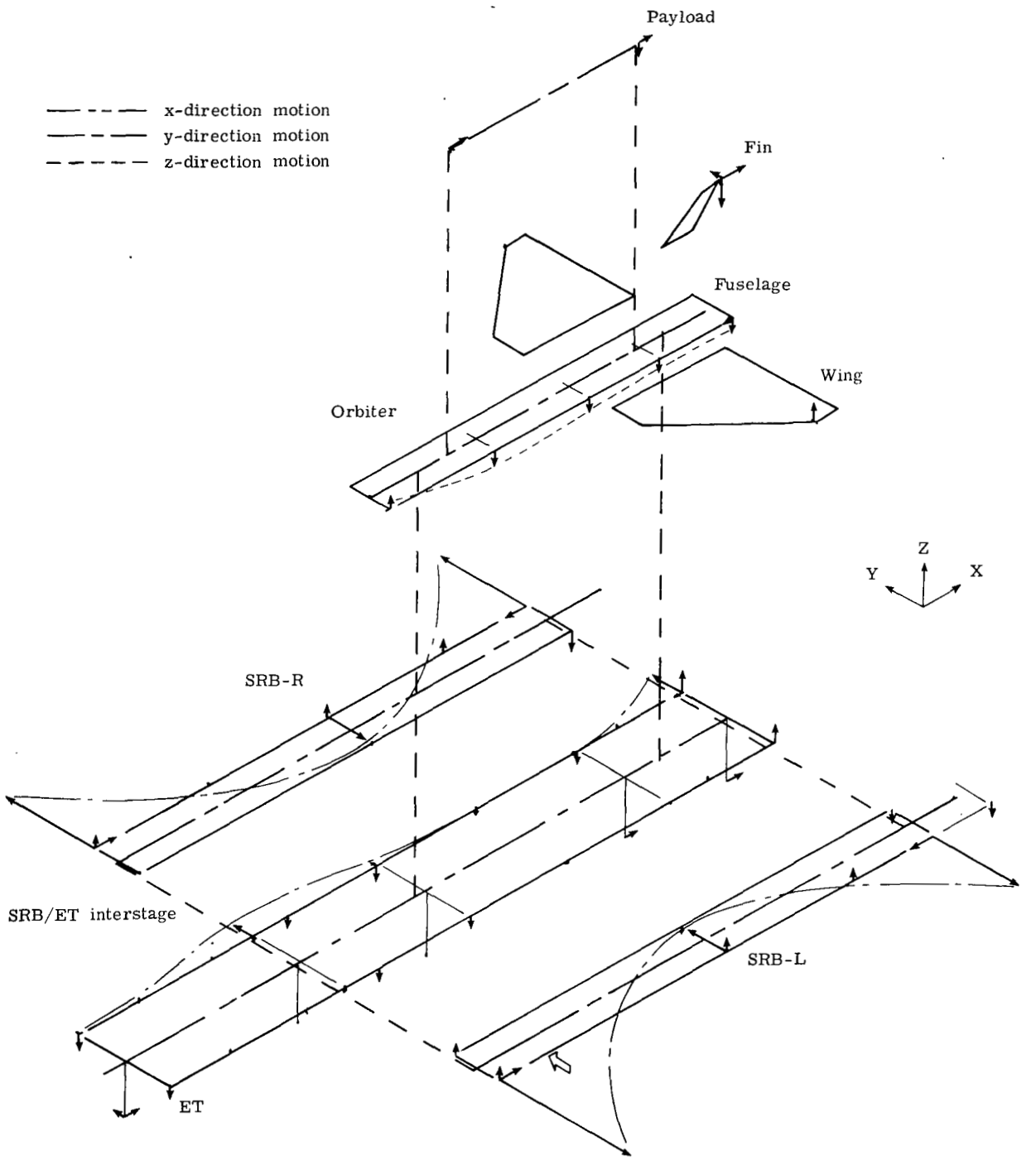

(h) 76.39 Hz, mode 23.

Figure 23.- Continued.

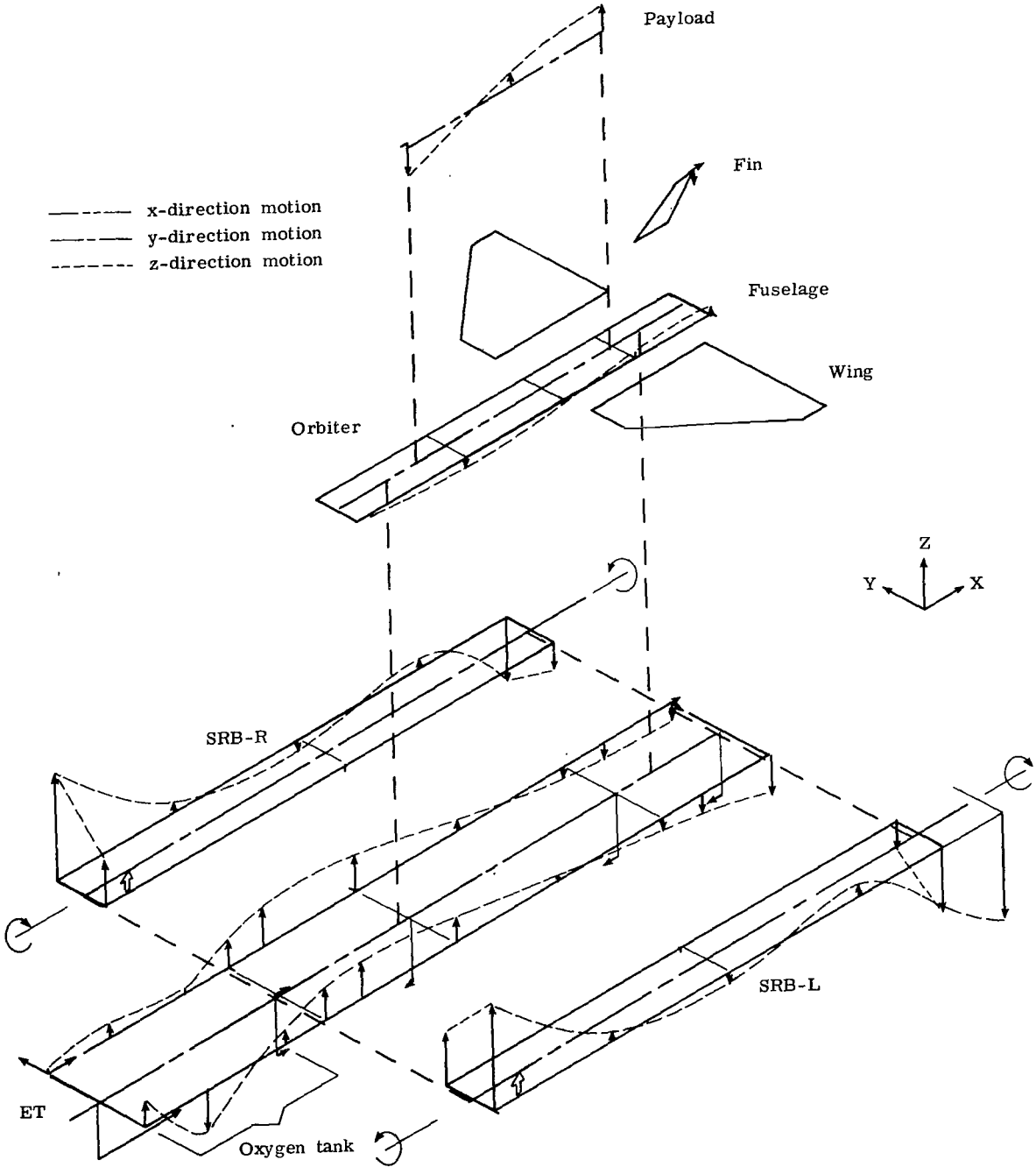

(i) 124.60 Hz, mode 28.

Figure 23.- Continued.

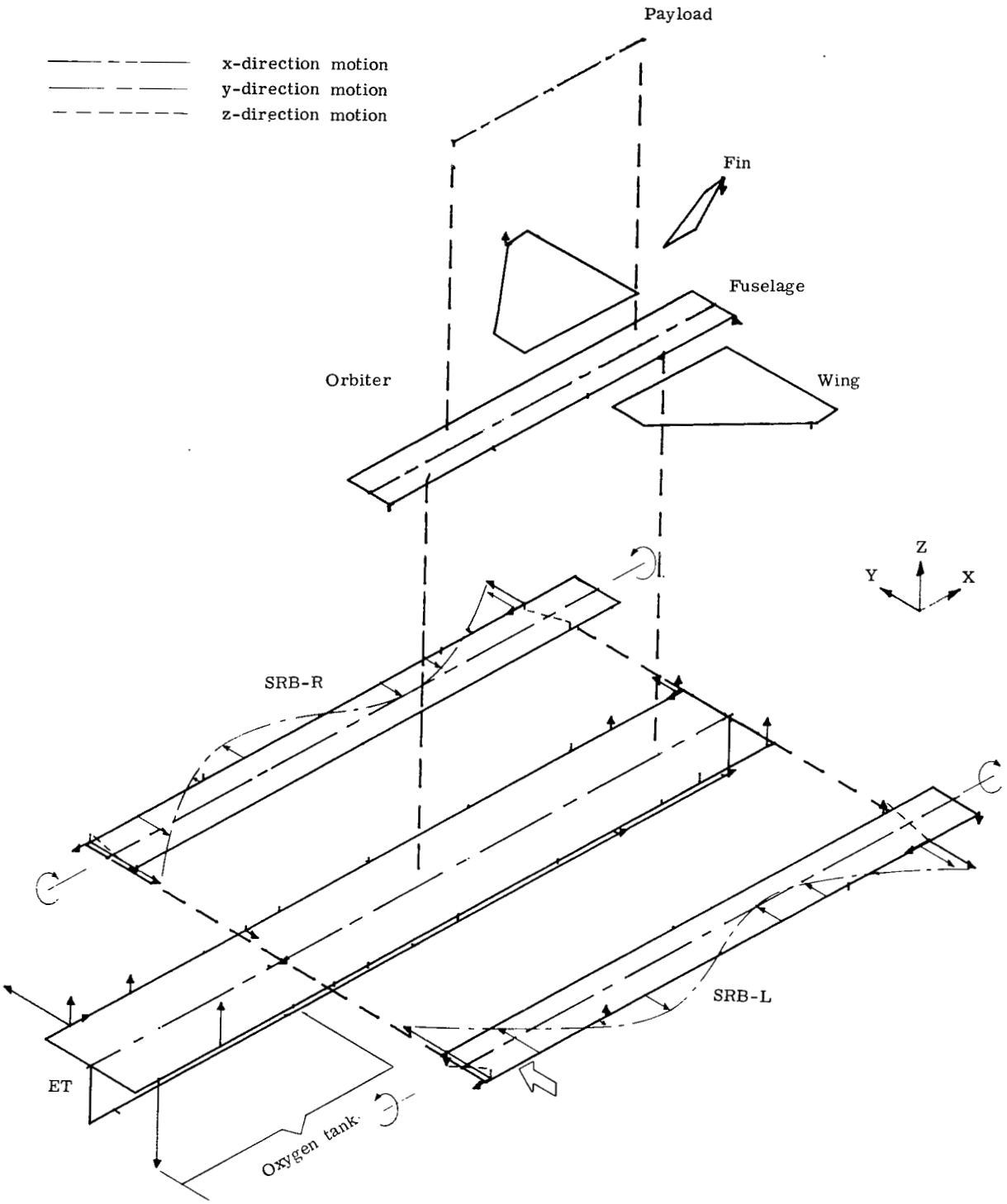

(j) 129.48 Hz, mode 29.

Figure 23.- Concluded.

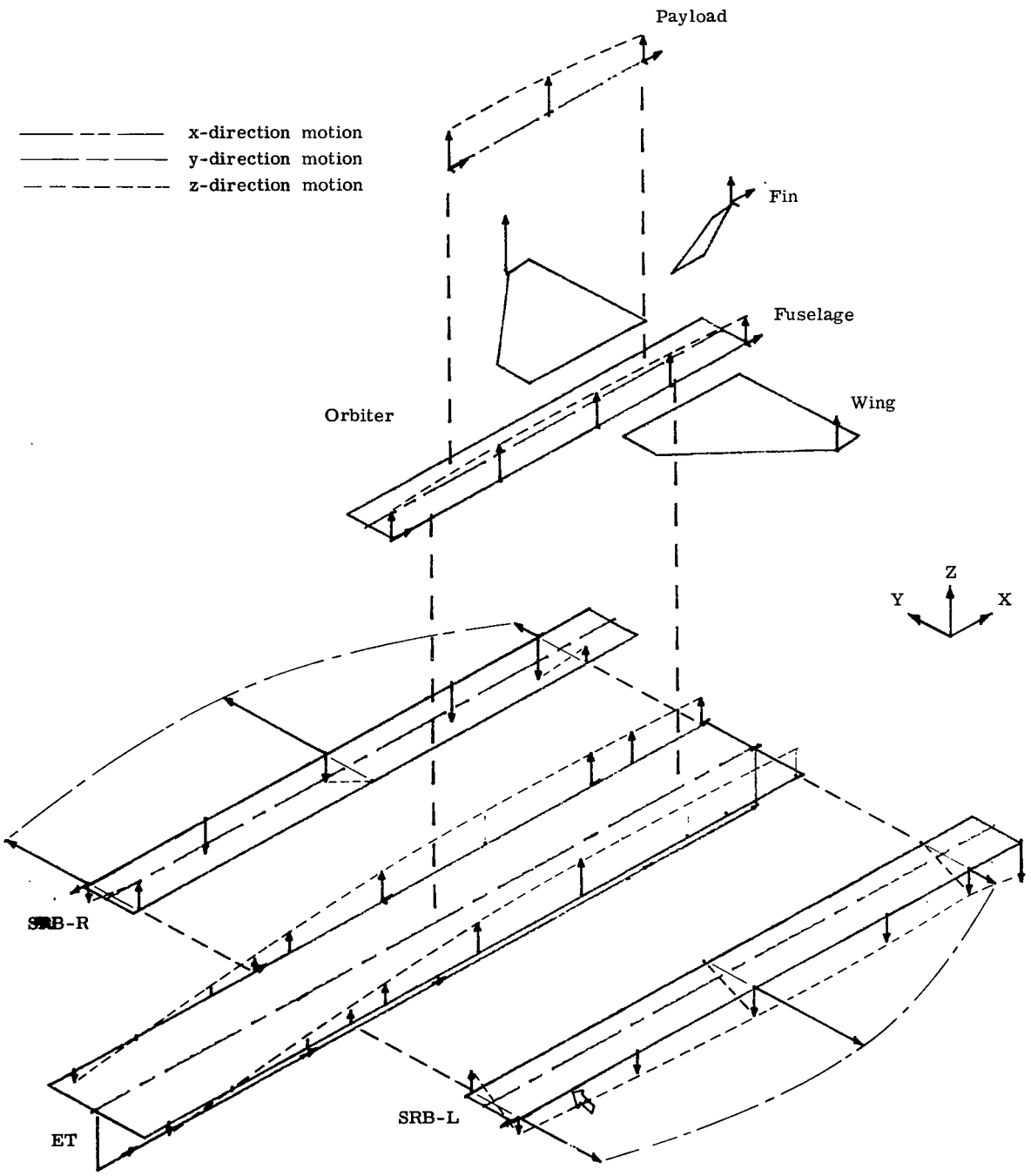

(a) 15.84 Hz, mode 2.

Figure 24.- Measured mode shapes for mated 1/8-scale shuttle model at mid-boost (q_{max}).

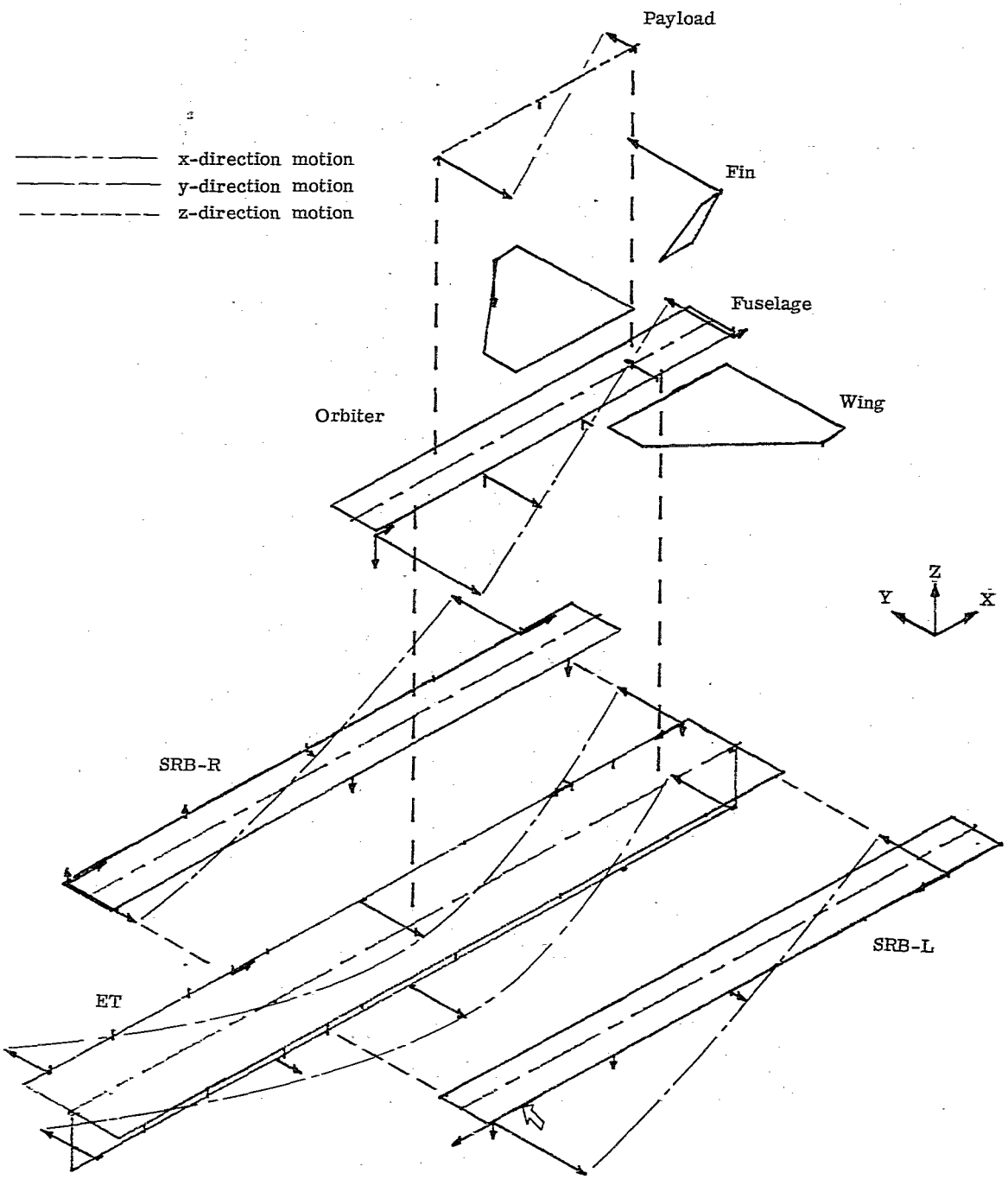

(b) 19.39 Hz, mode 4.

Figure 24.- Continued.

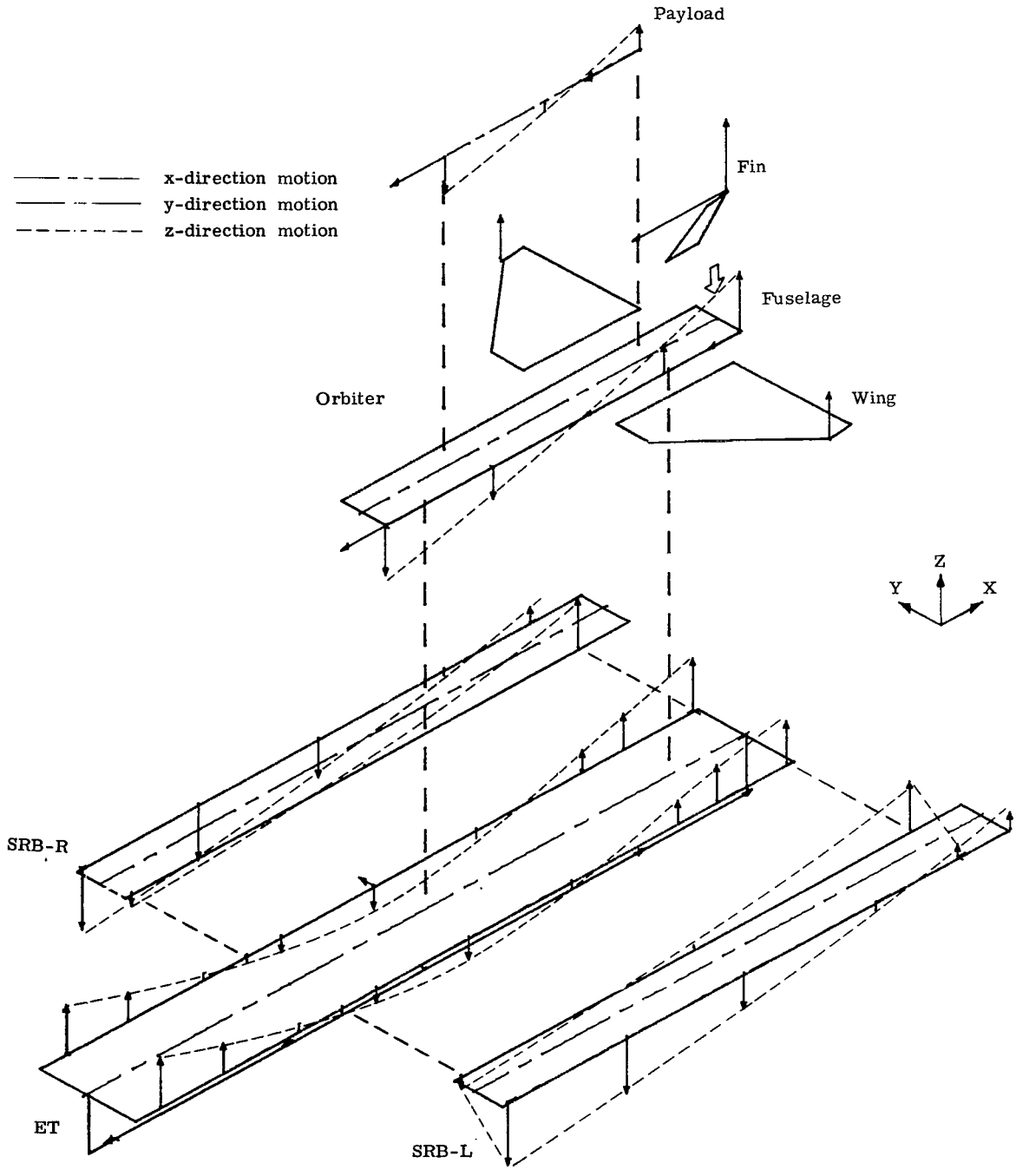

(c) 19.90 Hz, mode 5.

Figure 24.- Continued.

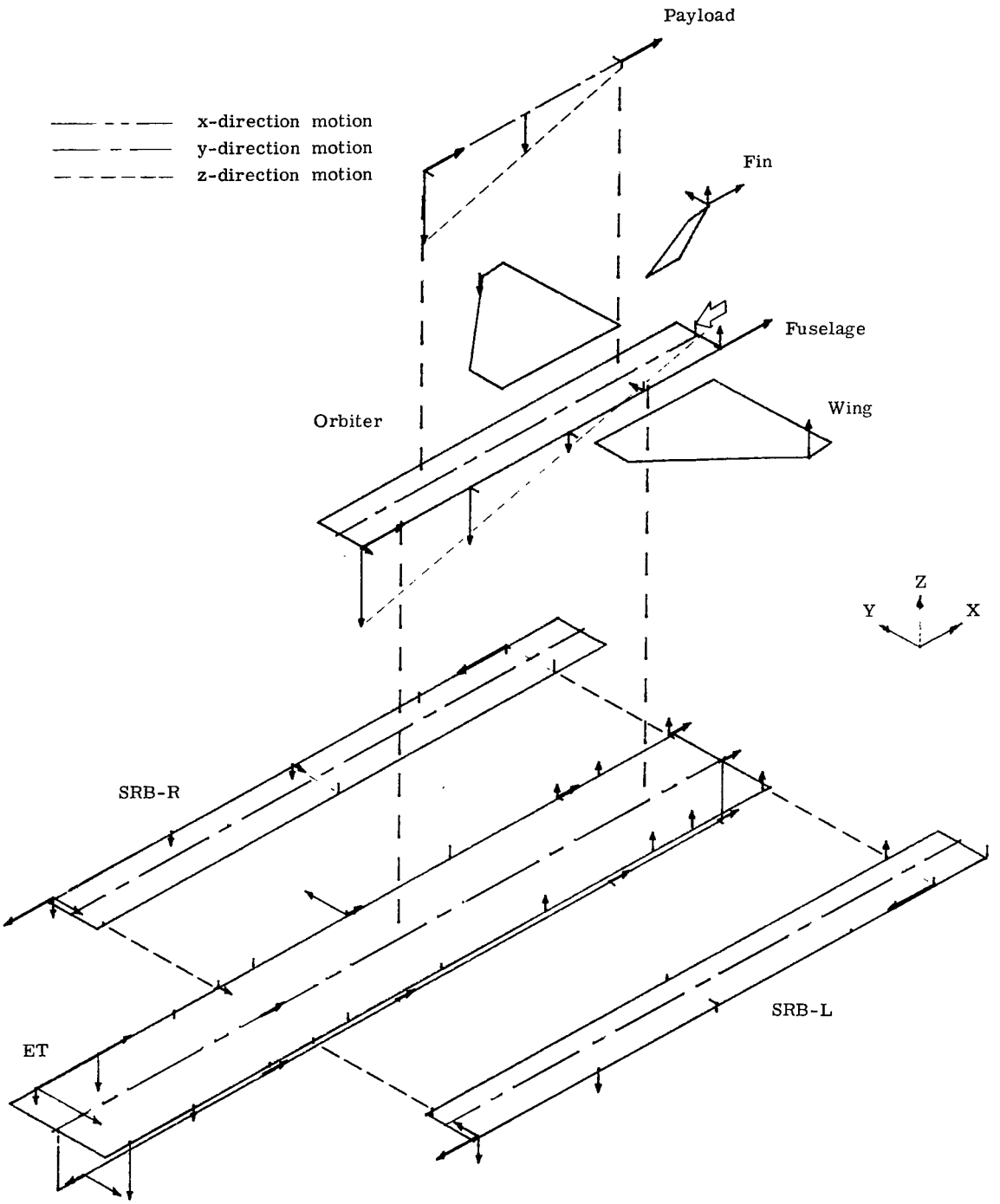

(d) 27.82 Hz, mode 8.

Figure 24.- Continued.

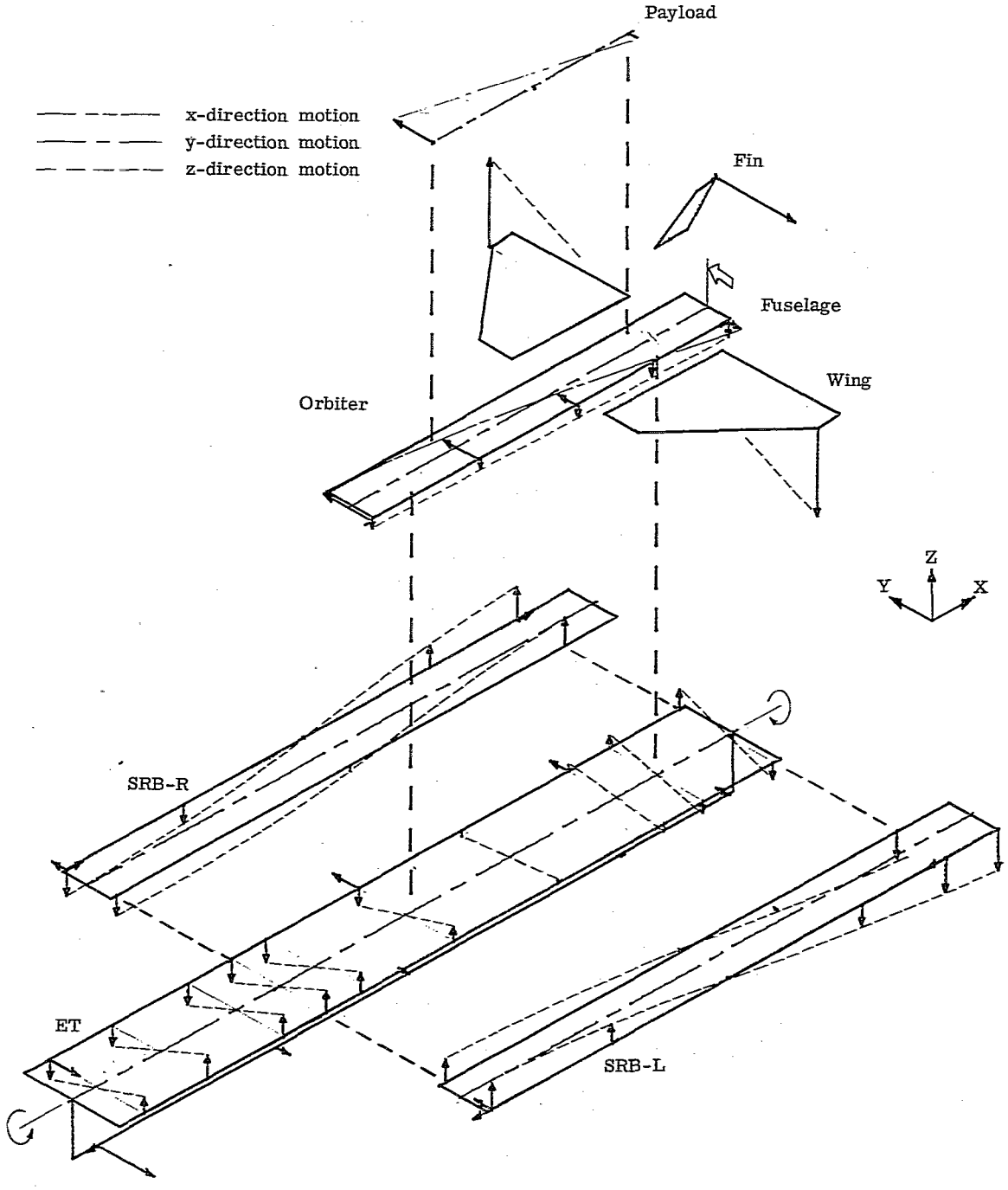

(e) 28.50 Hz, mode 9.

Figure 24.- Continued.

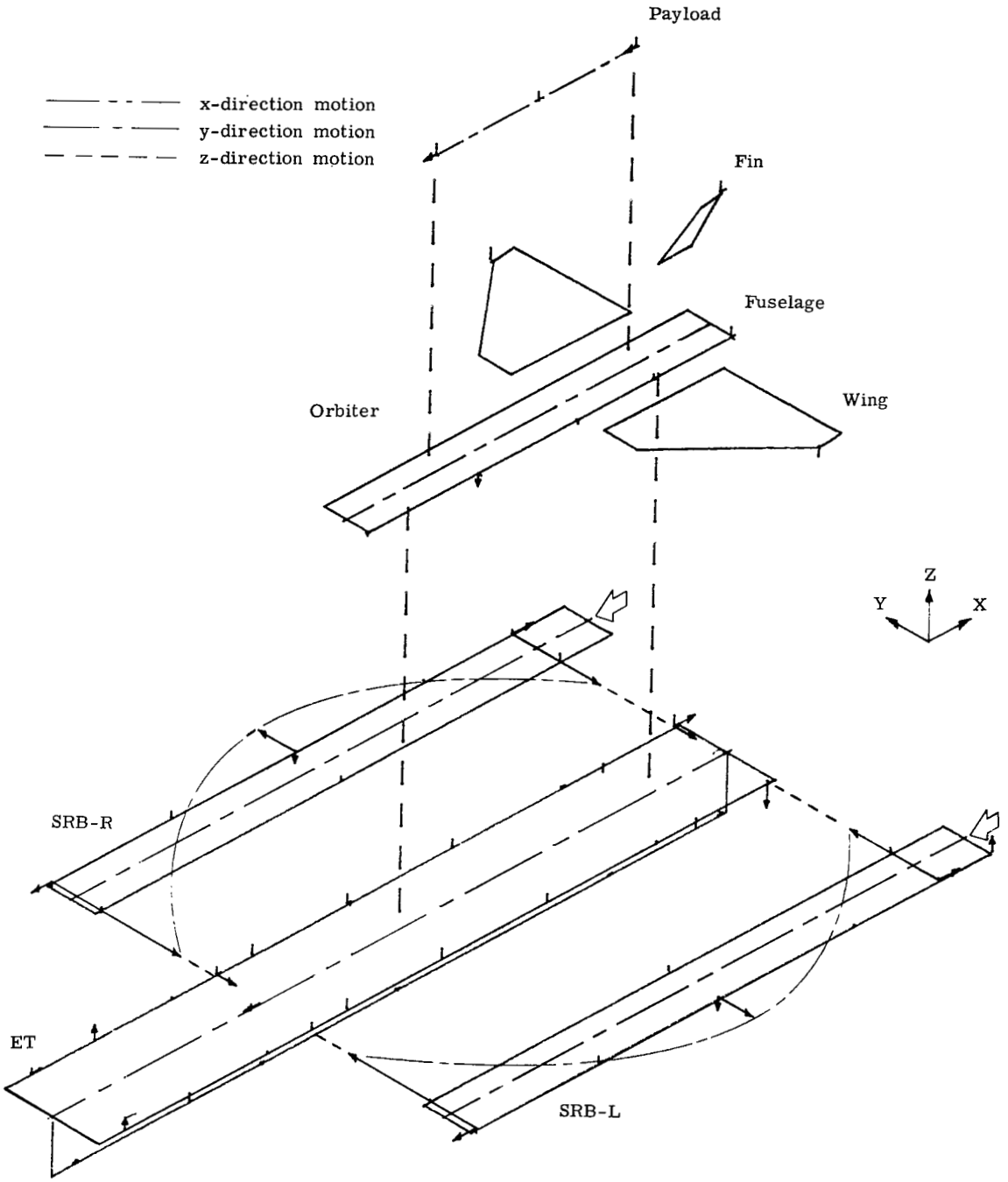

(f) 89.08 Hz, mode 23.

Figure 24.- Concluded.

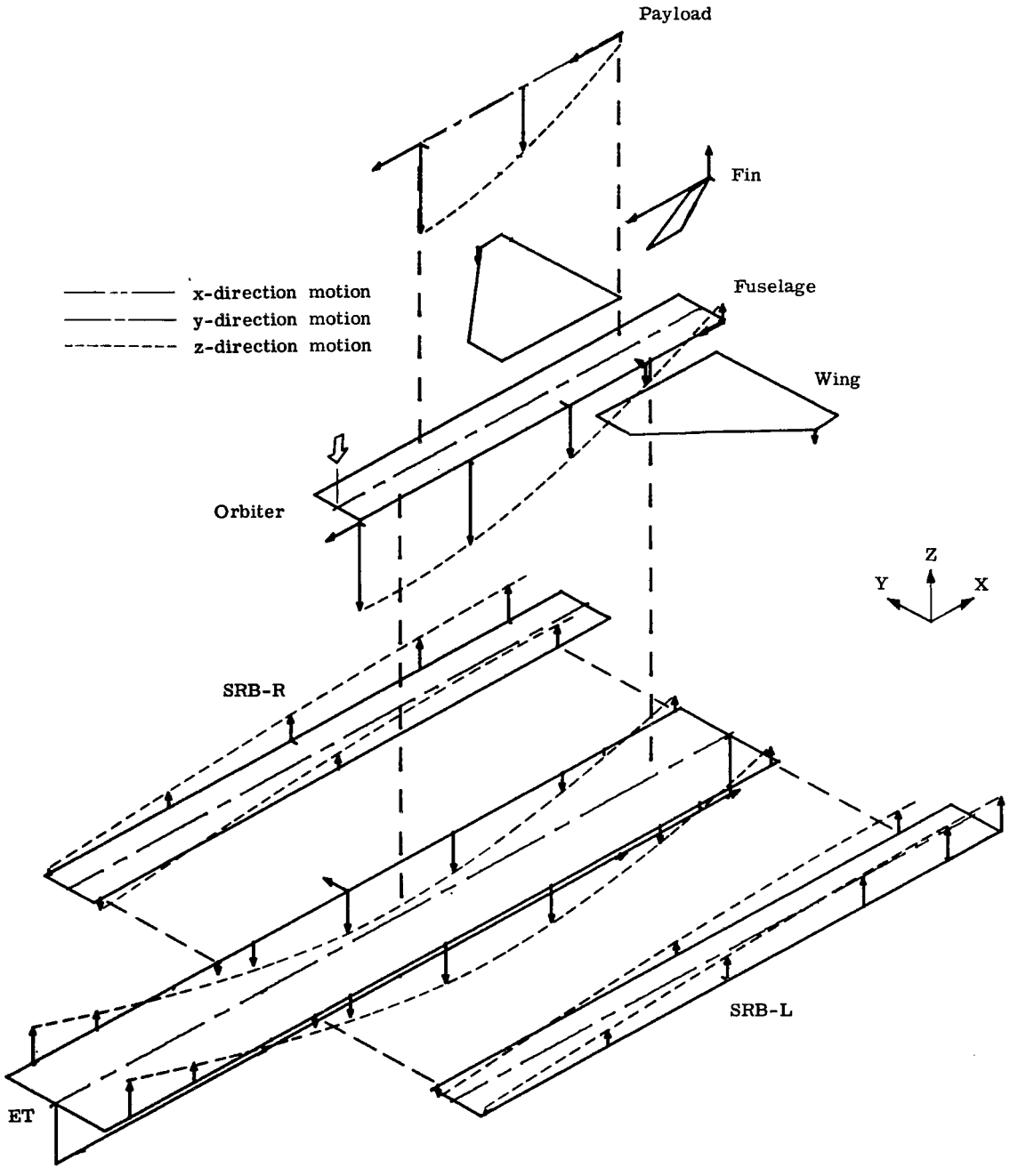

(a) 20.40 Hz, mode 2.

Figure 25.- Measured mode shapes for mated 1/8-scale shuttle model at end-boost (before SRB separation).

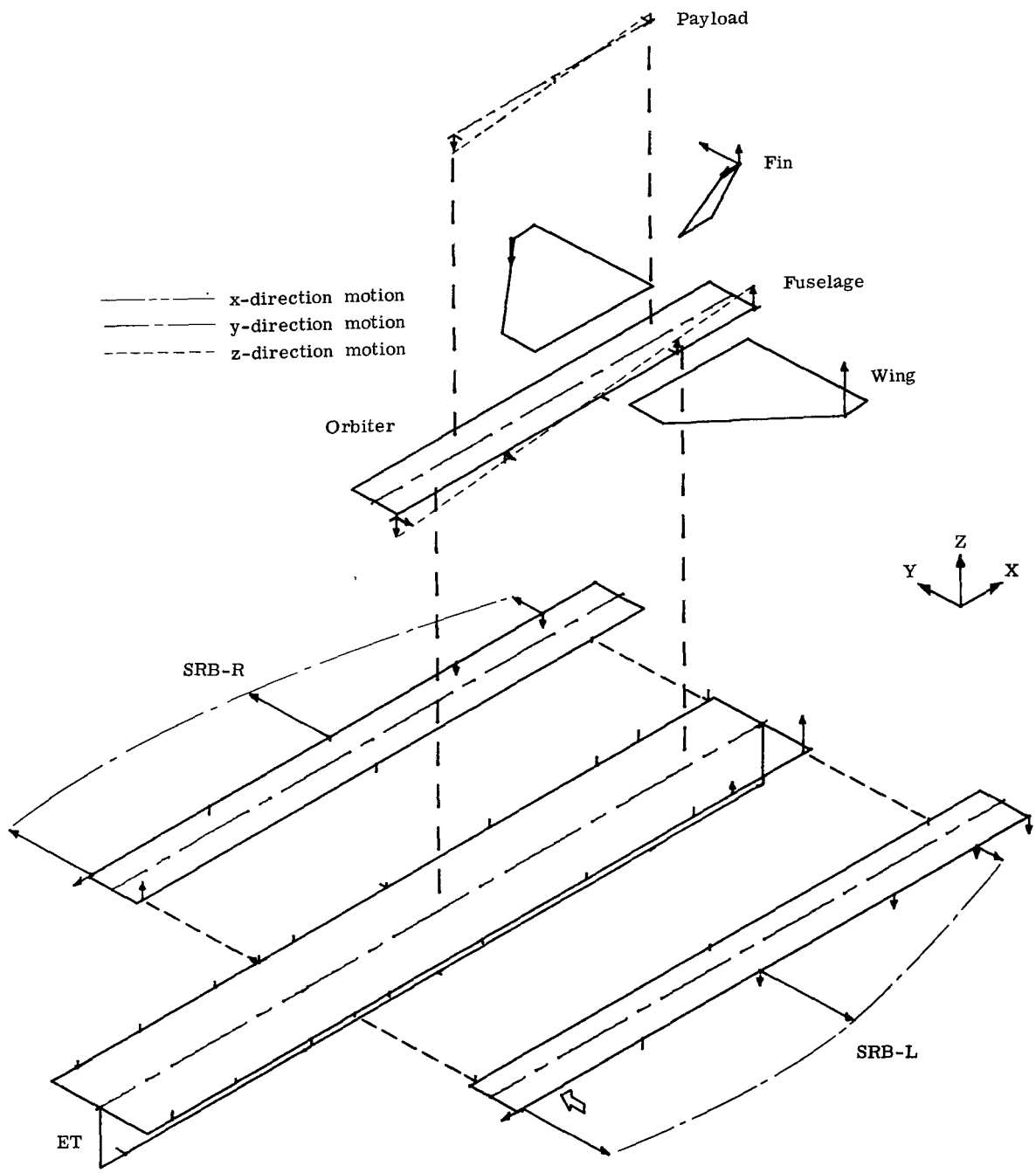

(b) 27.46 Hz, mode 5.

Figure 25.- Continued.

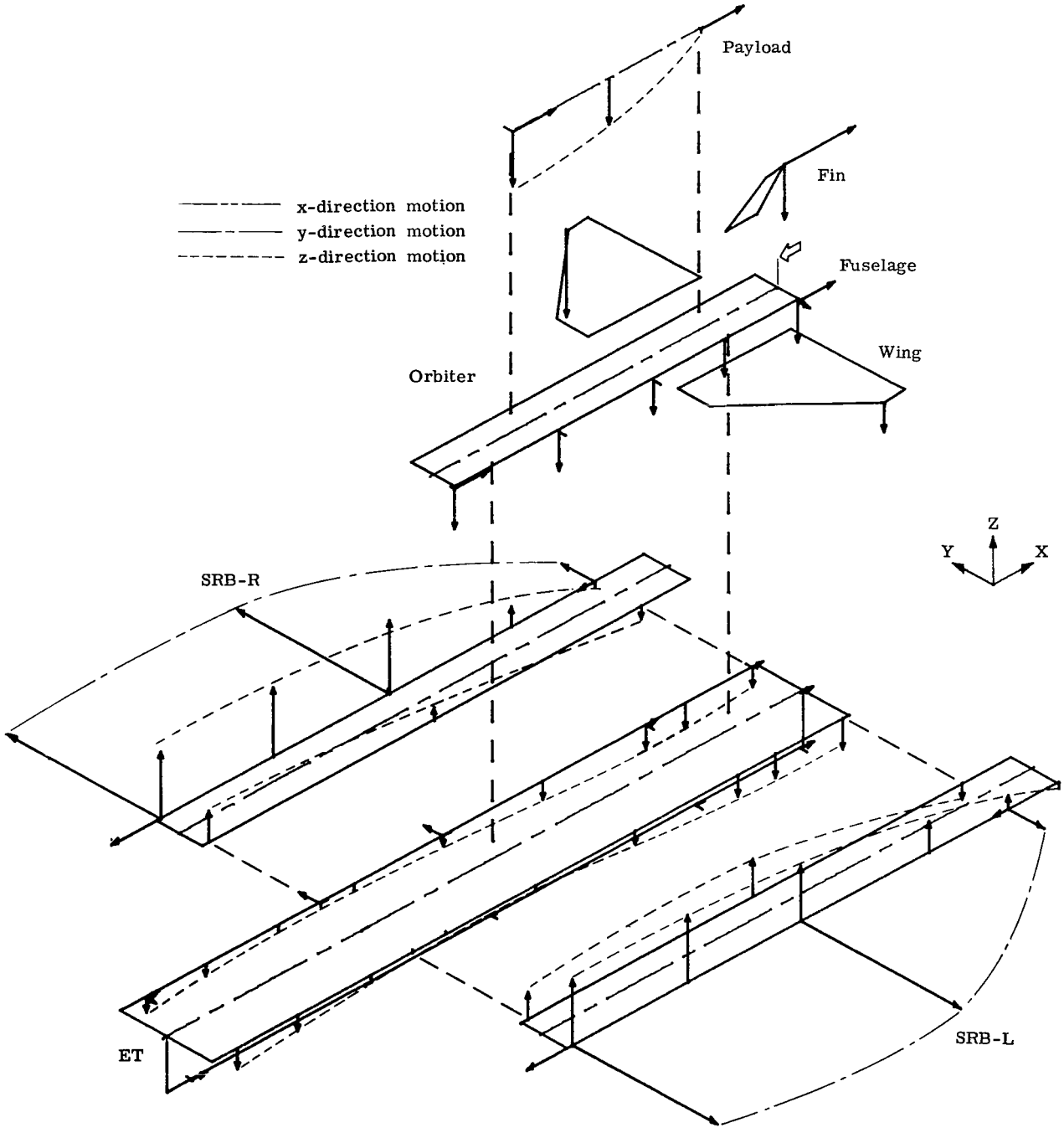

(c) 27.68 Hz, mode 6.

Figure 25.- Continued.

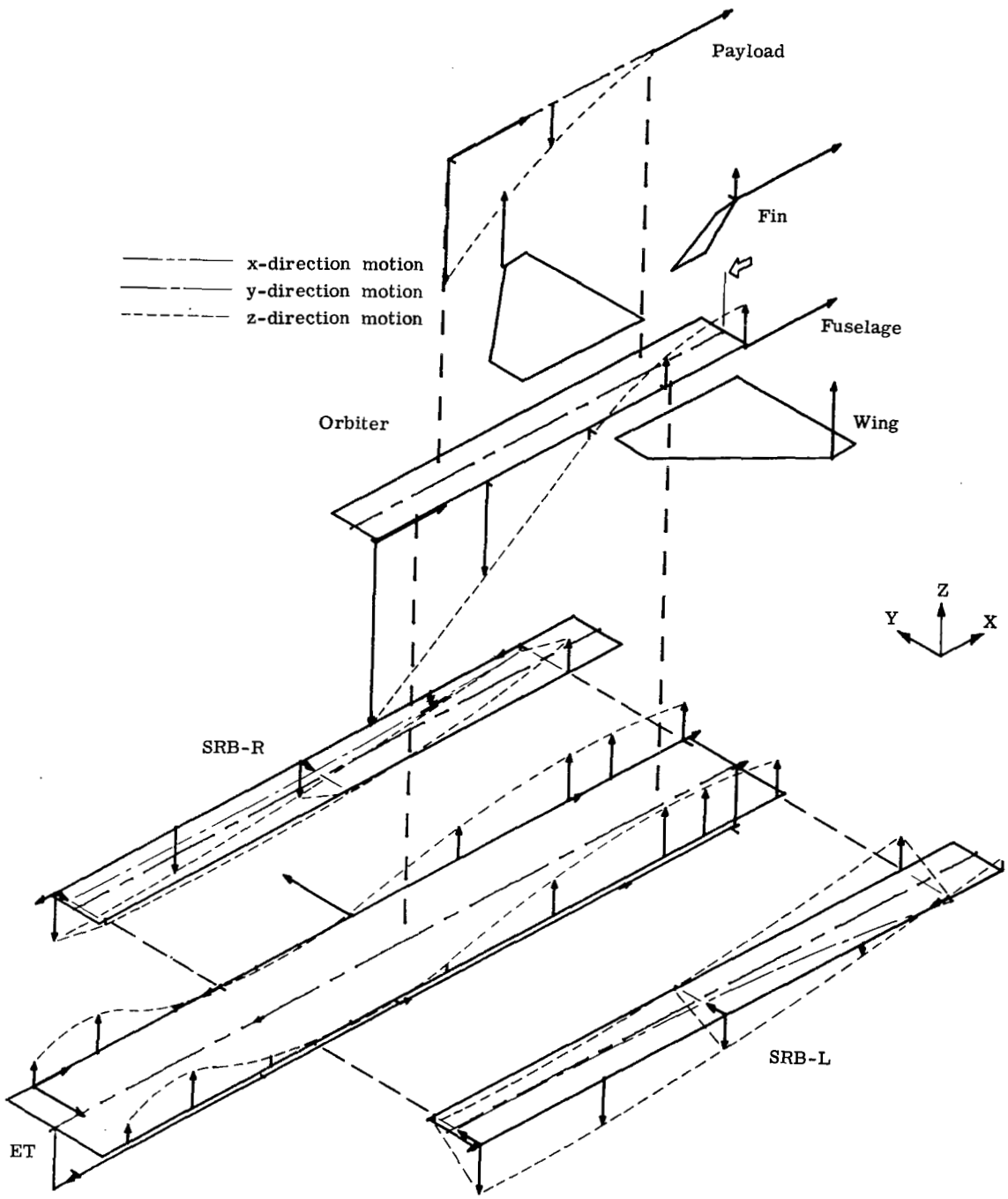

(d) 32.34 Hz, mode 8.

Figure 25.- Concluded.

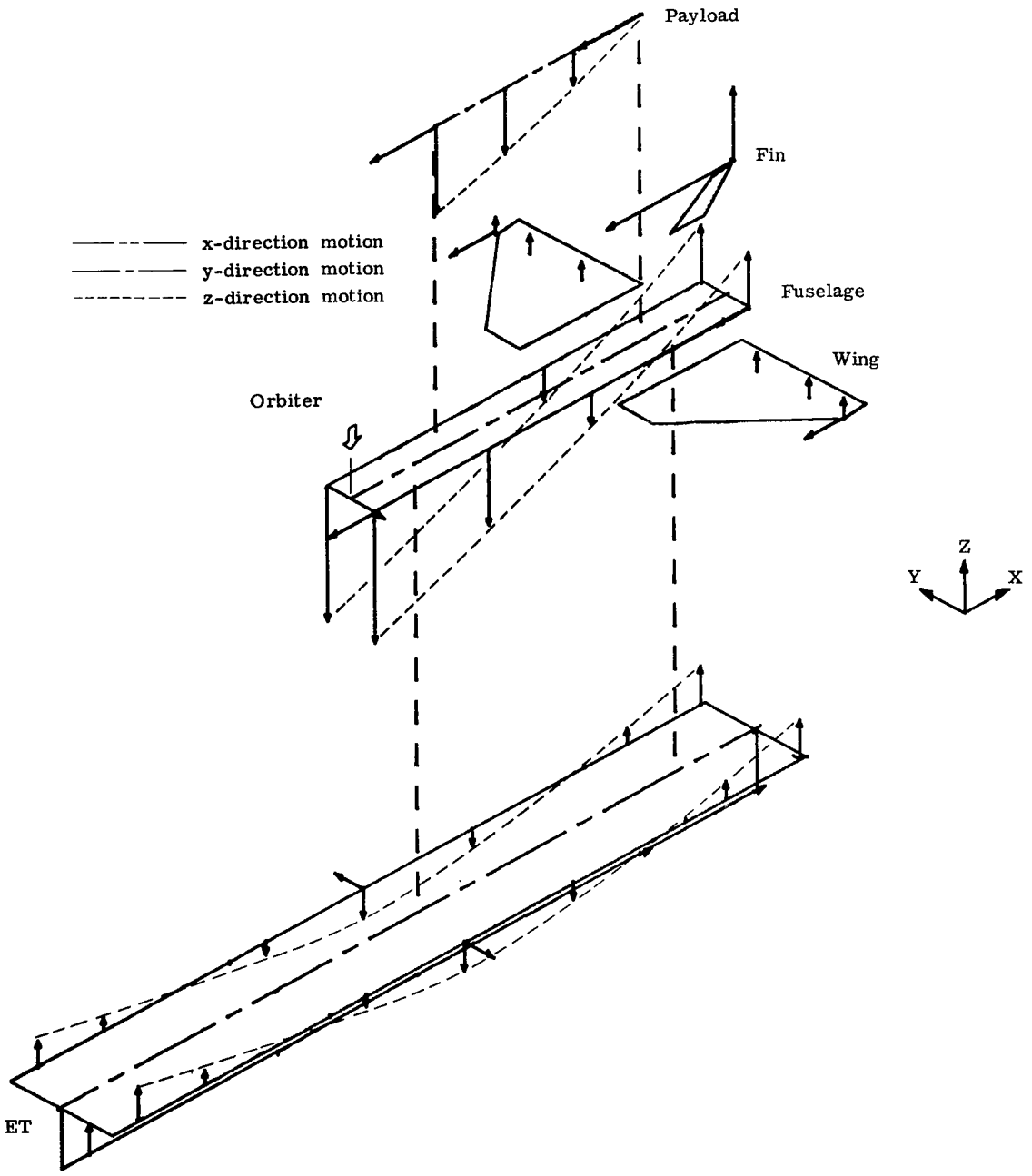

(a) 21.76 Hz, mode 1.

Figure 26.- Measured mode shapes for mated 1/8-scale shuttle model at end-boost (after SRB separation).

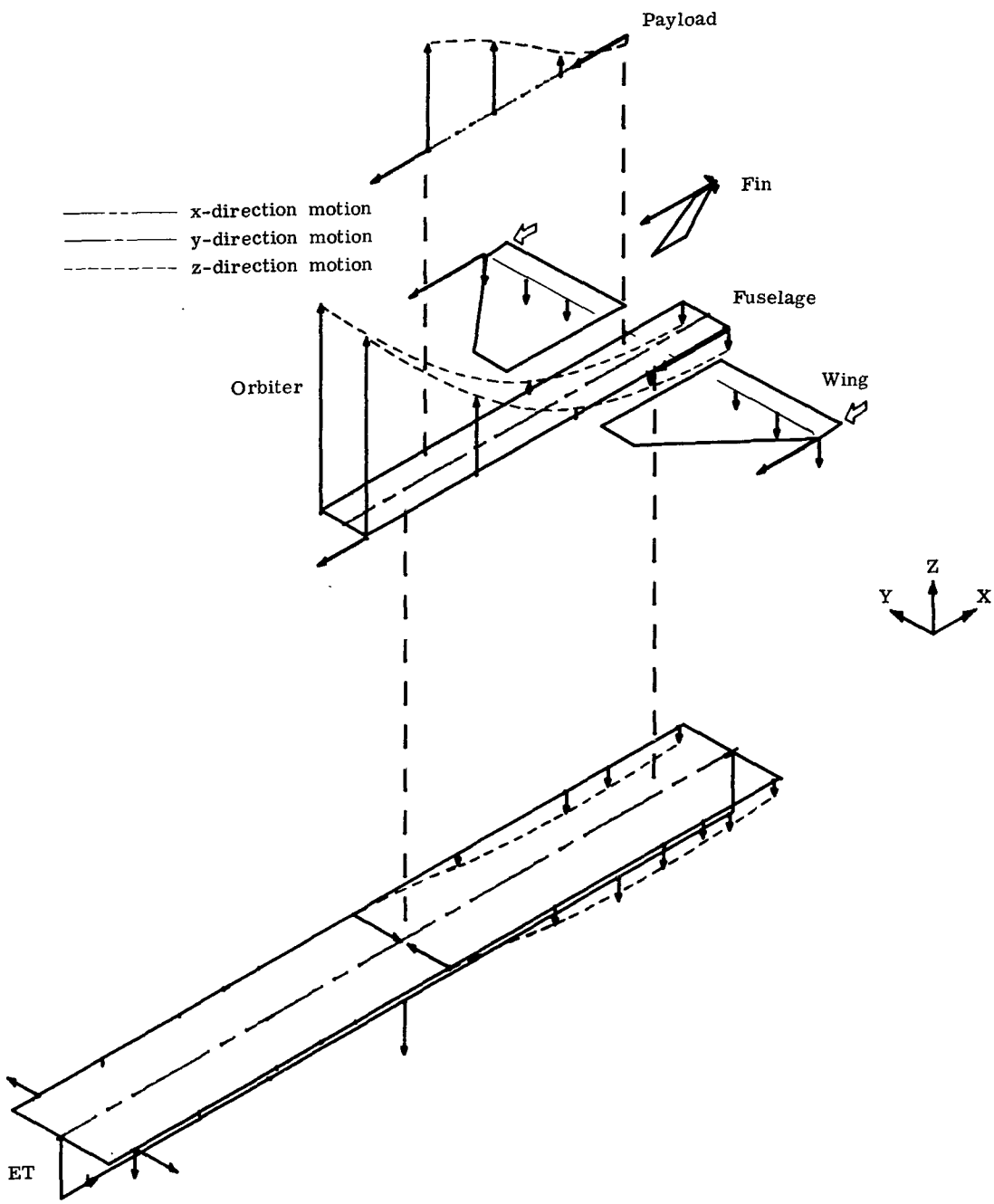

(b) 33.00 Hz, mode 3.

Figure 26.- Continued.

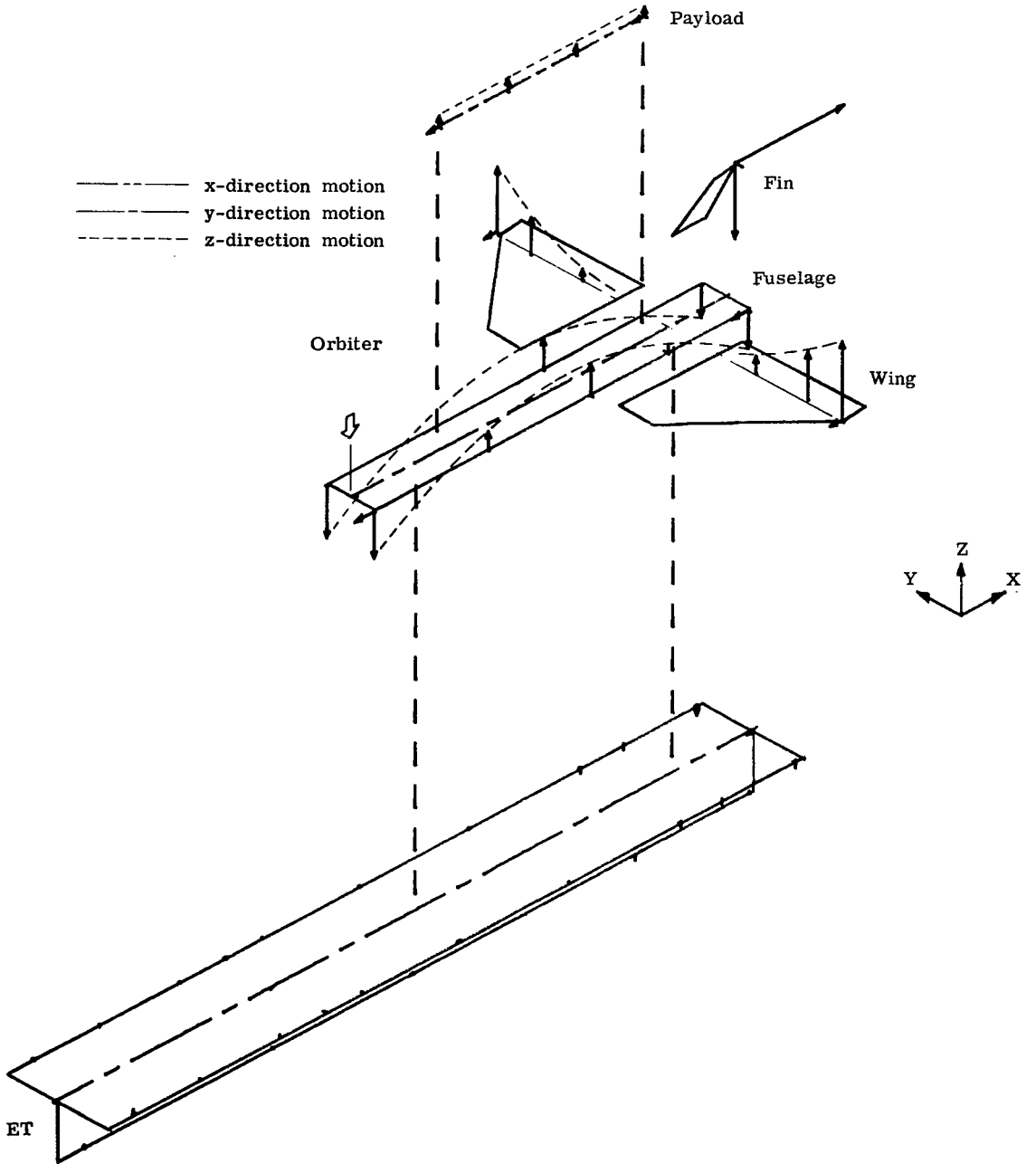

(c) 45.28 Hz, mode 6.

Figure 26.- Continued.

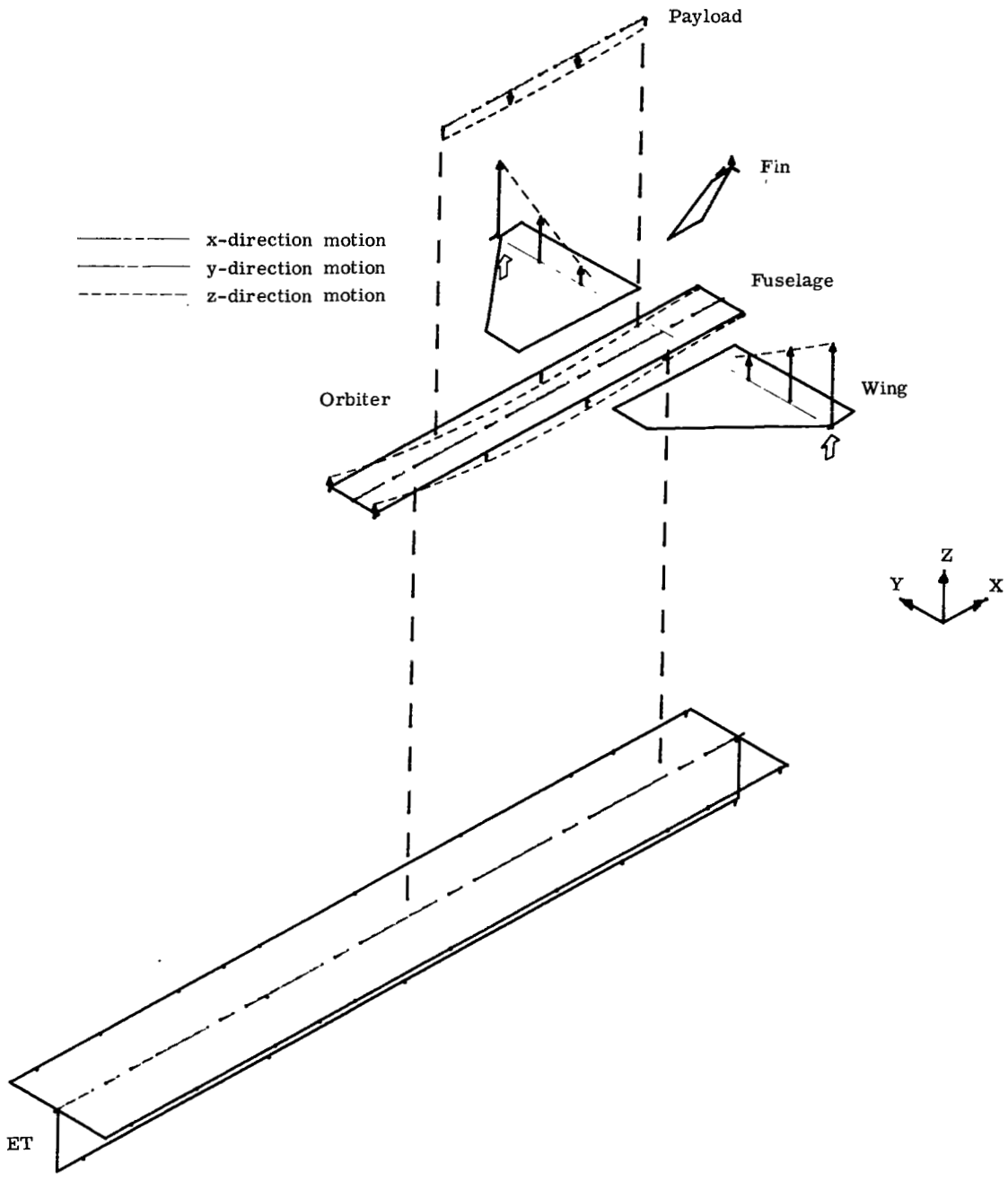

(d) 50.08 Hz, mode 7.

Figure 26.- Continued.

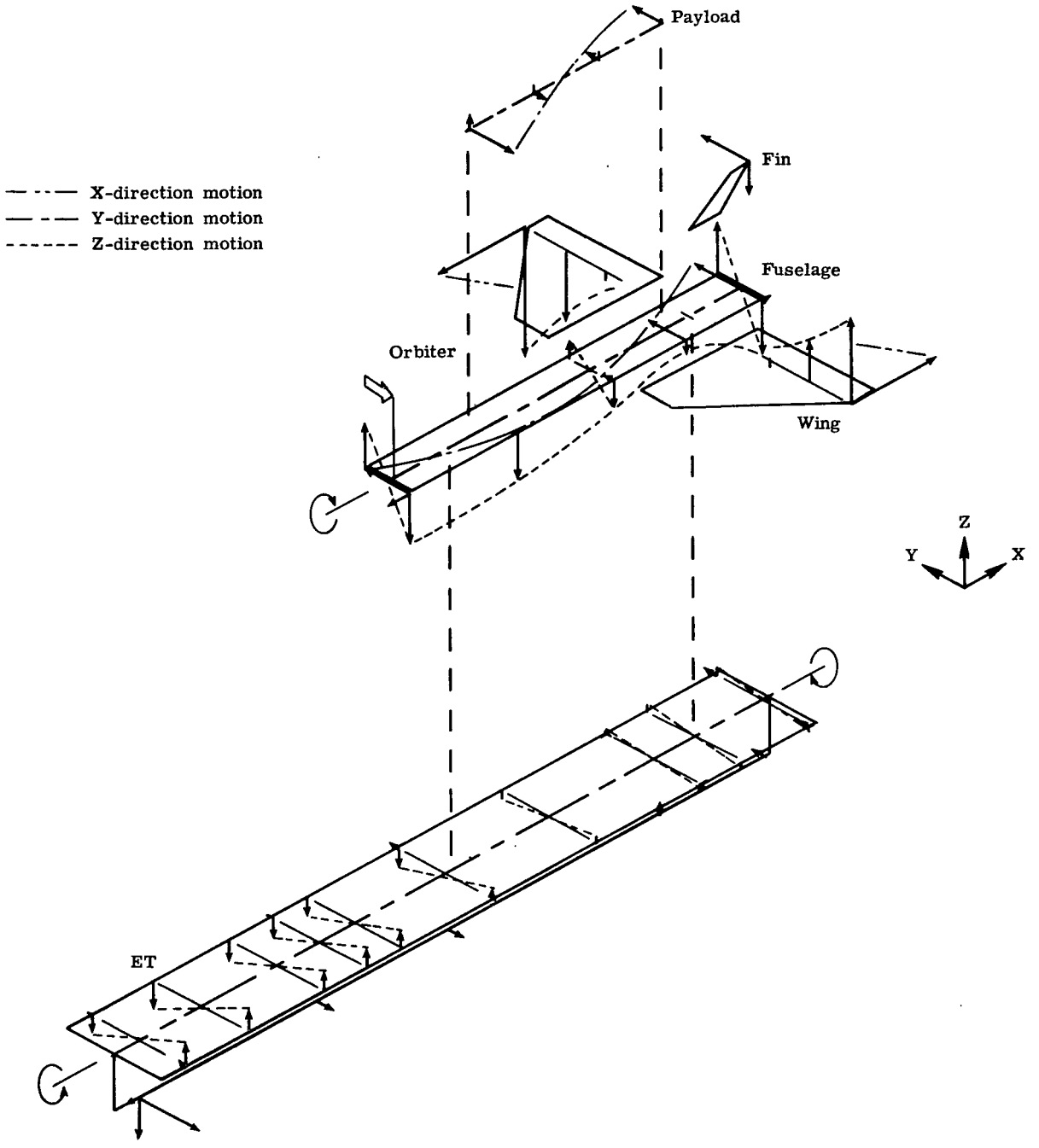

(e) 80.10 Hz, mode 14.

Figure 26.- Continued.

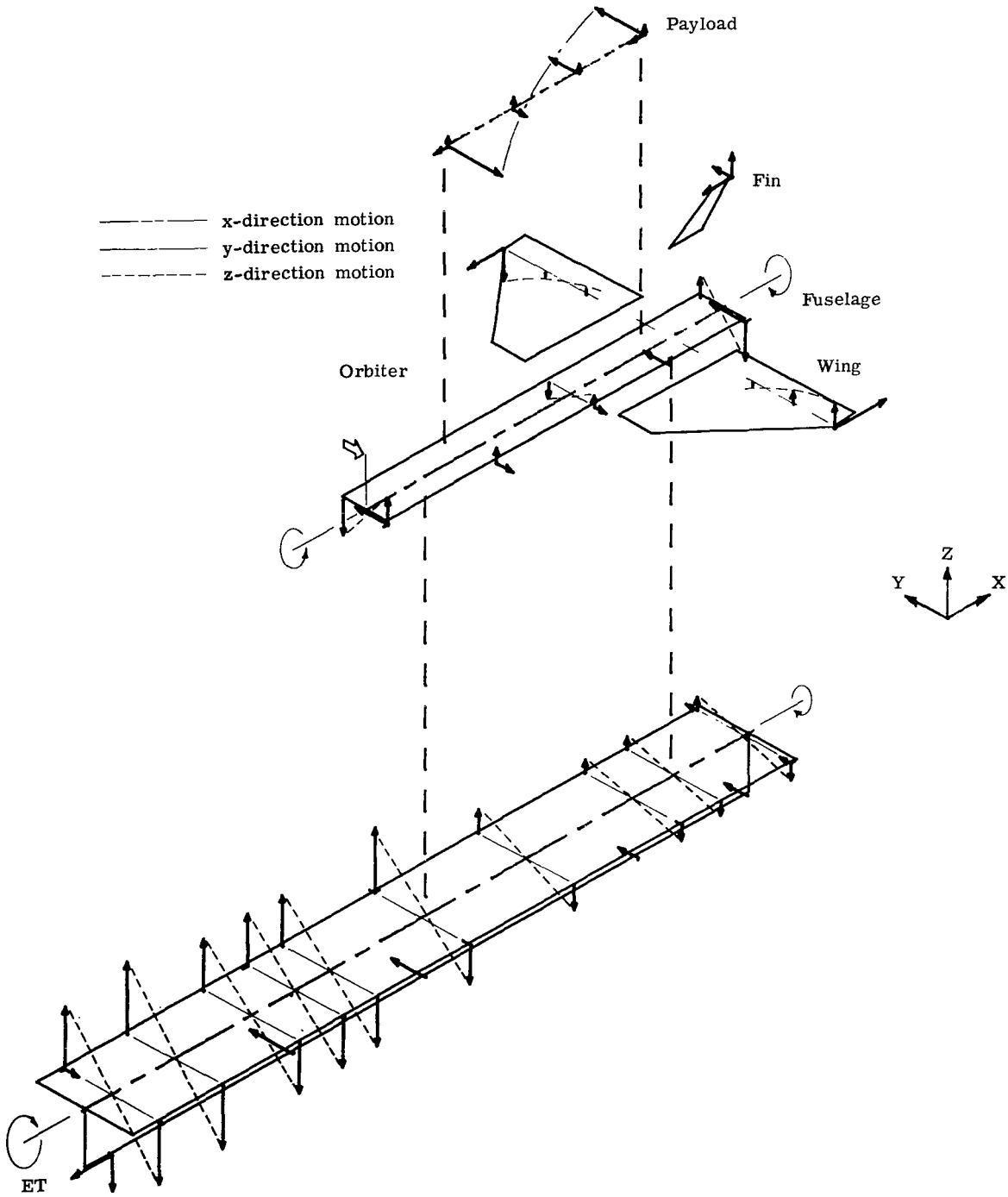

(f) 89.88 Hz, mode 15.

Figure 26.- Concluded.

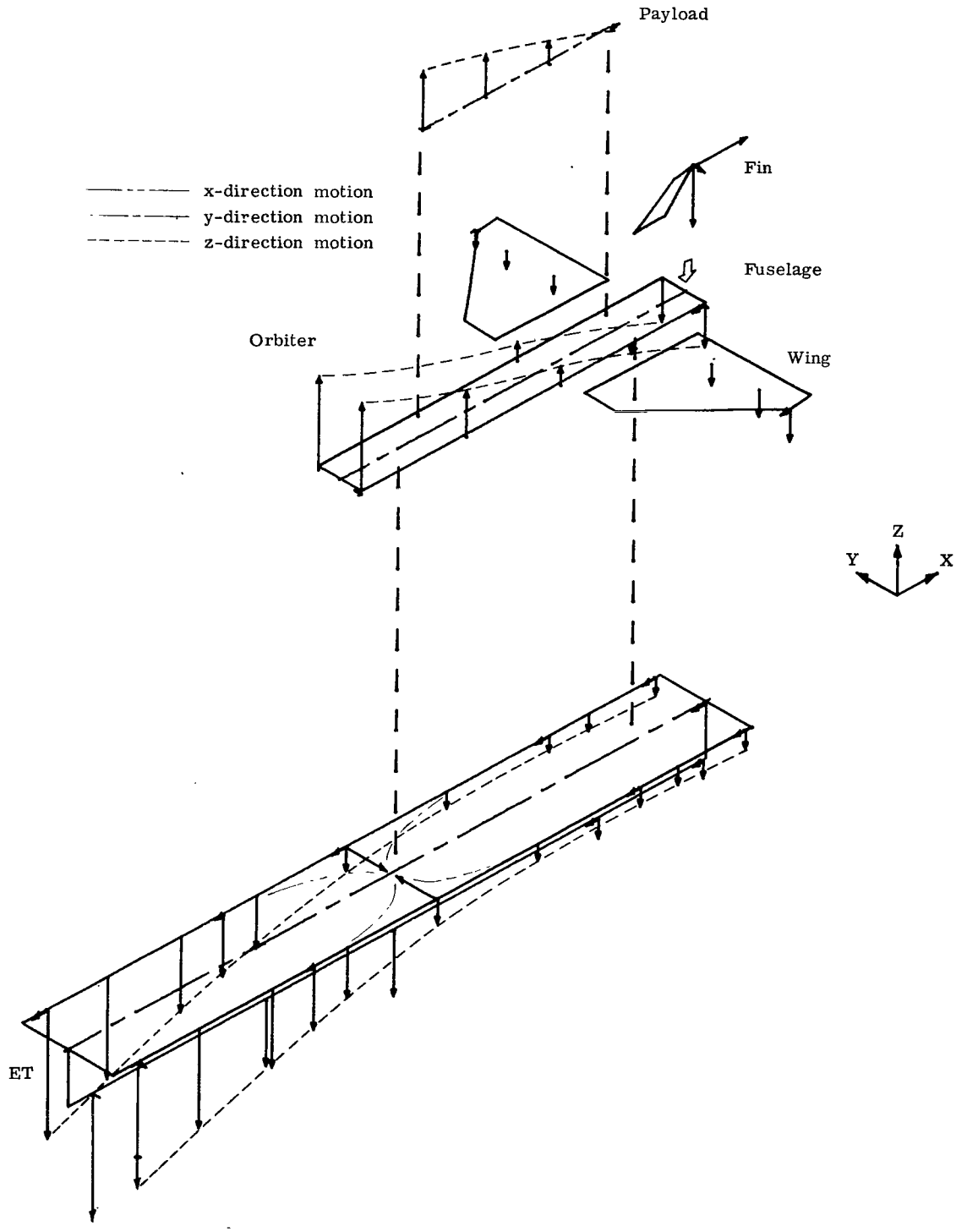

(a) 32.13 Hz, mode 1.

Figure 27.- Measured mode shapes for mated 1/8-scale shuttle model at end-burn (before ET jettison).

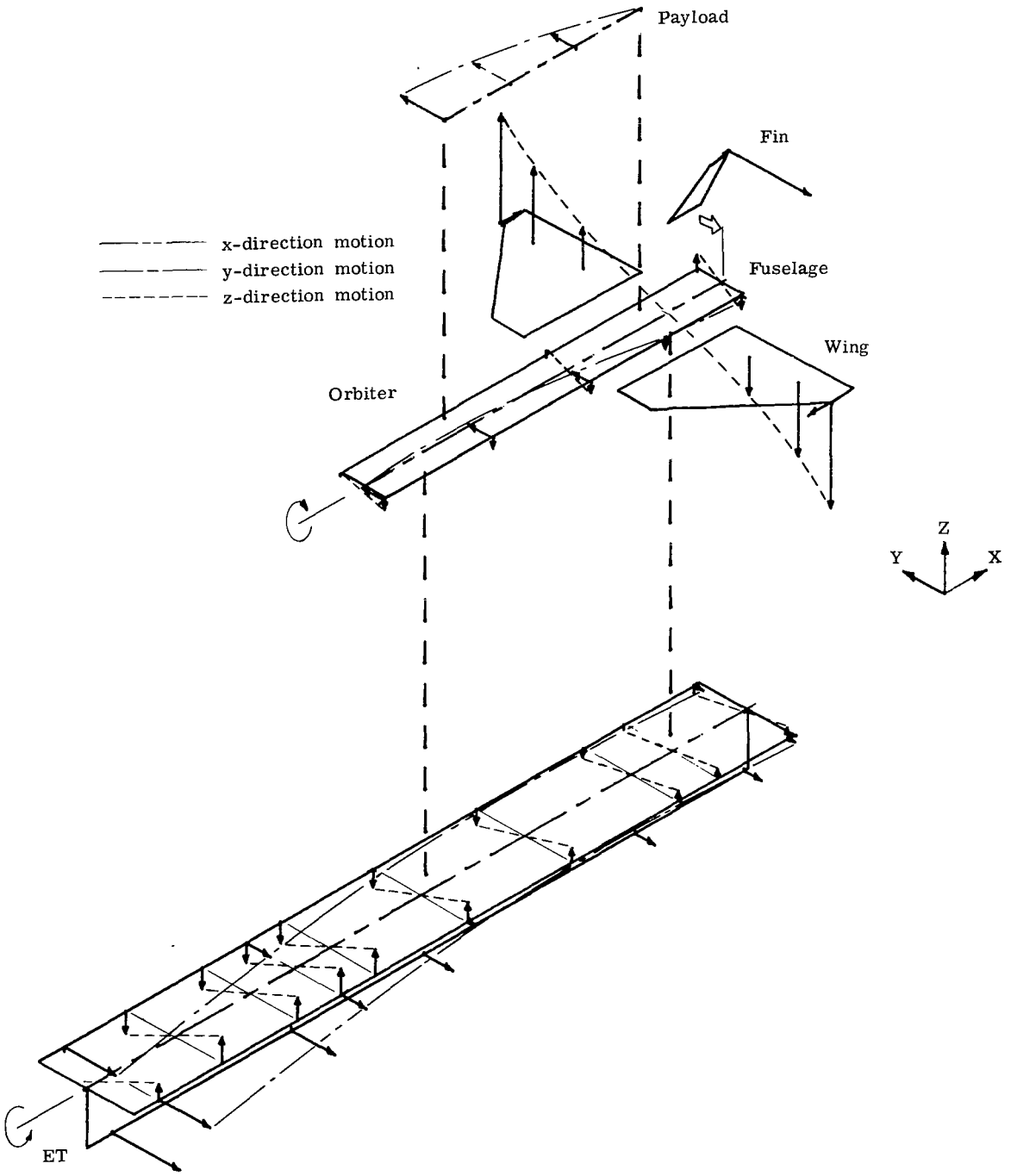

(b) 35.65 Hz, mode 2.

Figure 27.- Continued.

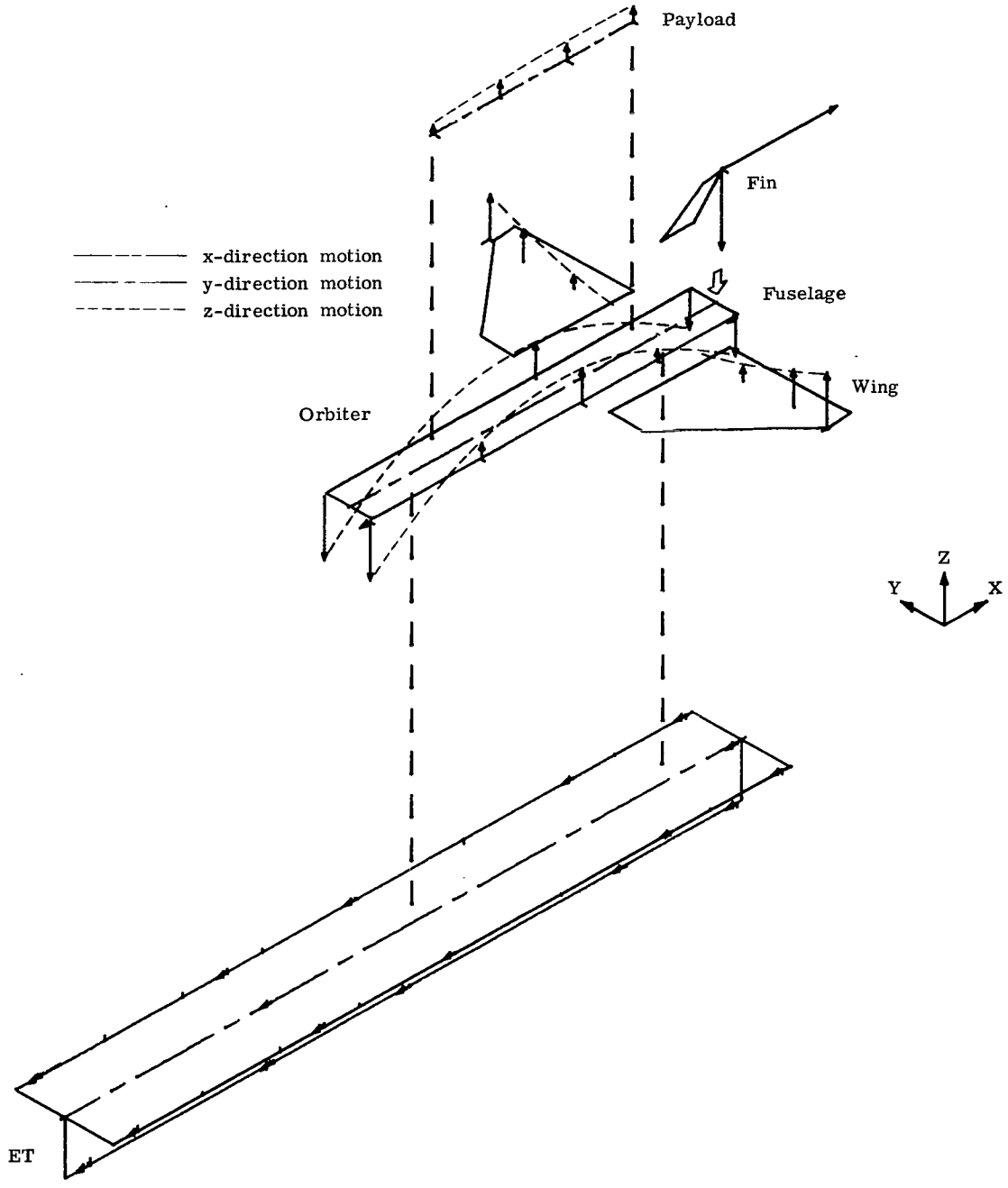

(c) 42.91 Hz, mode 4.

Figure 27.- Continued.

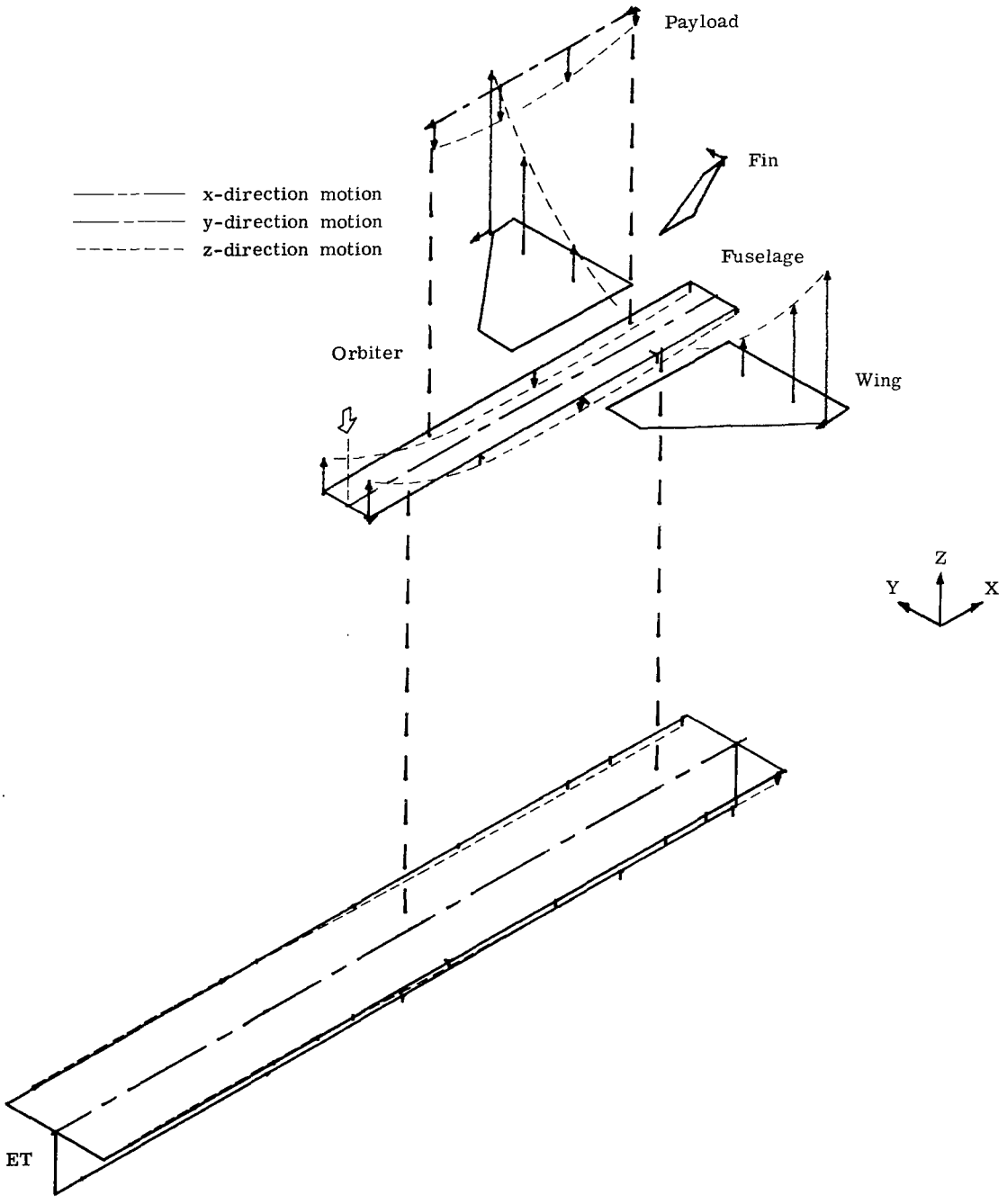

(d) 51.33 Hz, mode 6.

Figure 27.- Continued.

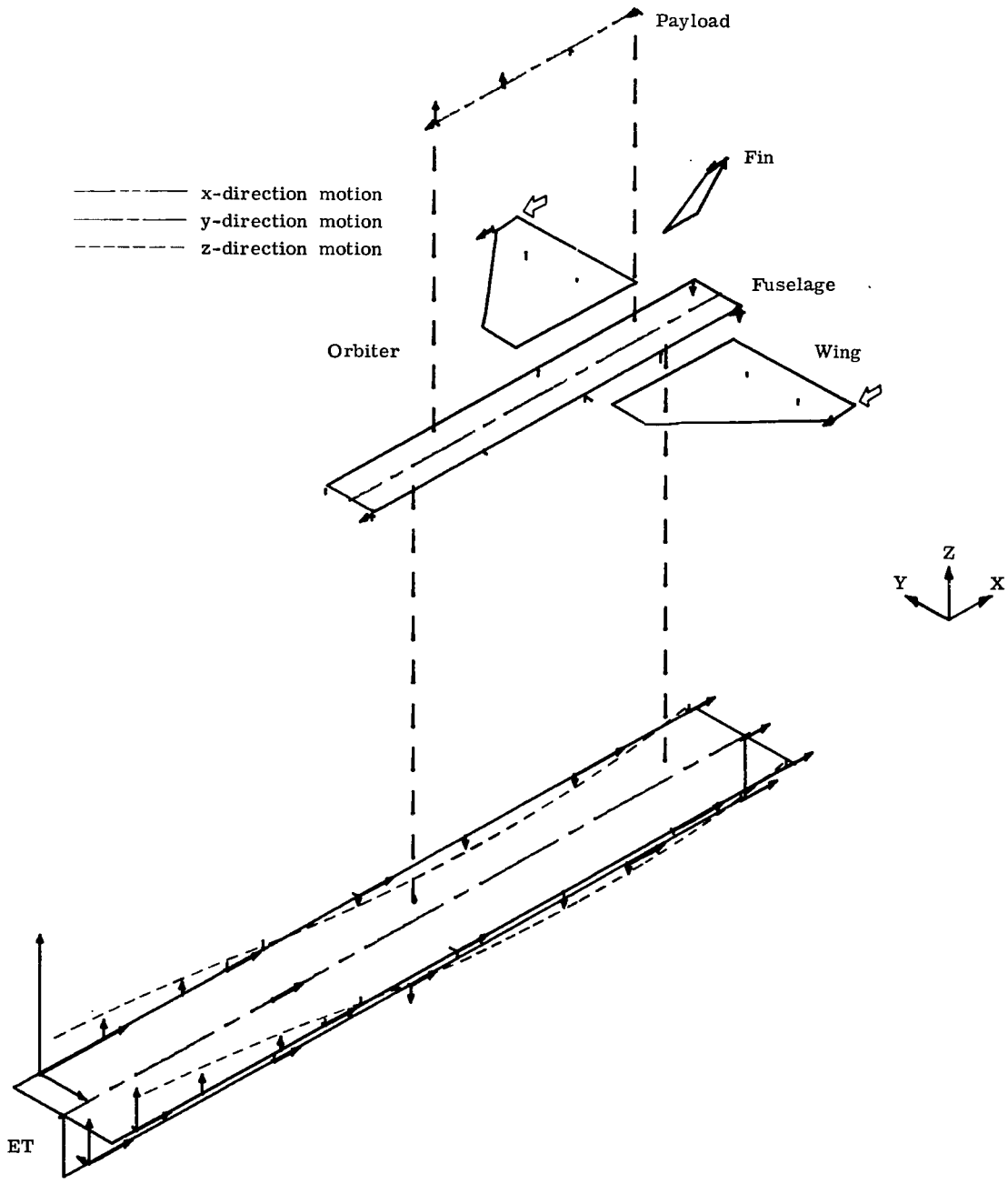

(e) 63.16 Hz, mode 11.

Figure 27.- Continued.

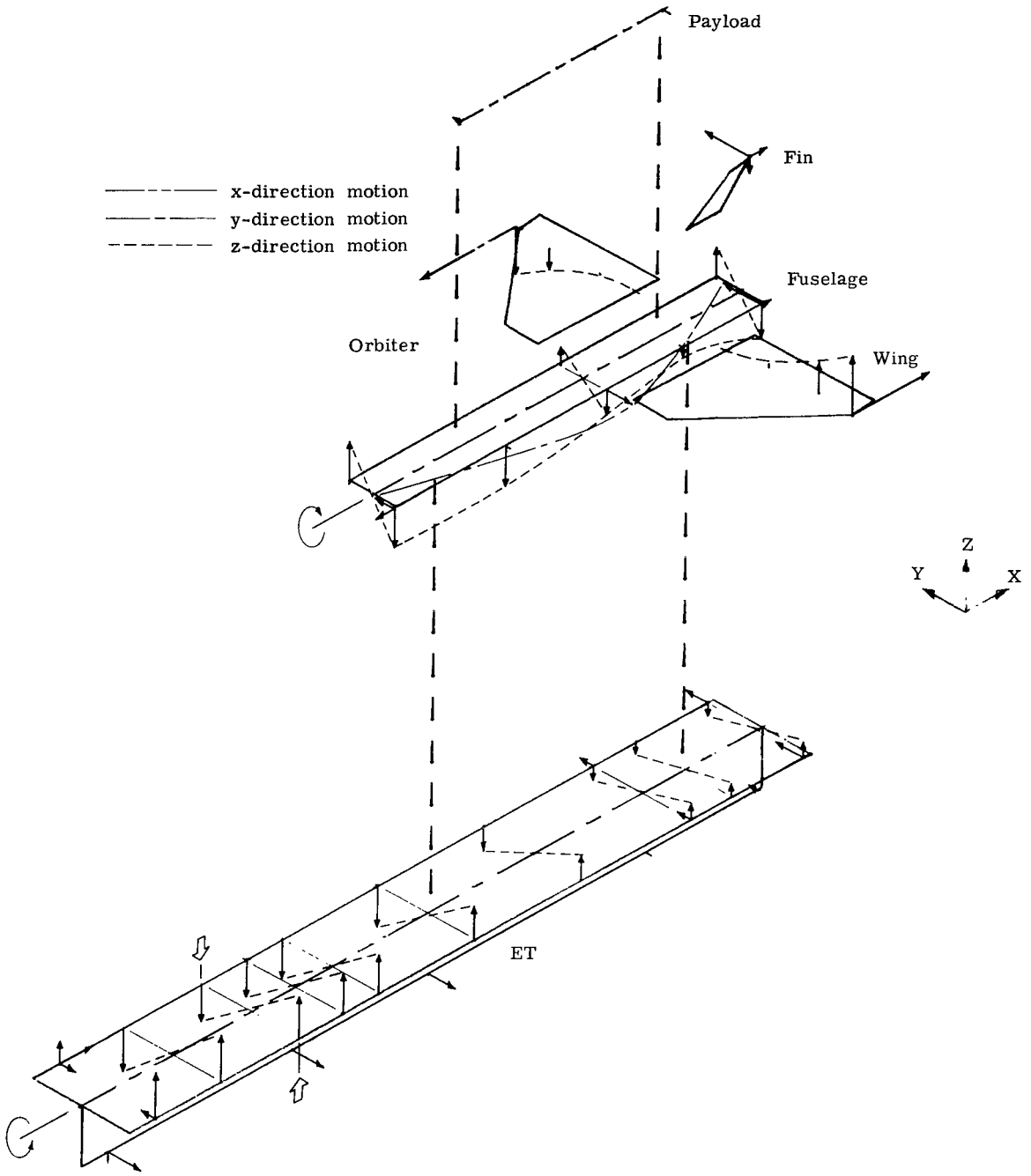

(f) 73.82 Hz, mode 12.

Figure 27.- Concluded.

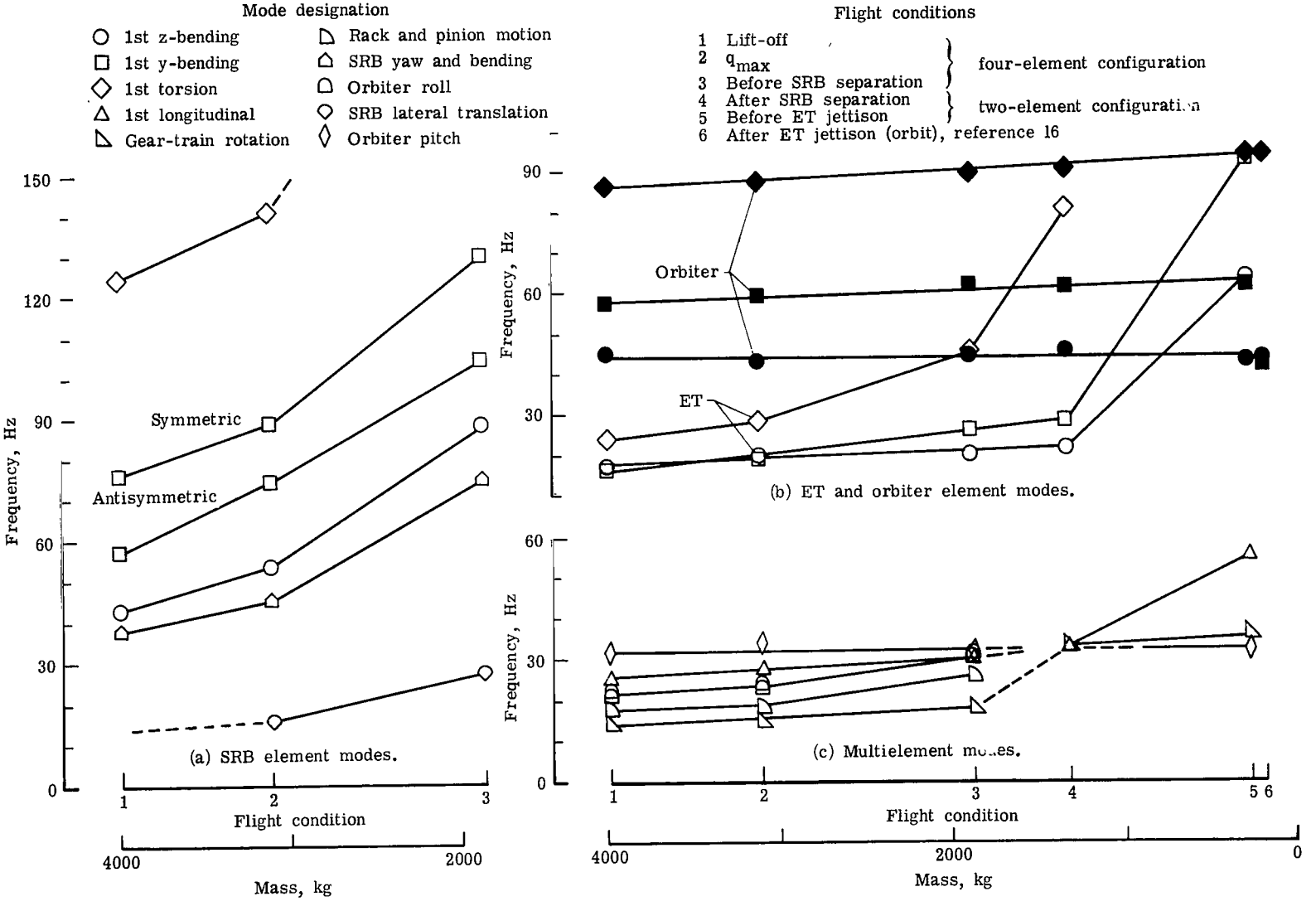

Figure 28.- Variations of resonant frequencies for several modes with flight condition of 1/8-scale shuttle model.

(a) Lift-off.

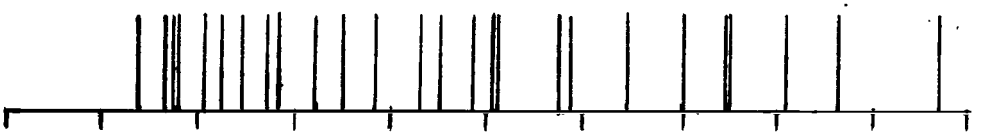

(b) After SRB separation.

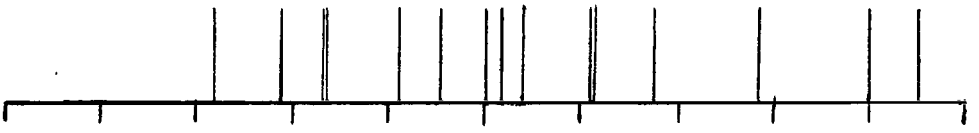

(c) Before ET jettison.

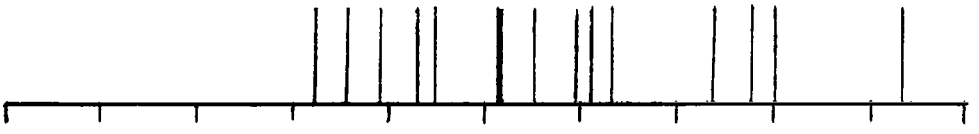

(d) After ET jettison (orbiter only), reference 16.

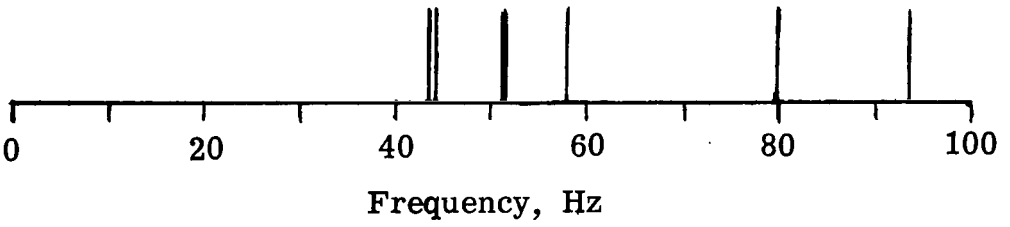

Figure 29.- Natural frequency spectrums obtained for 1/8-scale shuttle model at typical flight conditions.

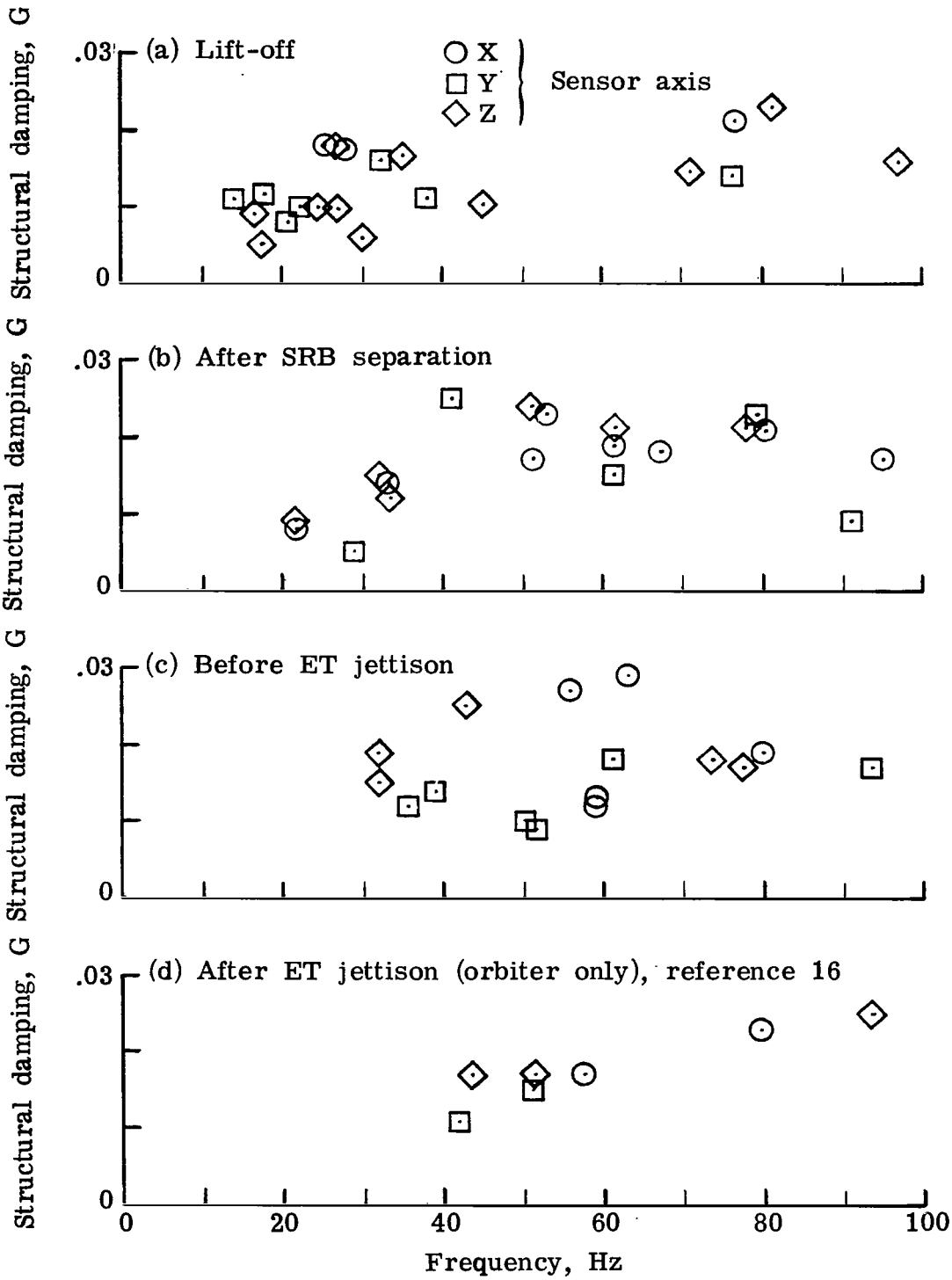

Figure 30.- Structural damping obtained for 1/8-scale shuttle model at typical flight conditions.

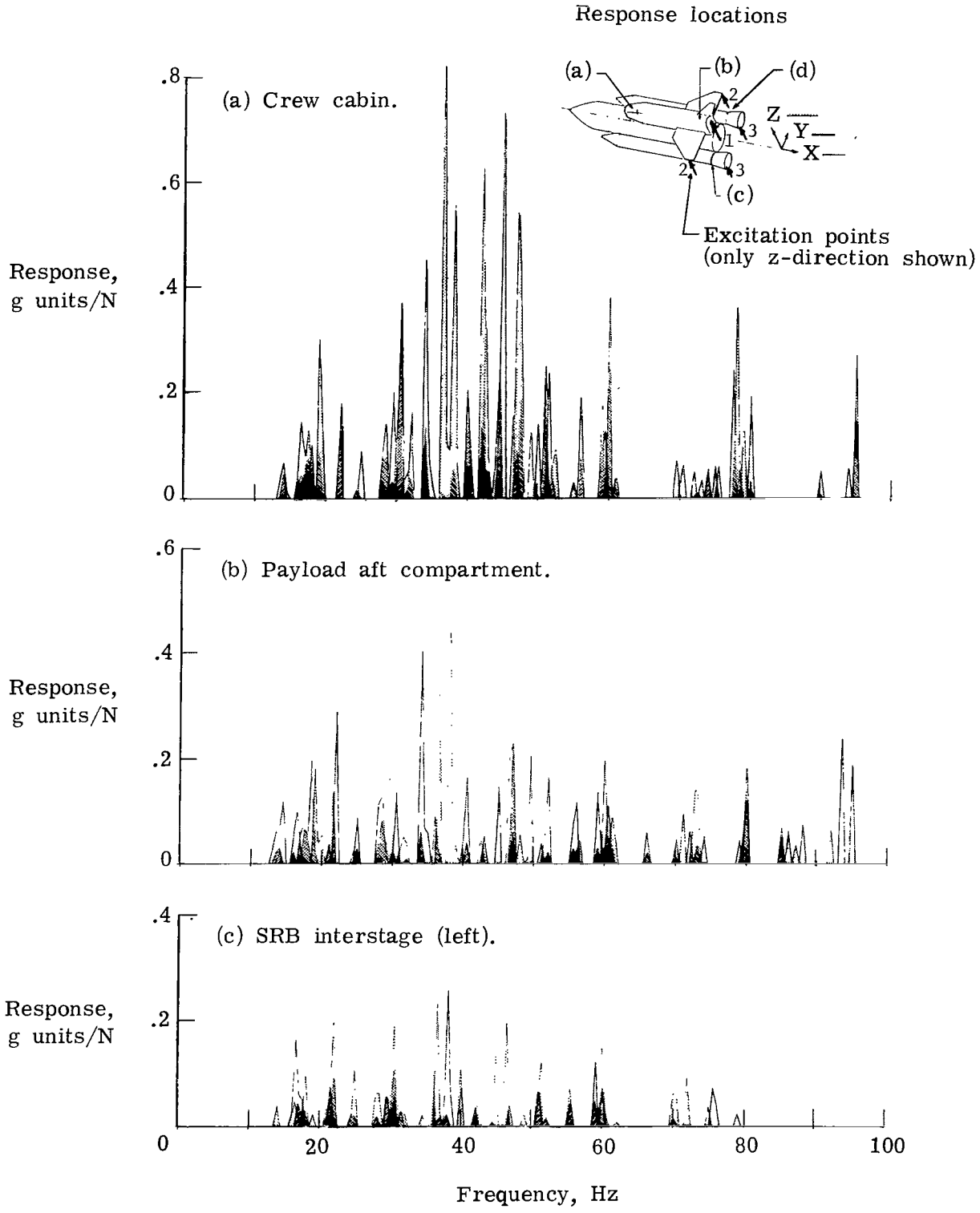

Figure 31.- Response spectrums obtained at three locations during transfer-function measurements of mated 1/8-scale shuttle model at lift-off.

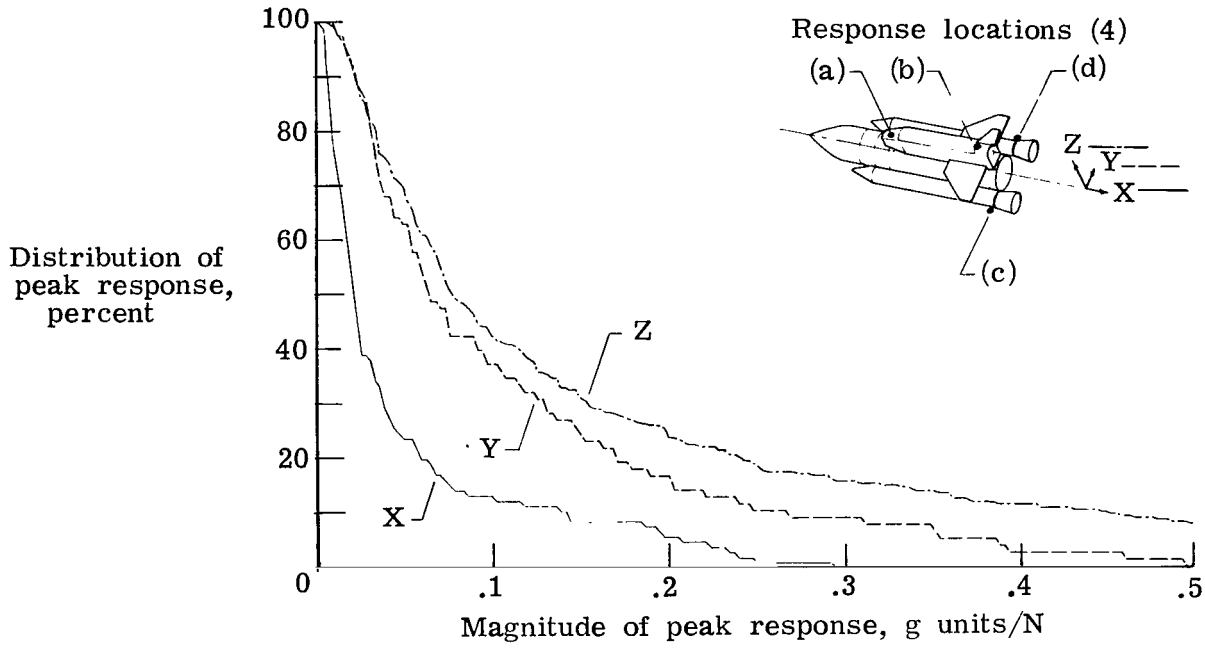

(a) Response measurements X, Y, and Z due to all excitations in x-, y-, and z-direction.

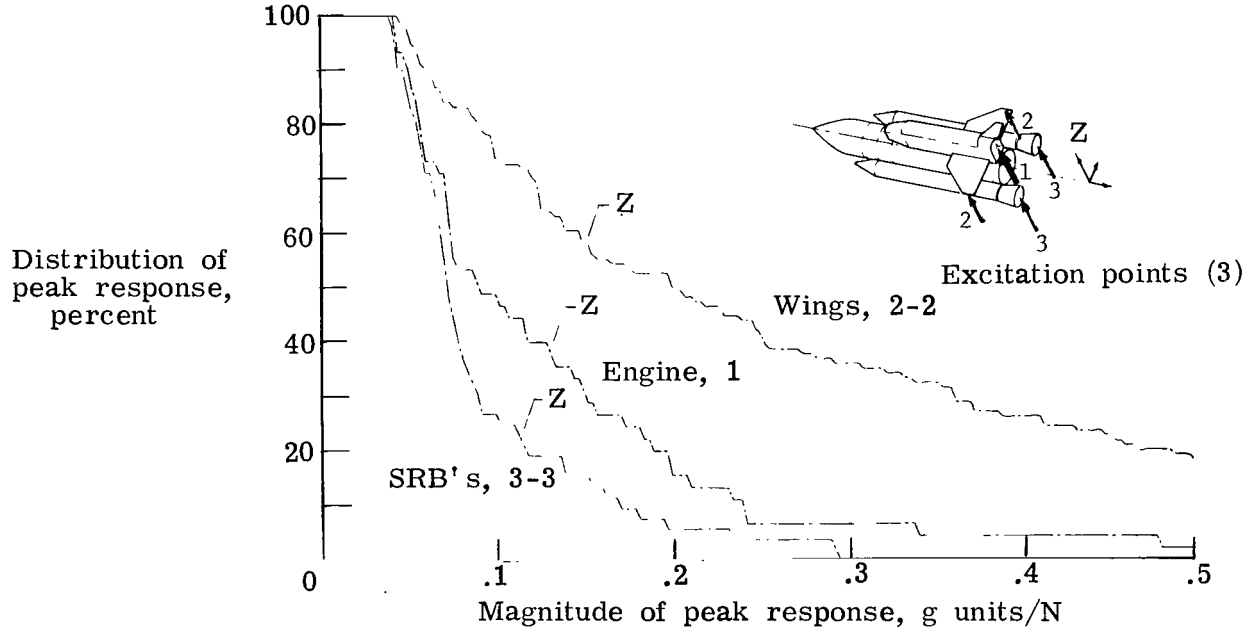

(b) Response measurements Z during excitation at three points in z-direction (1, 2-2, and 3-3).

Figure 32.- Magnitude distributions of the peak responses obtained during transfer-function measurements of mated 1/8-scale shuttle model at lift-off.

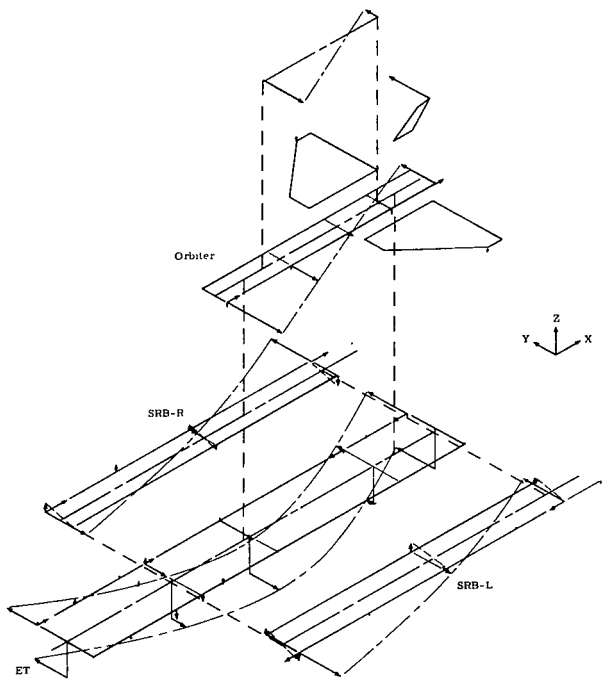

(a) 16.60 Hz, mode 2.

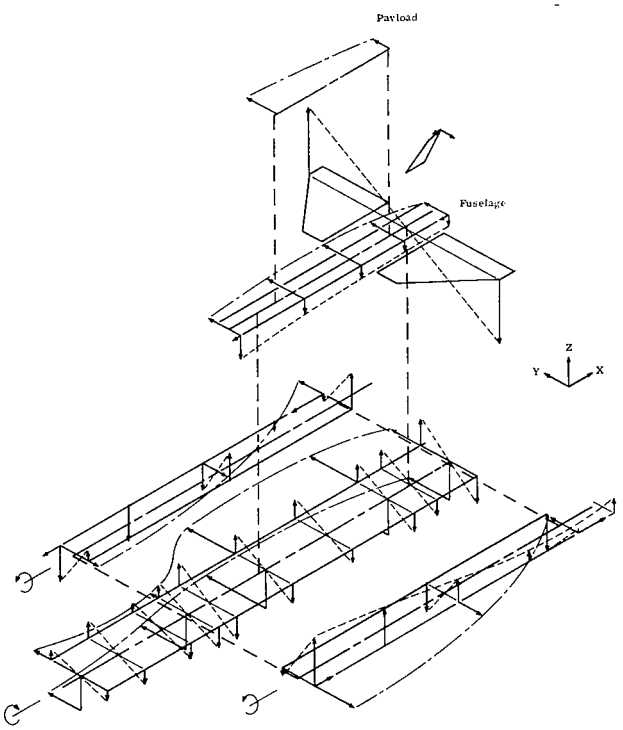

(b) 20.64 Hz, mode 5.

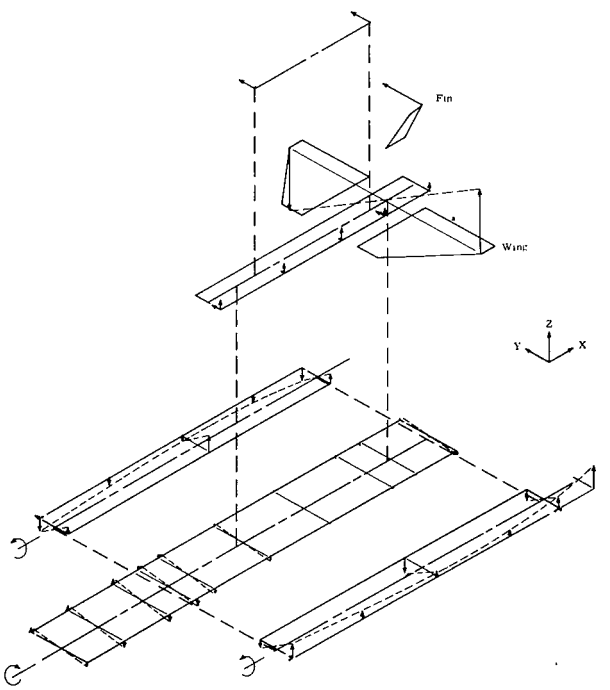

(c) 22.25 Hz, mode 6.

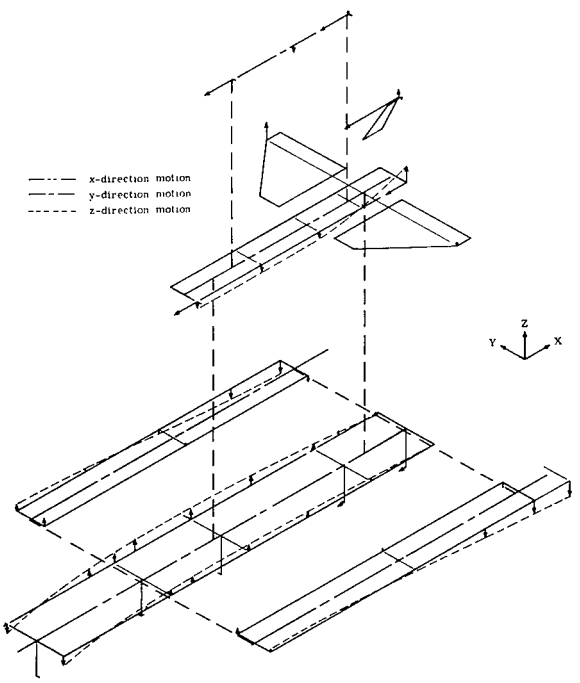

(d) 28.13 Hz, mode 9.

Figure 33.- Supplementary mode shapes for 1/8-scale shuttle model at lift-off.

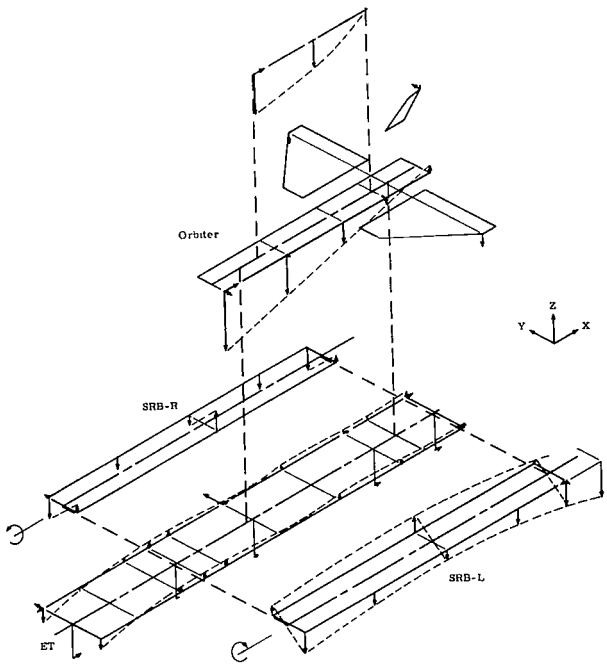

(e) 32.27 Hz, mode 10.

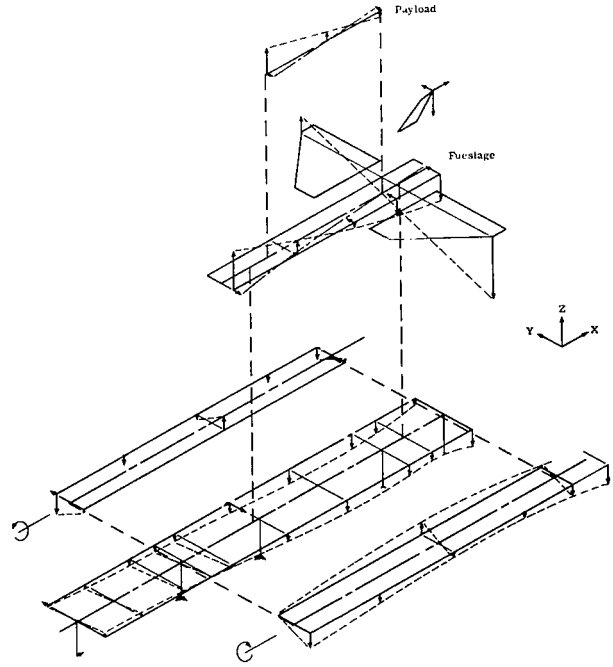

(f) 35.25 Hz, mode 11.

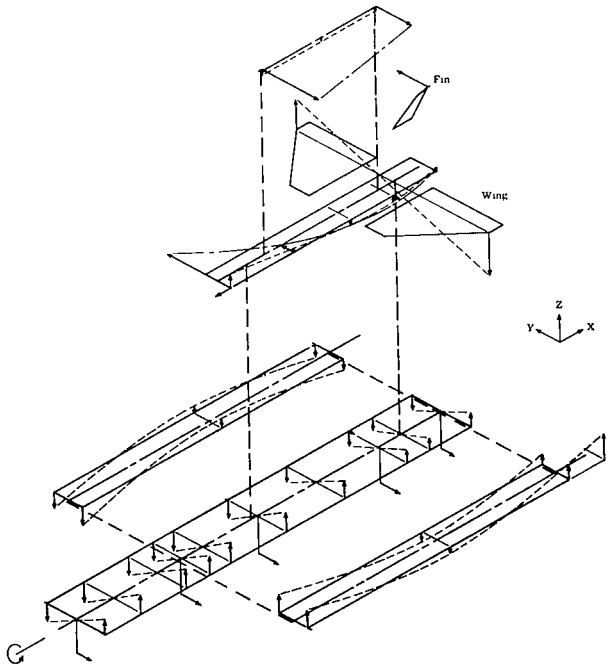

(g) 43.29 Hz, mode 13.

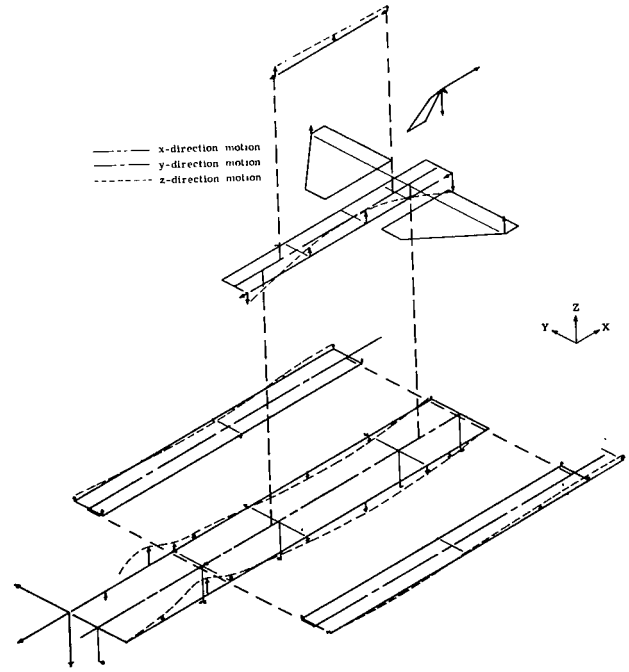

(h) 45.15 Hz, mode 14.

Figure 33.- Continued.

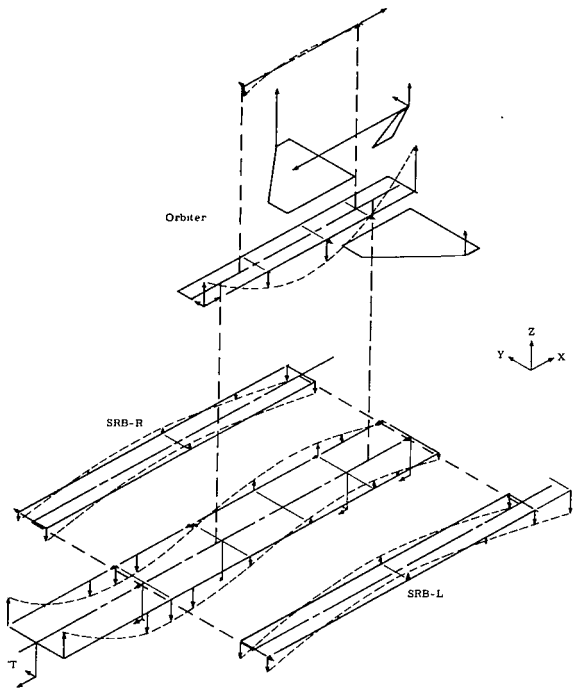

(i) 48.50 Hz, mode 15.

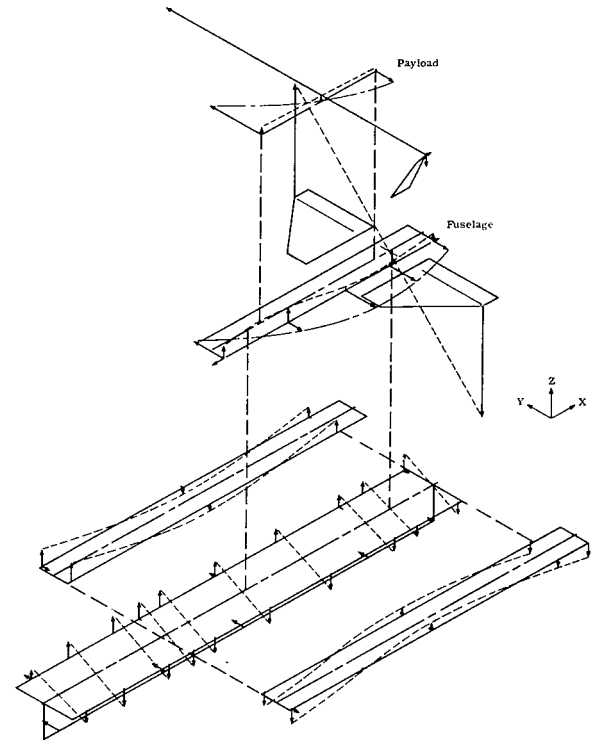

(j) 51.39 Hz, mode 16.

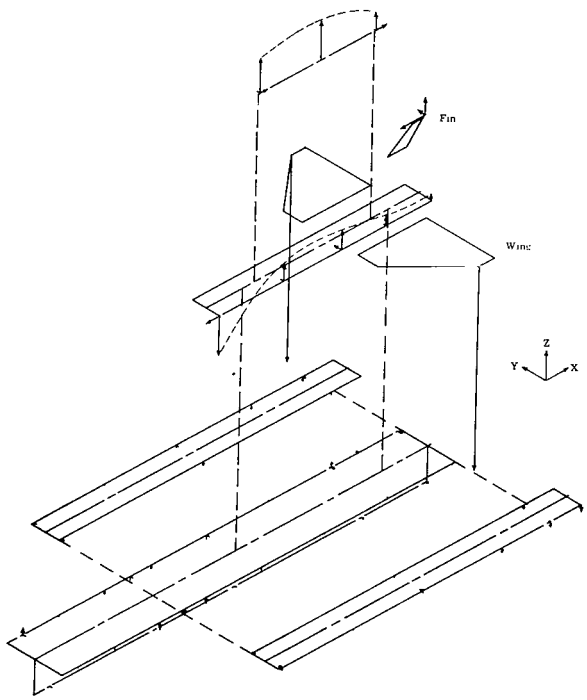

(k) 51.66 Hz, mode 17.

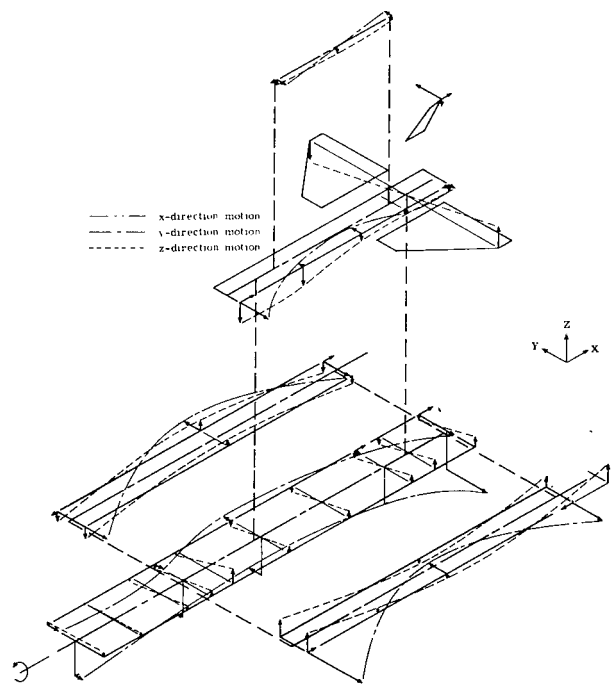

(l) 57.64 Hz, mode 18.

Figure 33.- Continued.

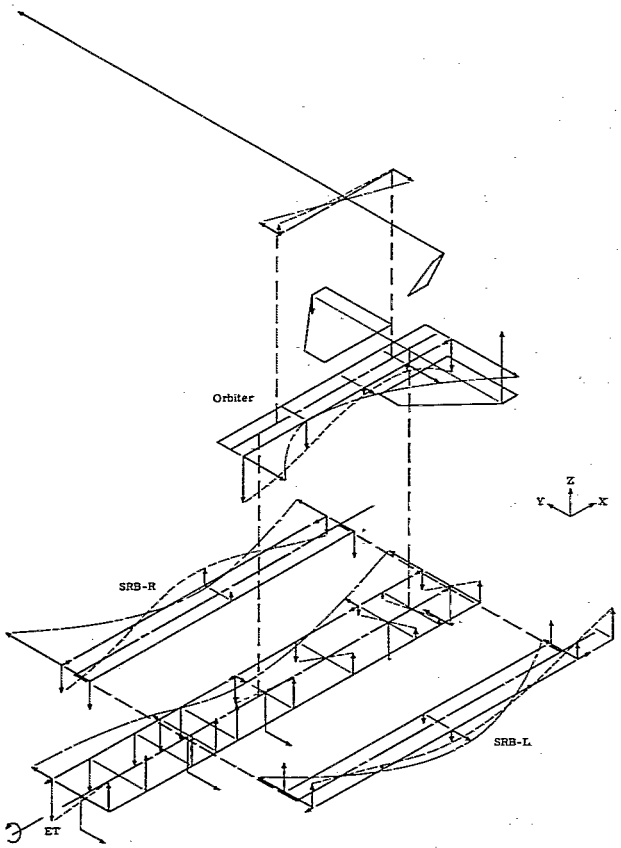

(m) 58.65 Hz, mode 19.

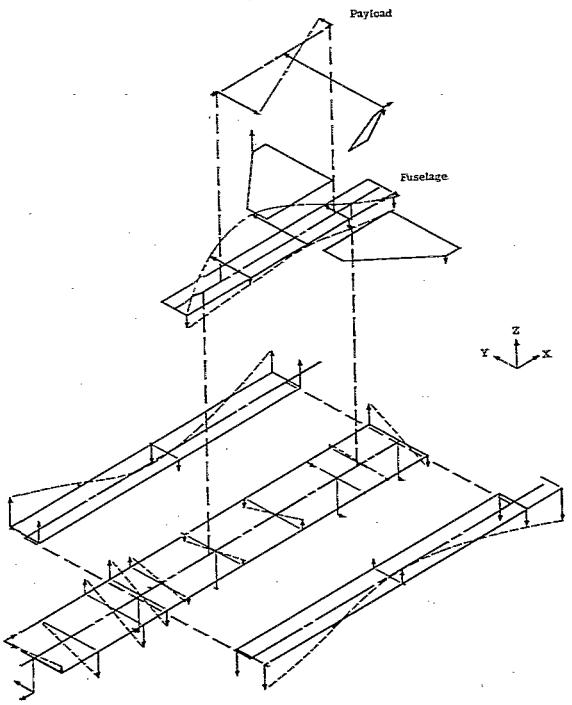

(n) 64.14 Hz, mode 20.

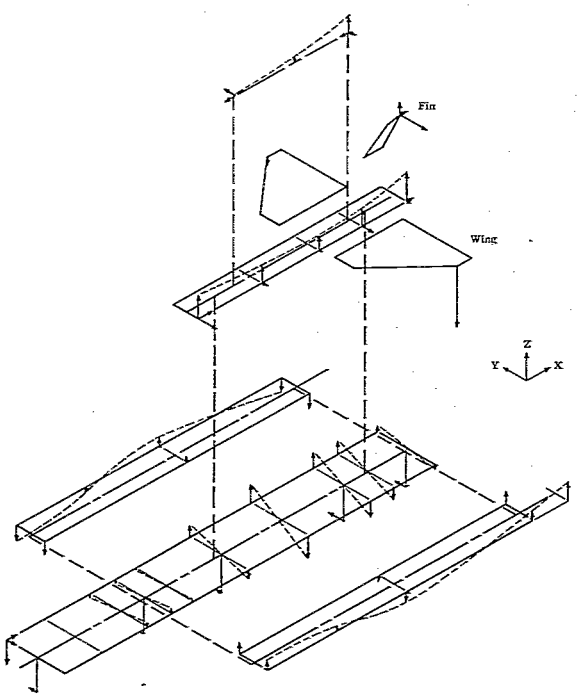

(o) 75.02 Hz, mode 22.

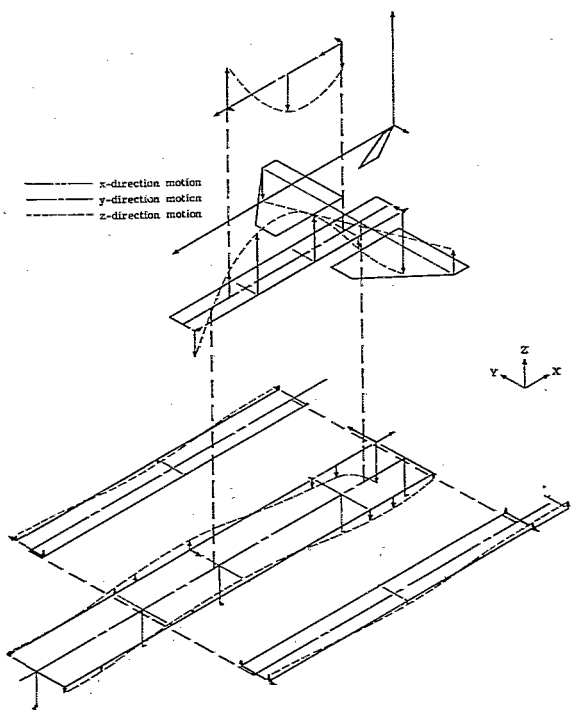

(p) 81.23 Hz, mode 24.

Figure 33.- Continued.

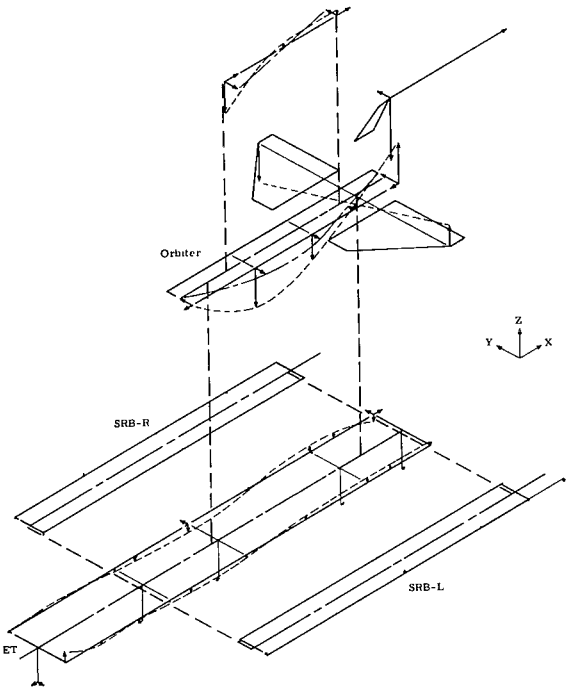

(q) 86.58 Hz, mode 25.

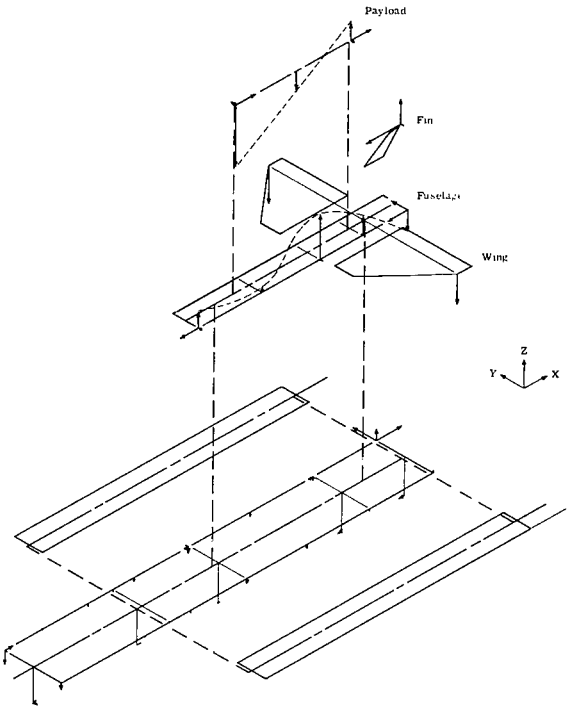

(r) 96.99 Hz, mode 26.

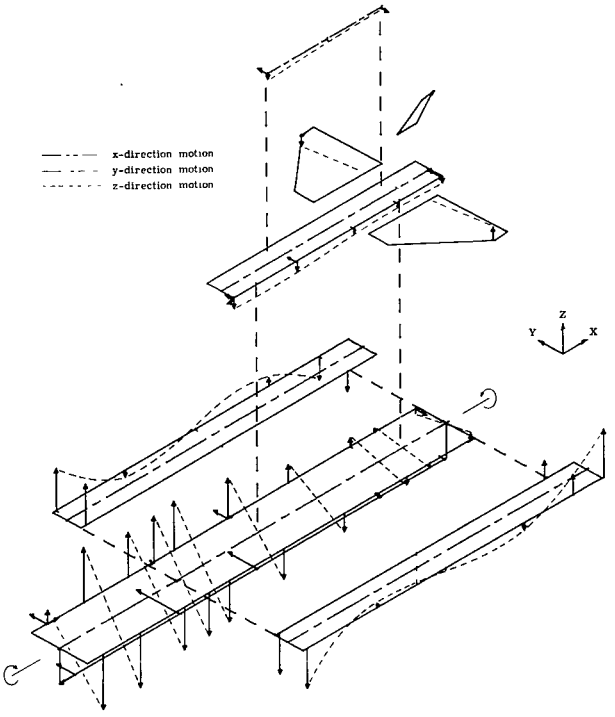

(s) 117.50 Hz, mode 27.

Figure 33.- Concluded.

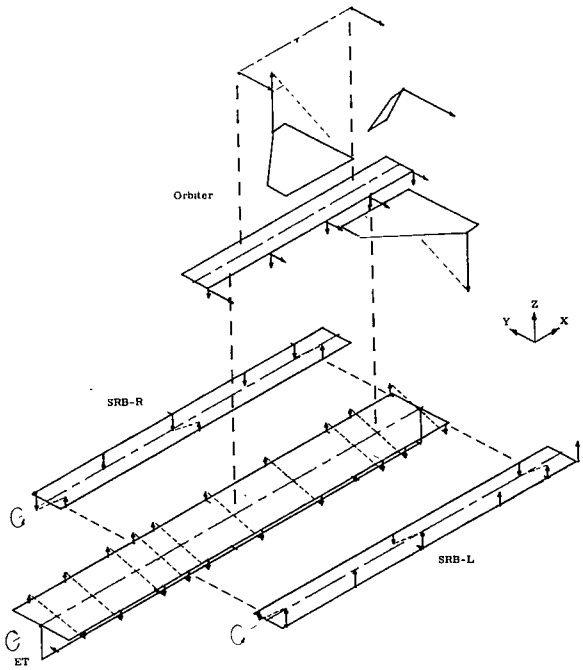

(a) 14.72 Hz, mode 1.

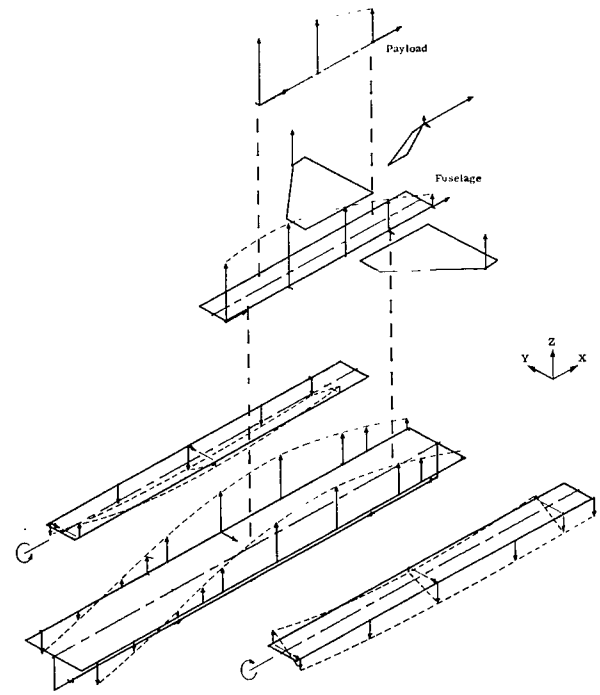

(b) 18.68 Hz, mode 3.

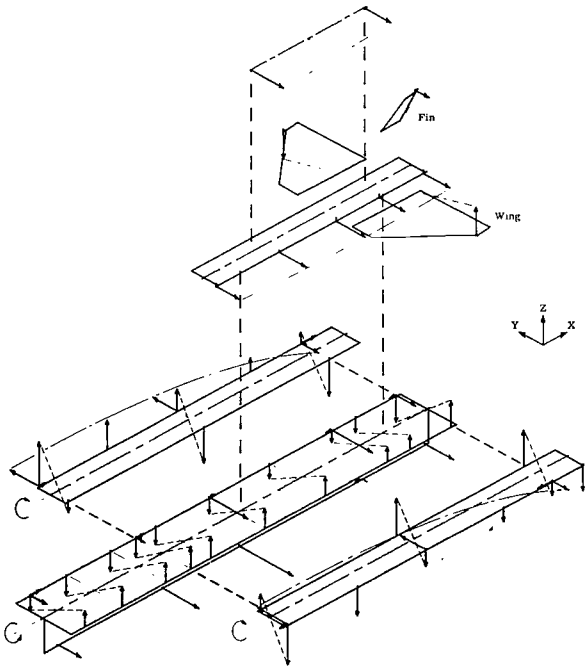

(c) 23.08 Hz, mode 6.

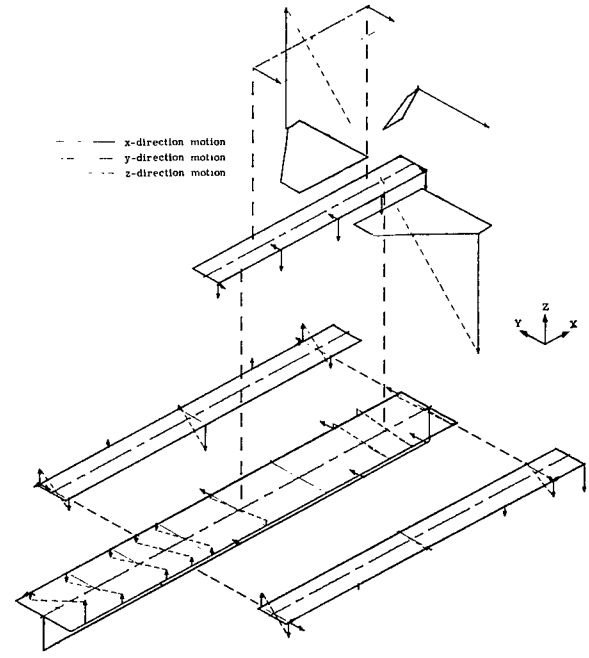

(d) 24.16 Hz, mode 7.

Figure 34.- Supplementary mode shapes for 1/8-scale shuttle model at mid-boost (q_{max}).

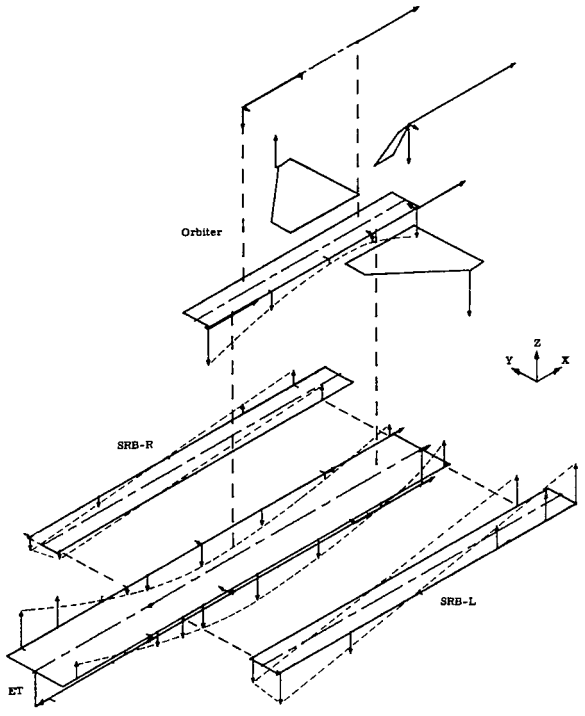

(e) 29.93 Hz, mode 10.

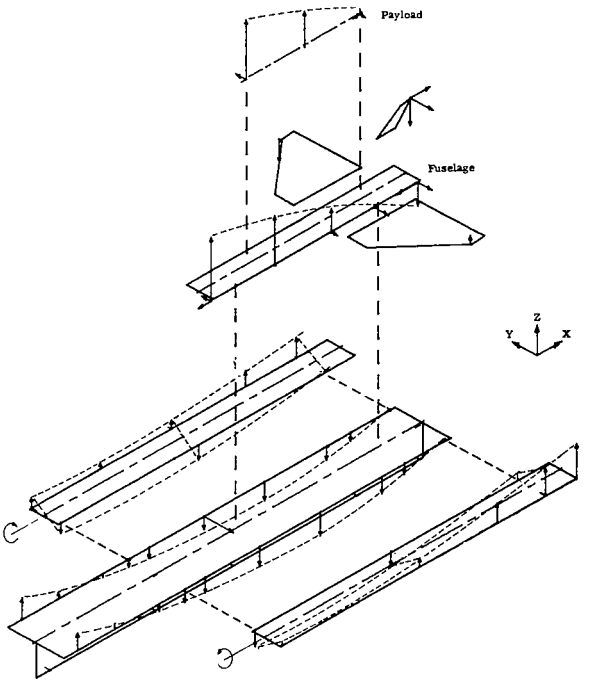

(f) 33.80 Hz, mode 11.

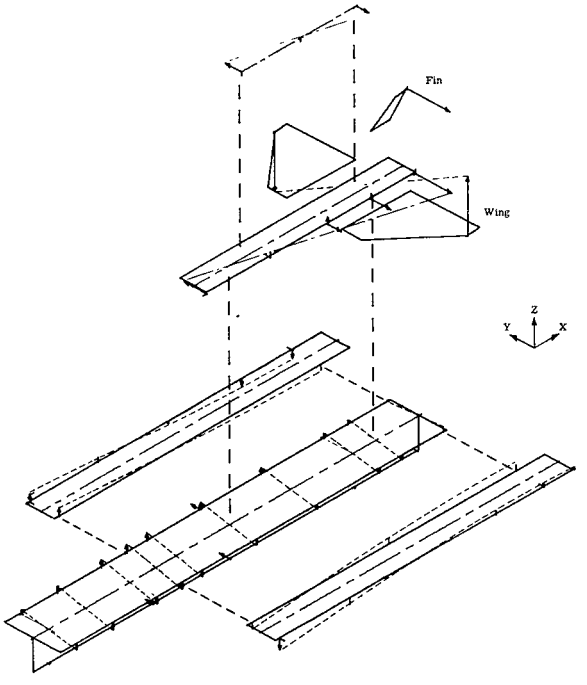

(g) 35.52 Hz, mode 12.

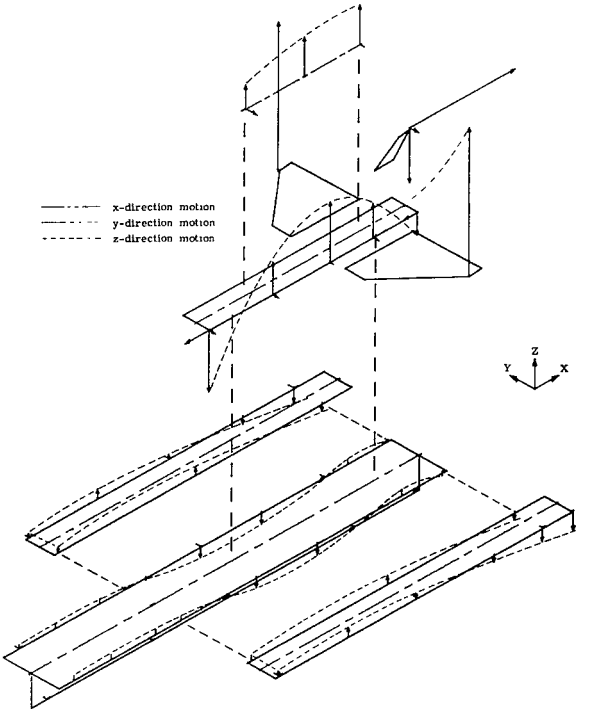

(h) 41.98 Hz, mode 13.

Figure 34.- Continued.

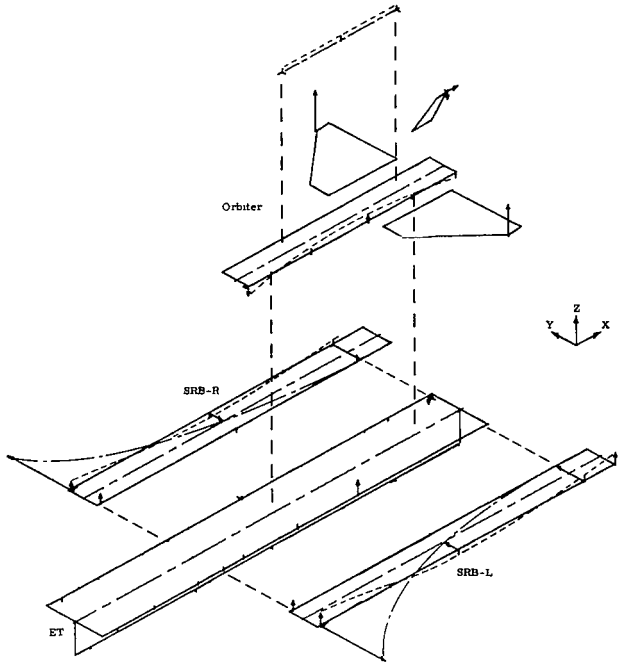

(i) 45.49 Hz, mode 14.

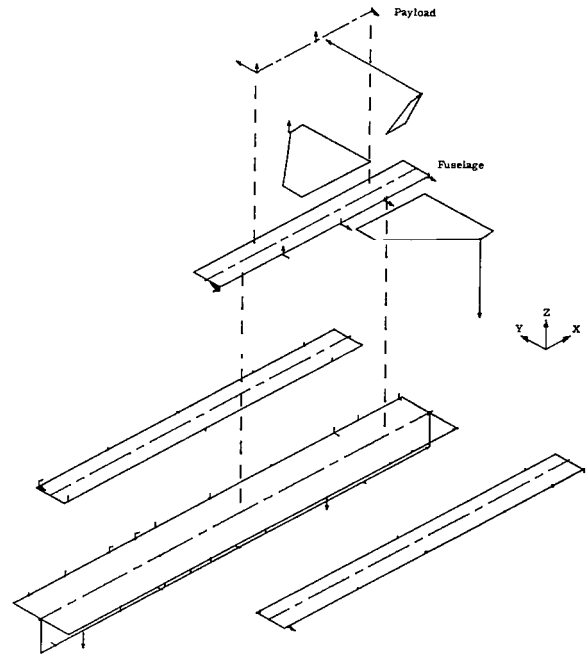

(j) 51.49 Hz, mode 15.

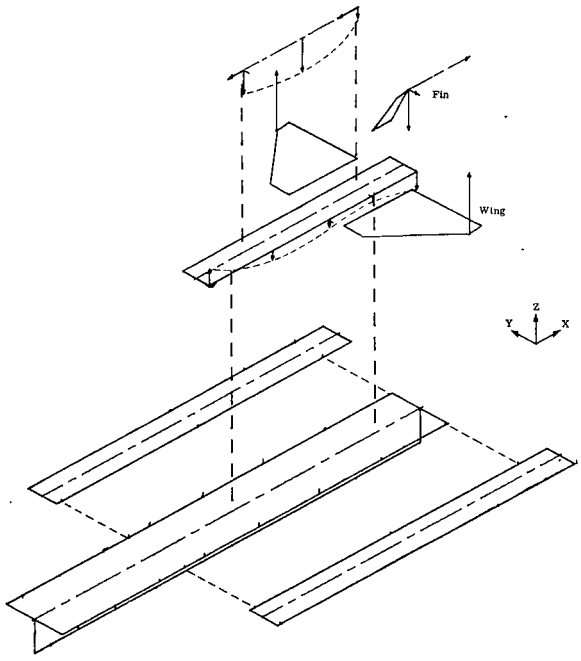

(k) 52.65 Hz, mode 16.

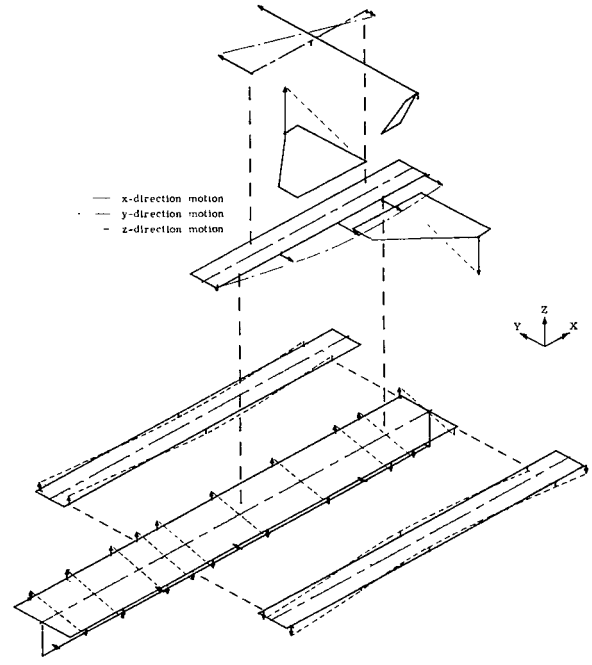

(l) 53.84 Hz, mode 17.

Figure 34.- Continued.

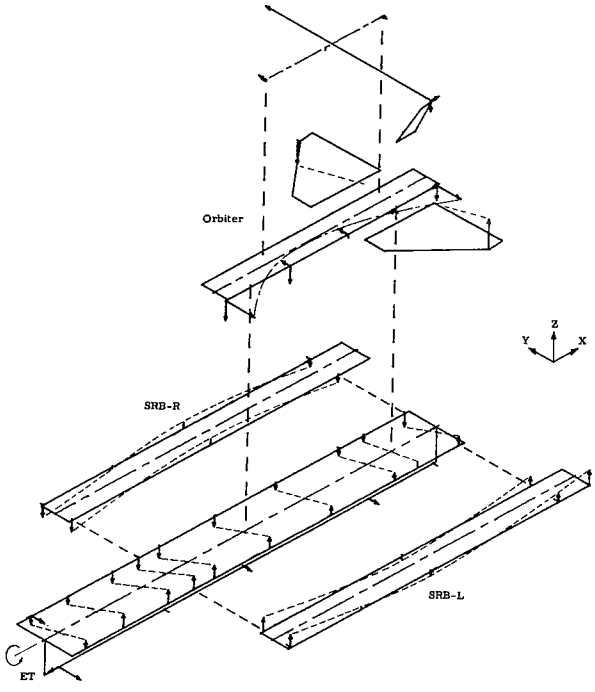

(m) 59.12 Hz, mode 18.

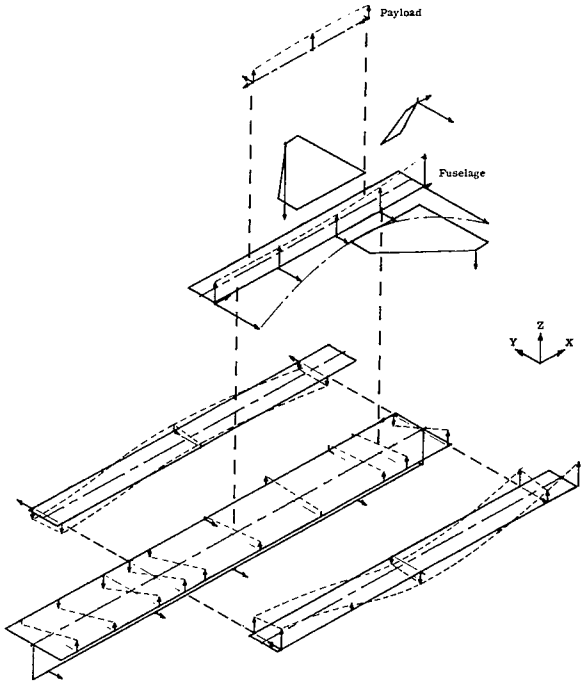

(n) 74.71 Hz, mode 19.

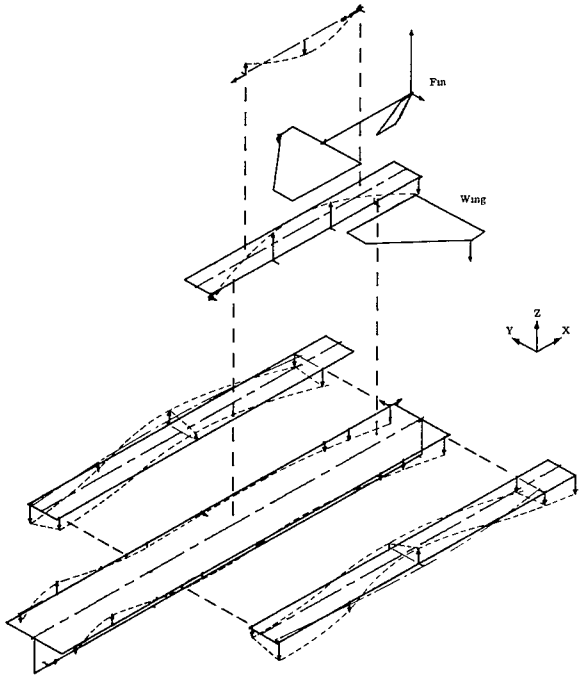

(o) 78.68 Hz, mode 20.

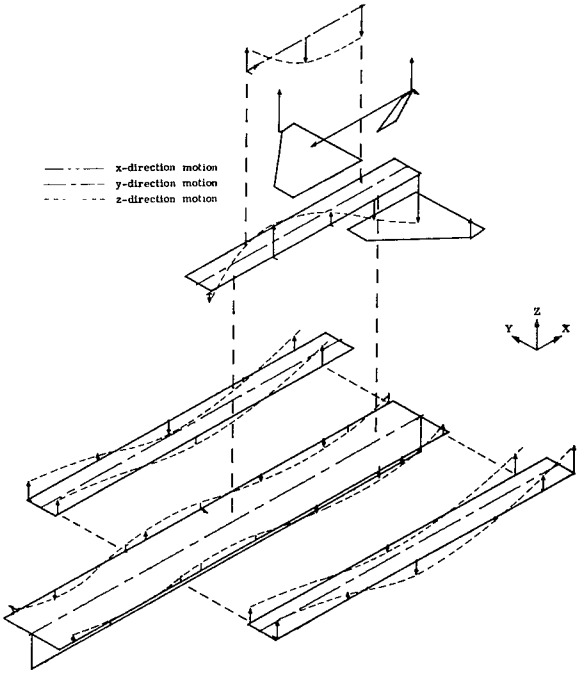

(p) 83.30 Hz, mode 21.

Figure 34.- Continued.

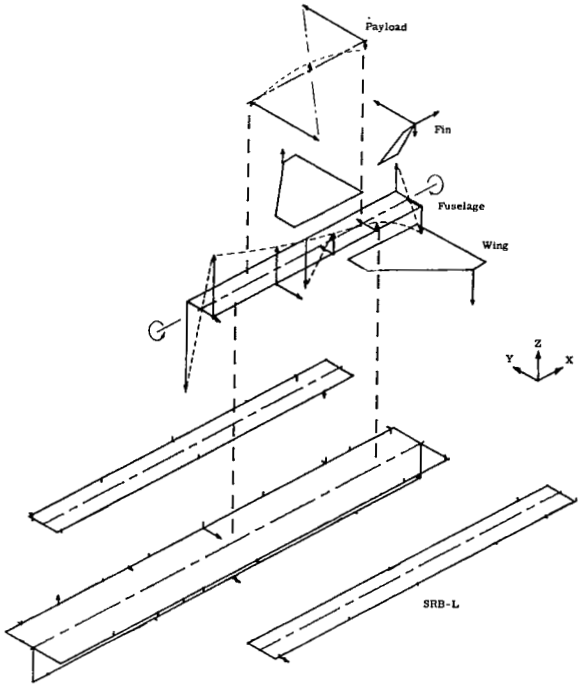

(q) 87.40 Hz, mode 22.

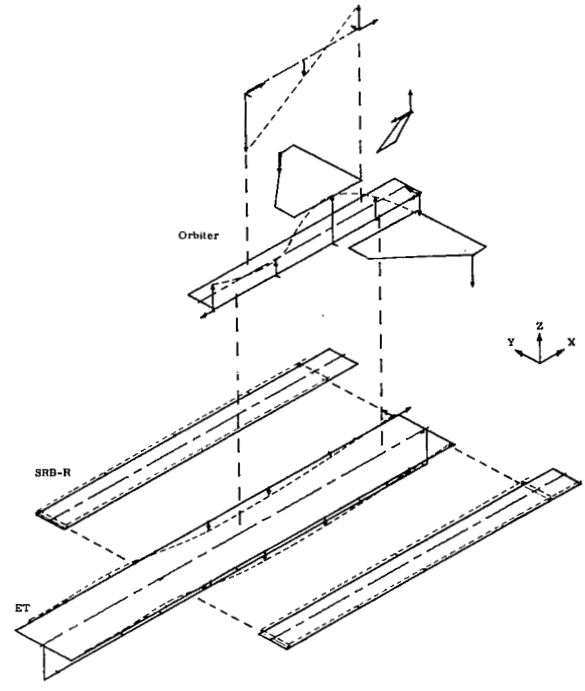

(r) 96.12 Hz, mode 24.

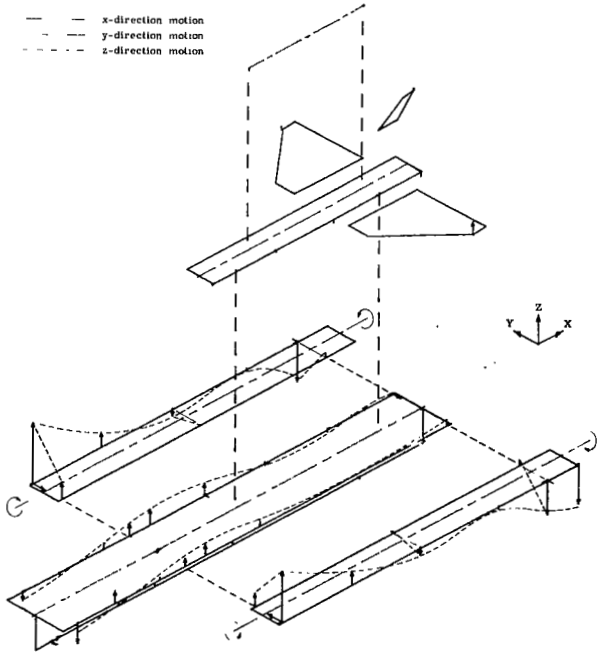

(s) 140.88 Hz.

Figure 34.- Concluded.

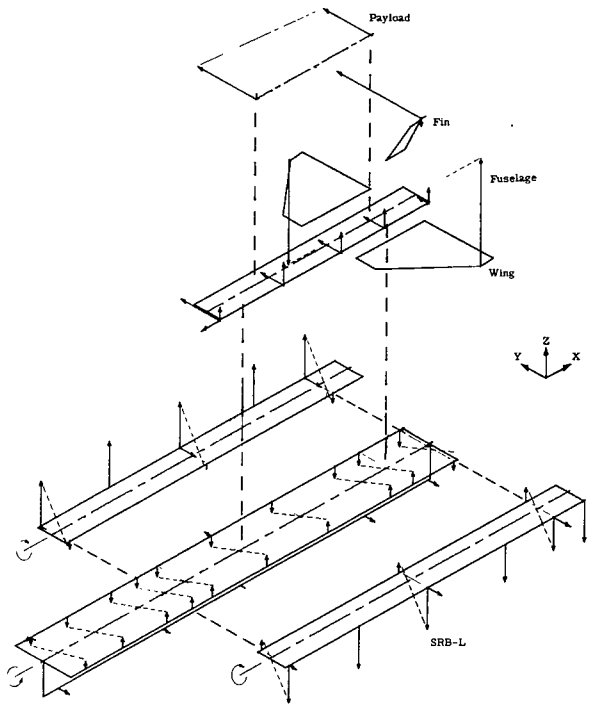

(a) 18.39 Hz, mode 1.

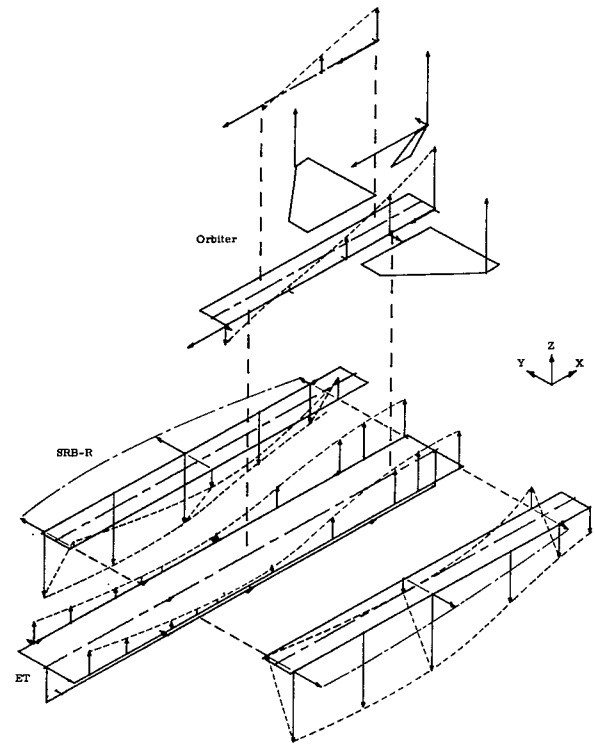

(b) 26.23 Hz, mode 3.

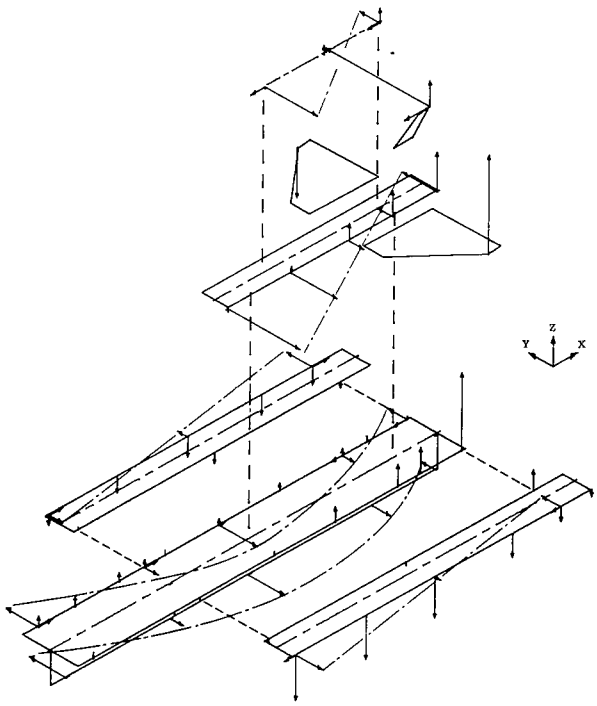

(c) 26.27 Hz, mode 4.

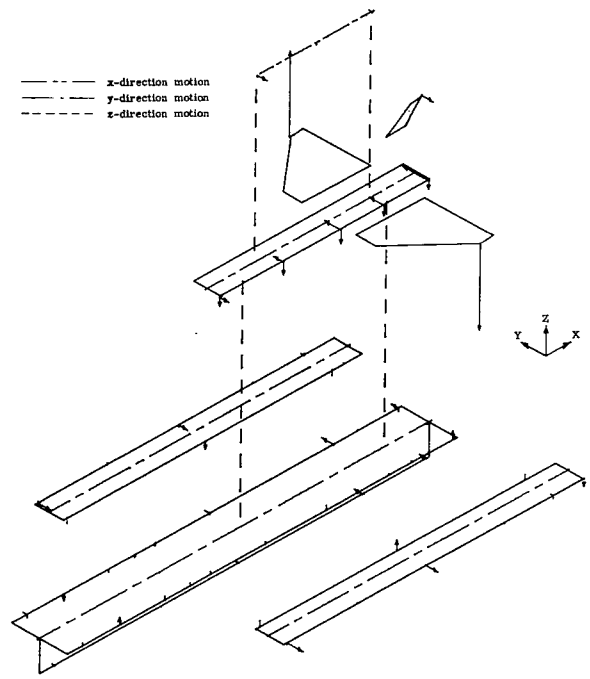

(d) 30.13 Hz, mode 7.

Figure 35.- Supplementary mode shapes for 1/8-scale shuttle model at end-boost (before SRB separation).

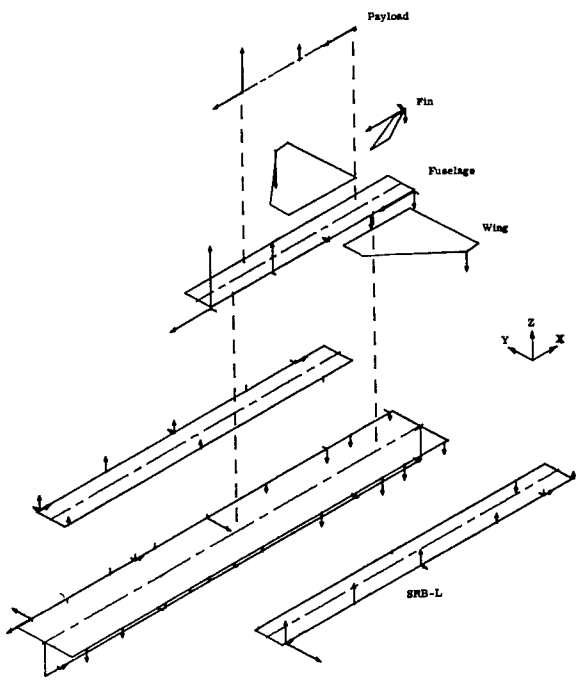

(e) 32.42 Hz, mode 9.

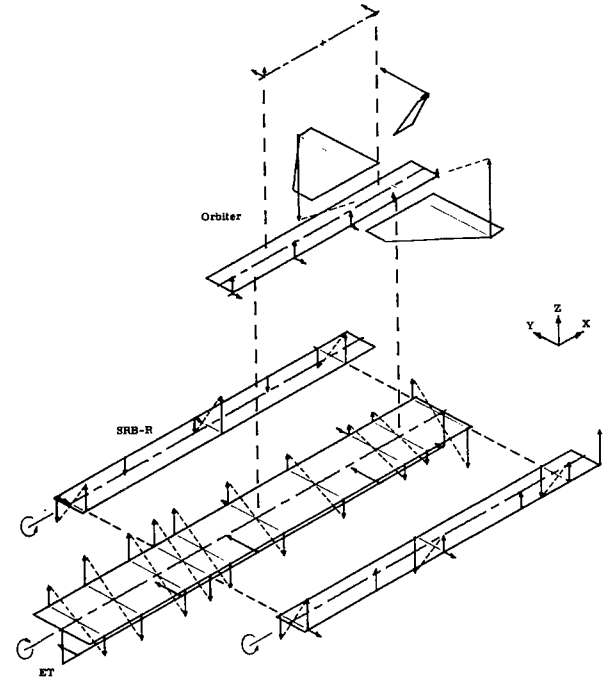

(f) 32.50 Hz, mode 10.

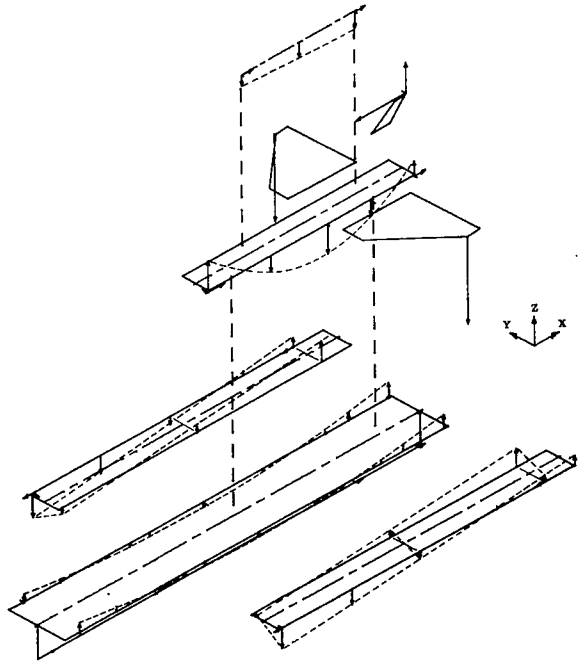

(g) 44.50 Hz, mode 11.

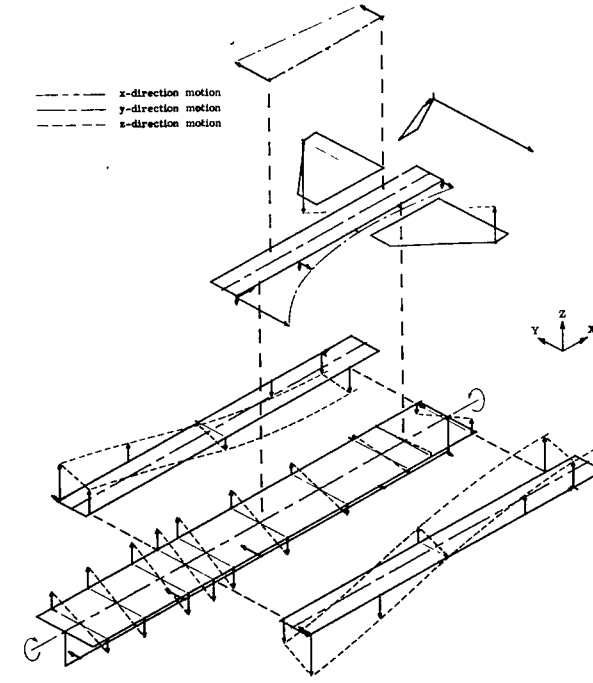

(h) 45.33 Hz, mode 12.

Figure 35.- Continued.

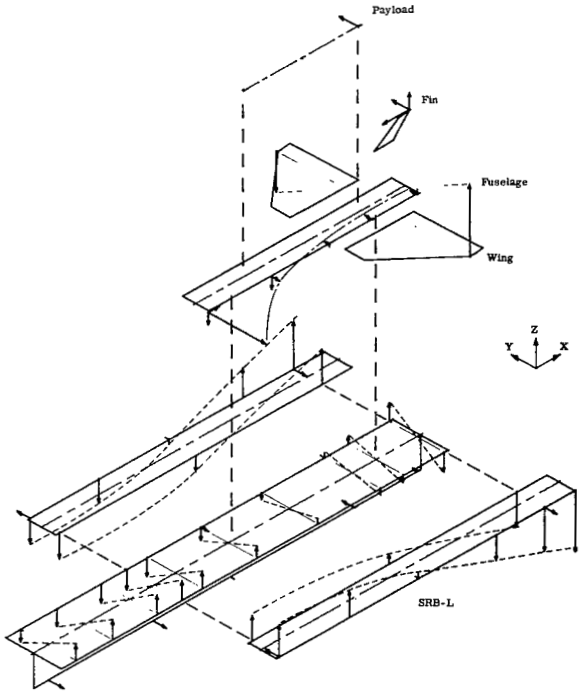

(i) 50.24 Hz, mode 13.

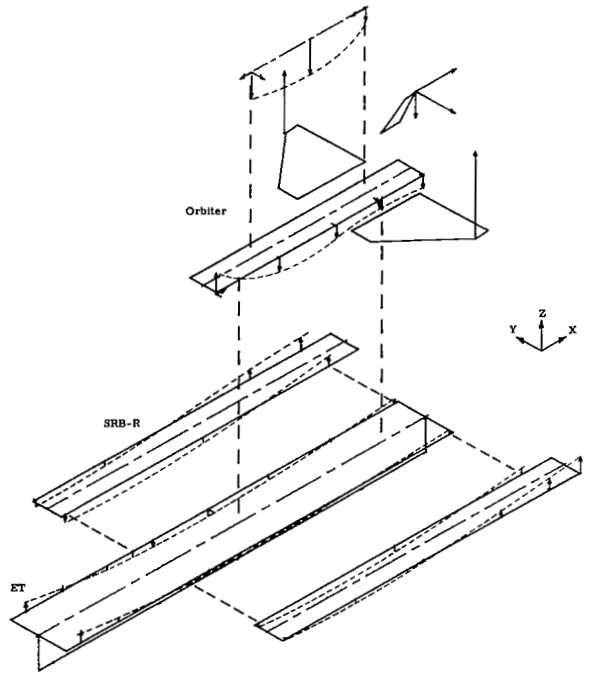

(j) 52.69 Hz, mode 14.

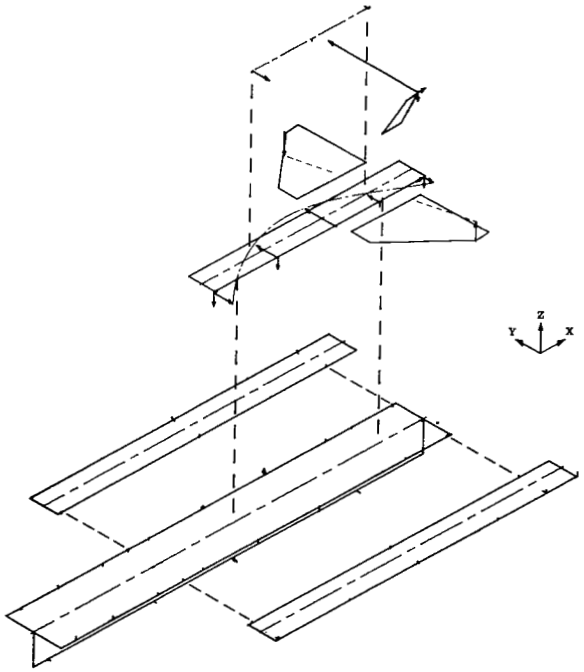

(k) 61.58 Hz, mode 15.

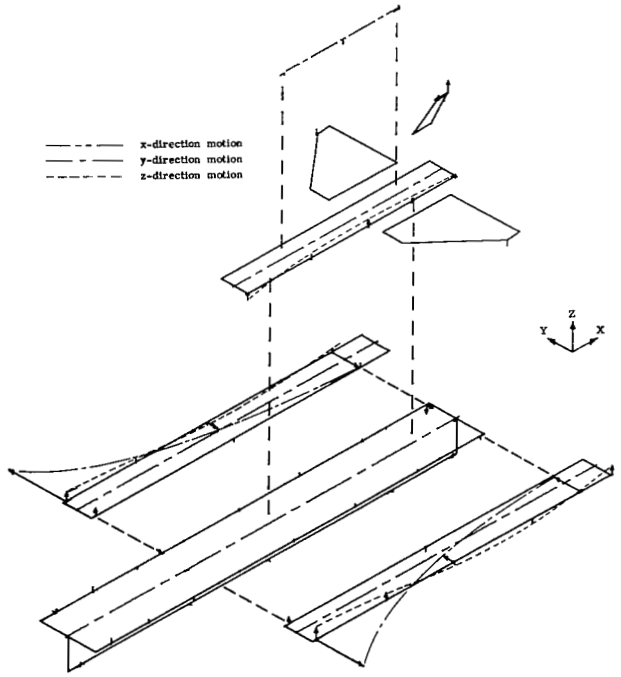

(l) 74.87 Hz, mode 16.

Figure 35.- Continued.

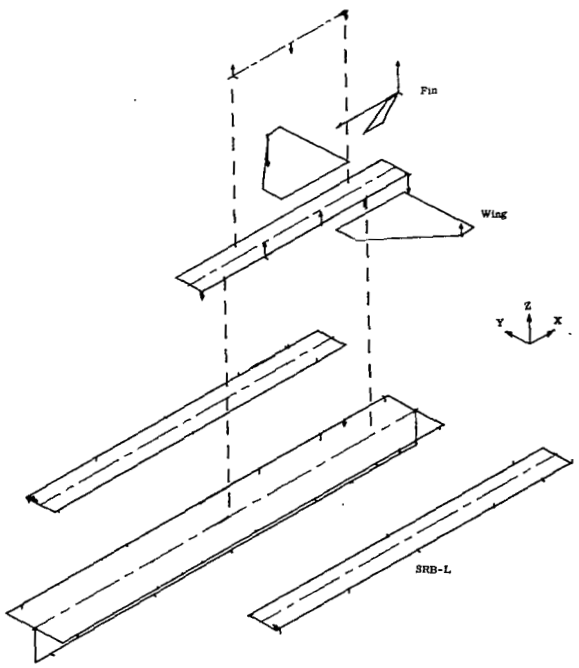

(m) 81.06 Hz, mode 17.

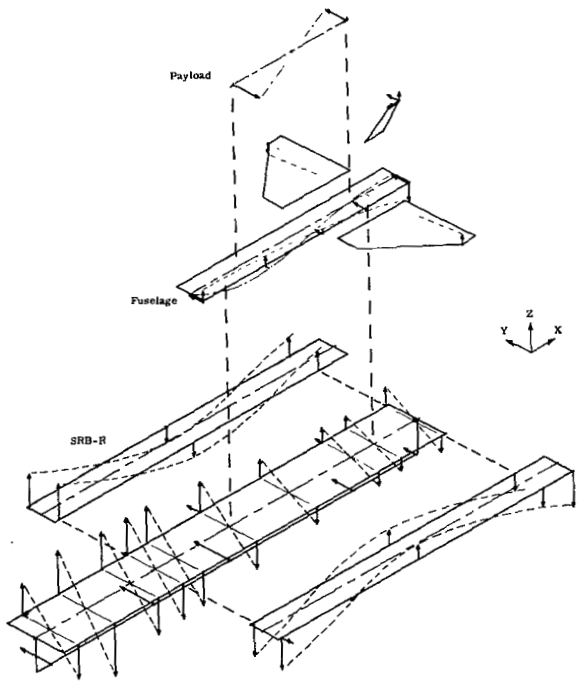

(n) 88.17 Hz, mode 18.

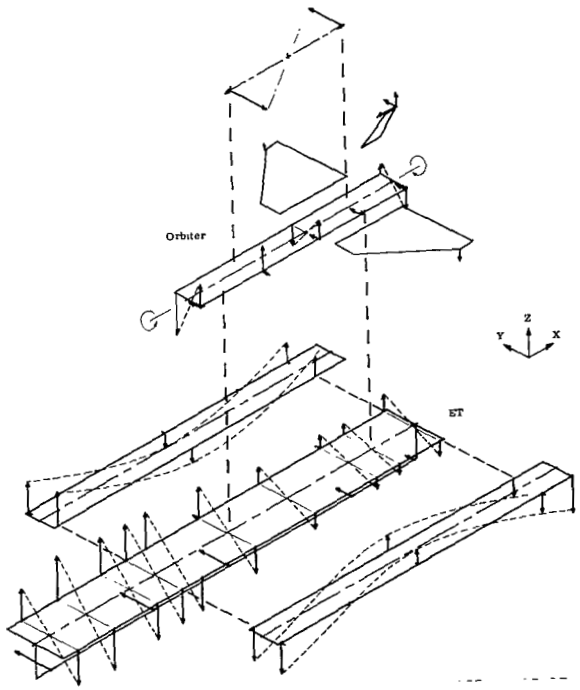

(o) 89.30 Hz, mode 19.

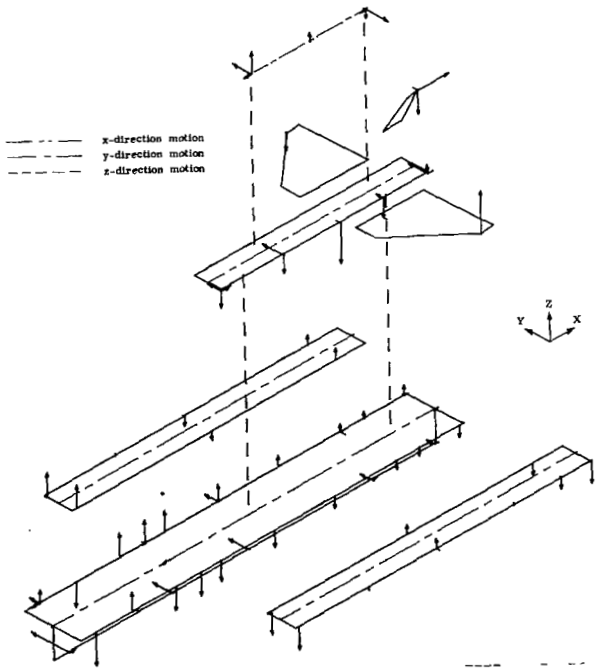

(p) 94.88 Hz, mode 20.

Figure 35.- Continued.

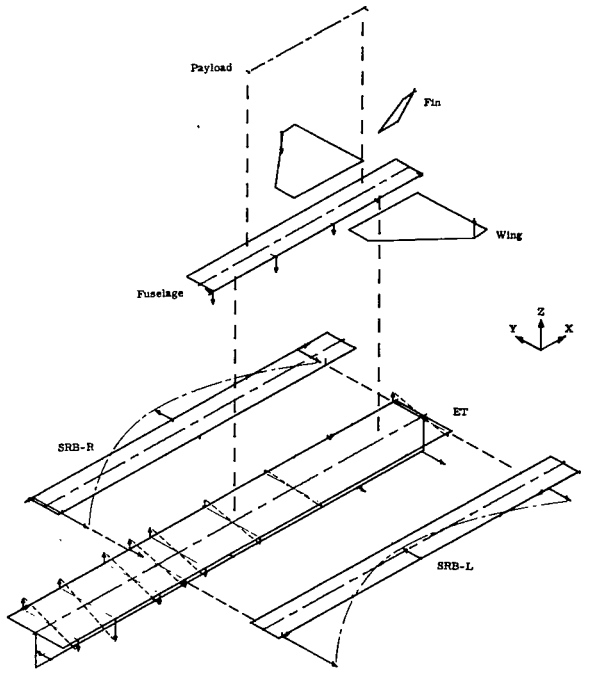

(q) 103.85 Hz.

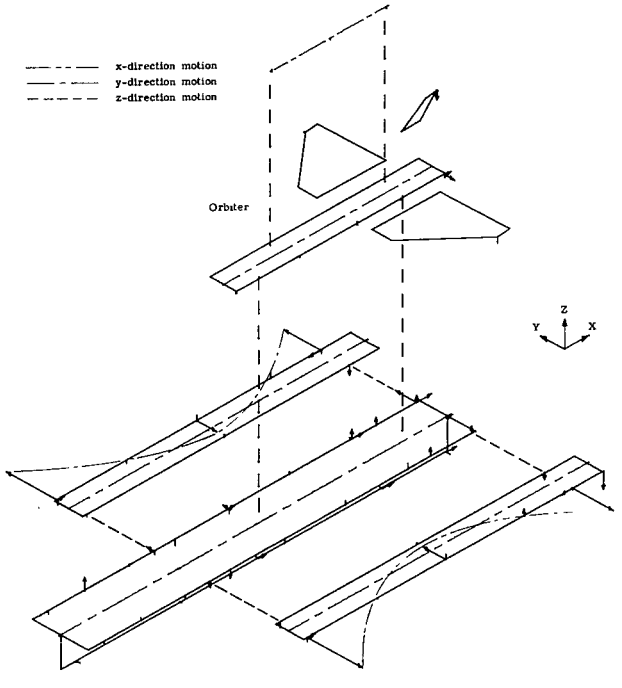

(r) 130.05 Hz.

Figure 35.- Concluded.

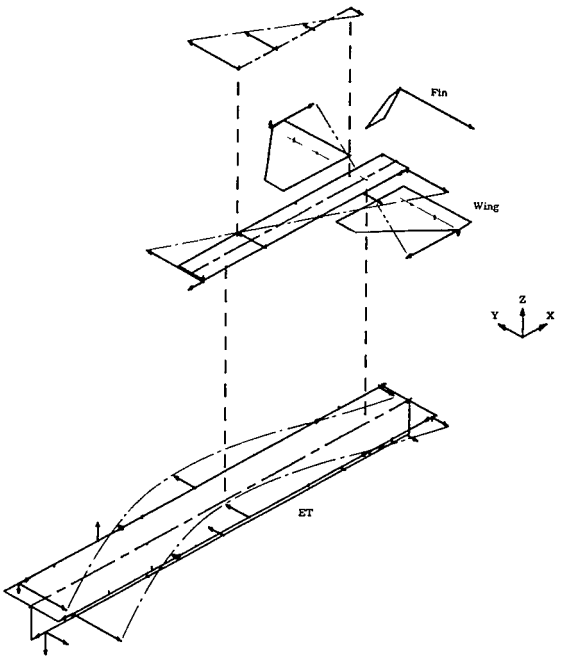

(a) 28.59 Hz, mode 2.

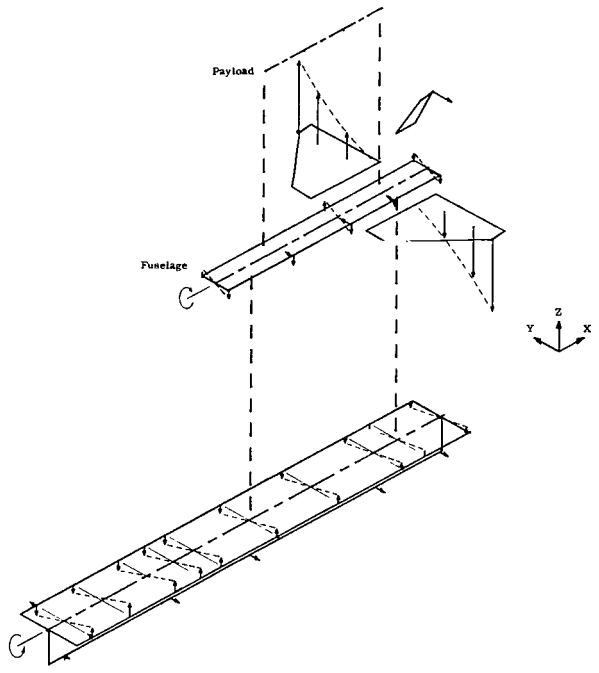

(b) 33.40 Hz, mode 4.

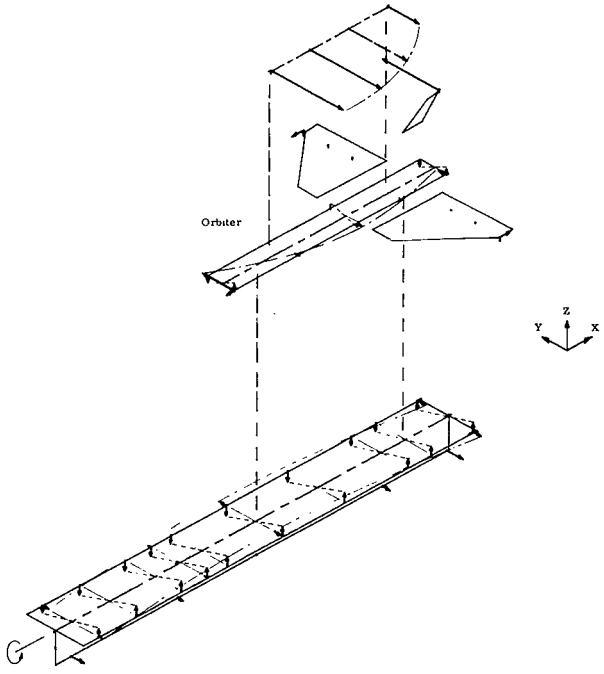

(c) 41.14 Hz, mode 5.

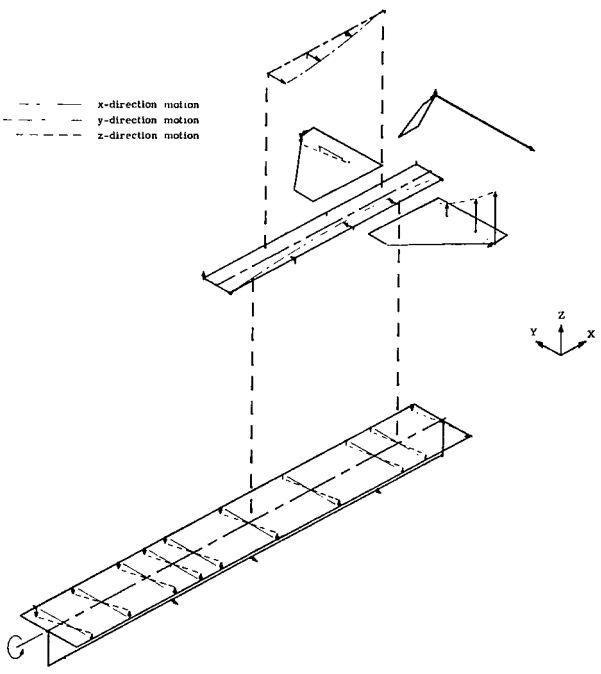

(d) 51.75 Hz, mode 8.

Figure 36.- Supplementary mode shapes for 1/8-scale shuttle model at end-boost (after SRB separation).

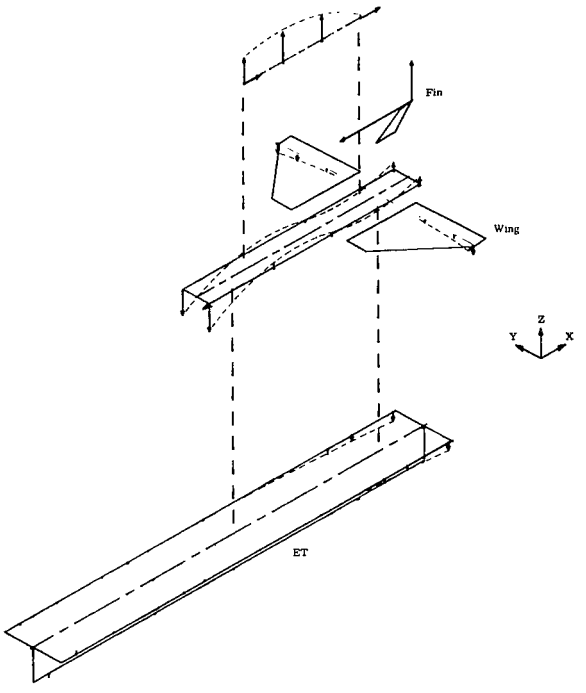

(e) 53.97 Hz, mode 9.

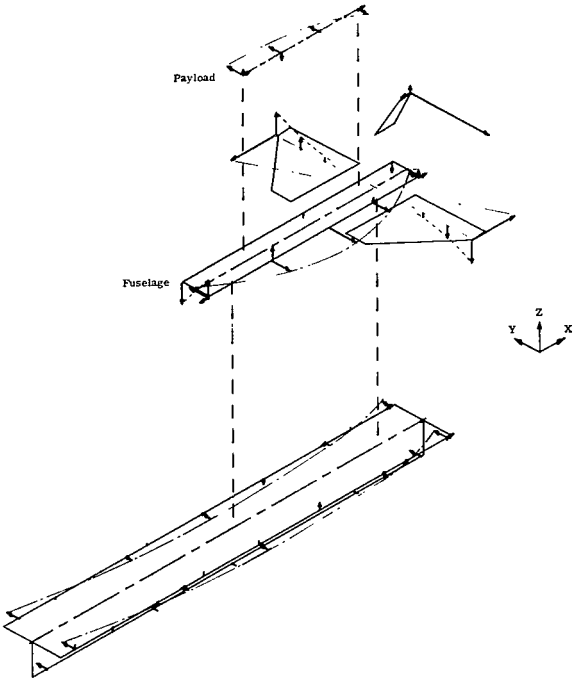

(f) 60.87 Hz, mode 10.

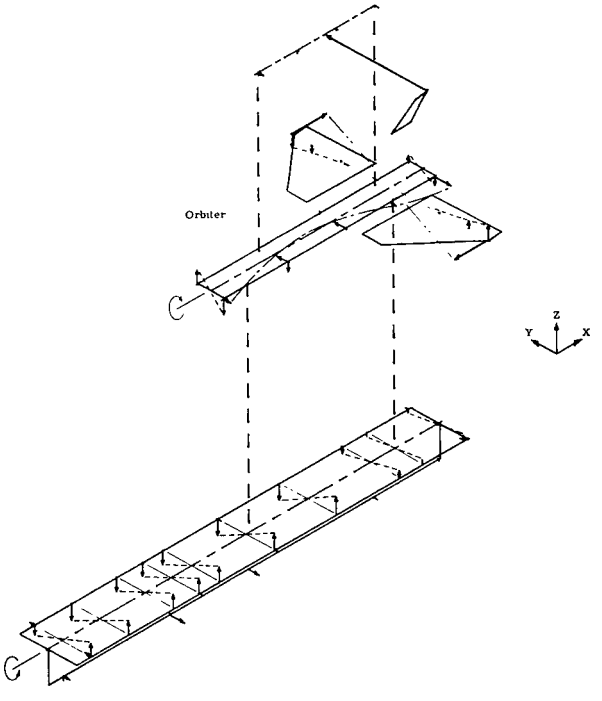

(g) 61.30 Hz, mode 11.

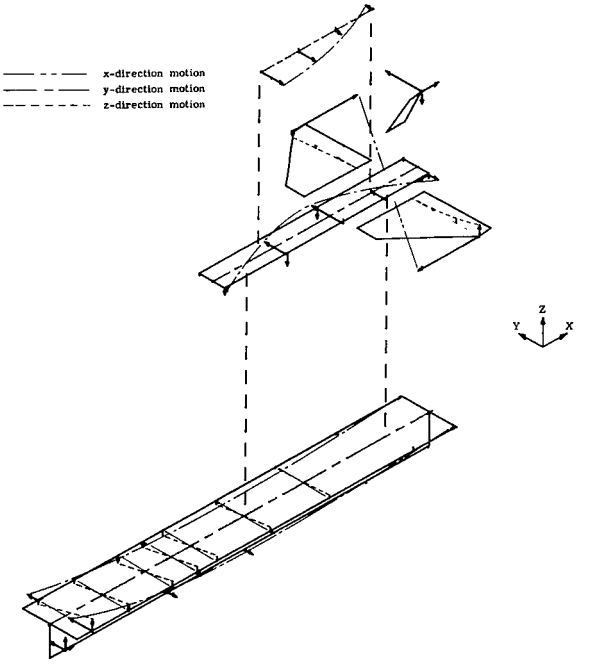

(h) 67.40 Hz, mode 12.

Figure 36.- Continued.

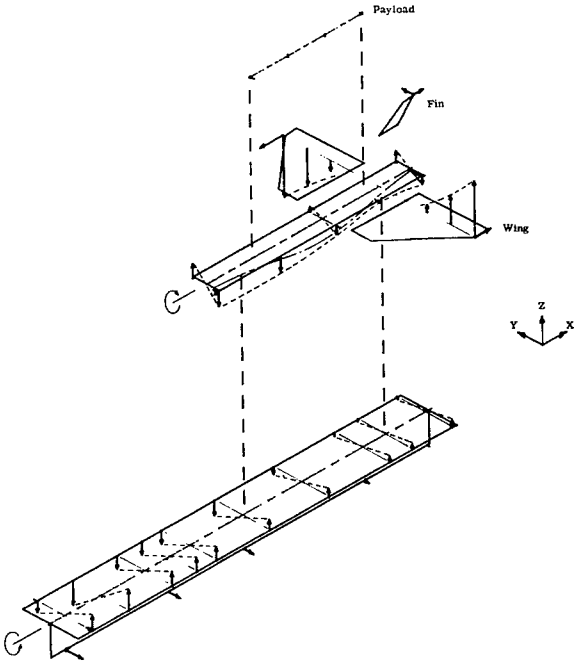

(i) 78.37 Hz, mode 13.

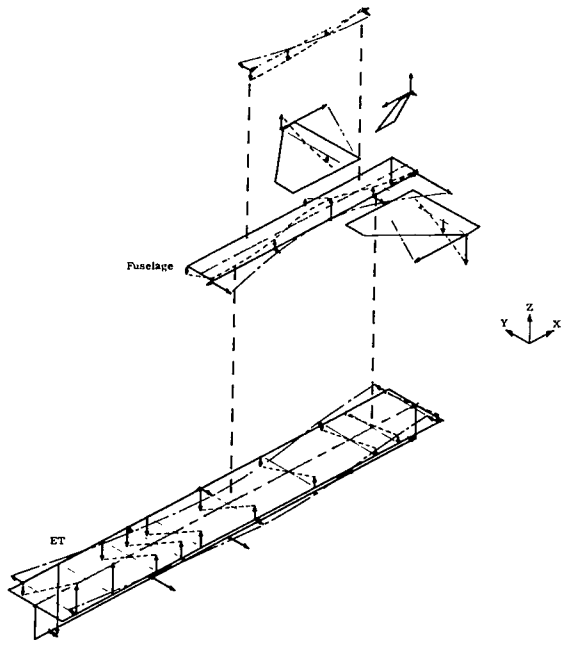

(j) 94.90 Hz, mode 16.

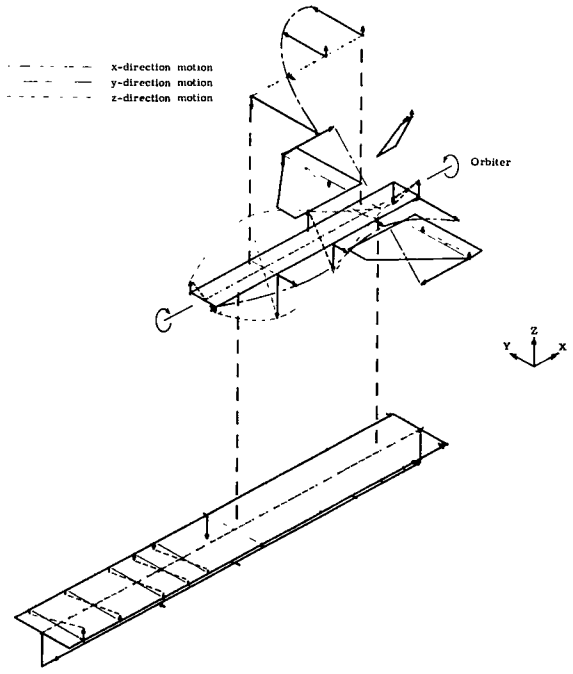

(k) 107.60 Hz, mode 17.

Figure 36.- Concluded.

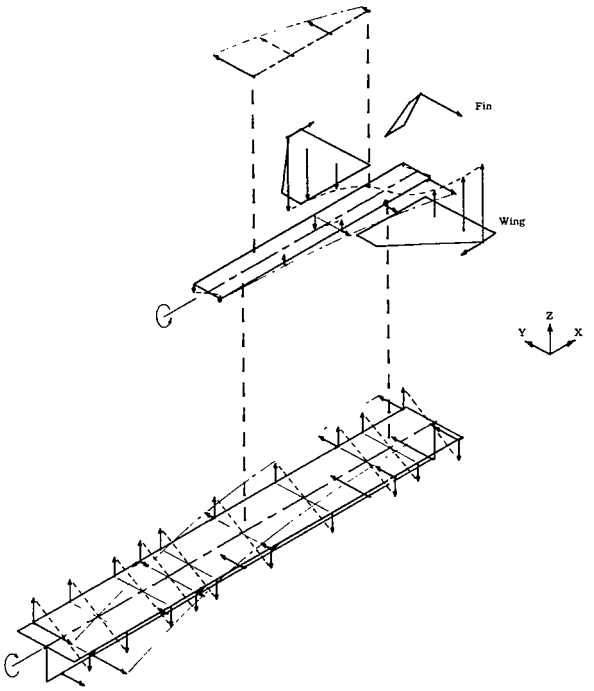

(a) 39.00 Hz, mode 3.

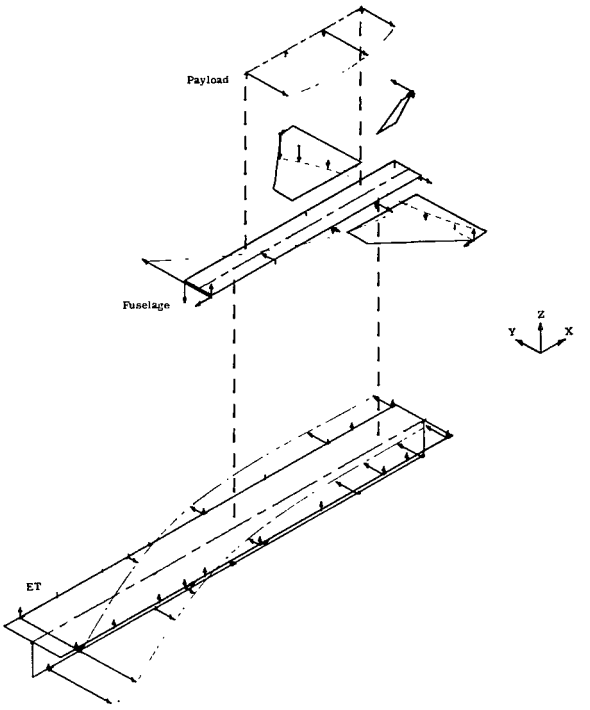

(b) 44.76 Hz, mode 5.

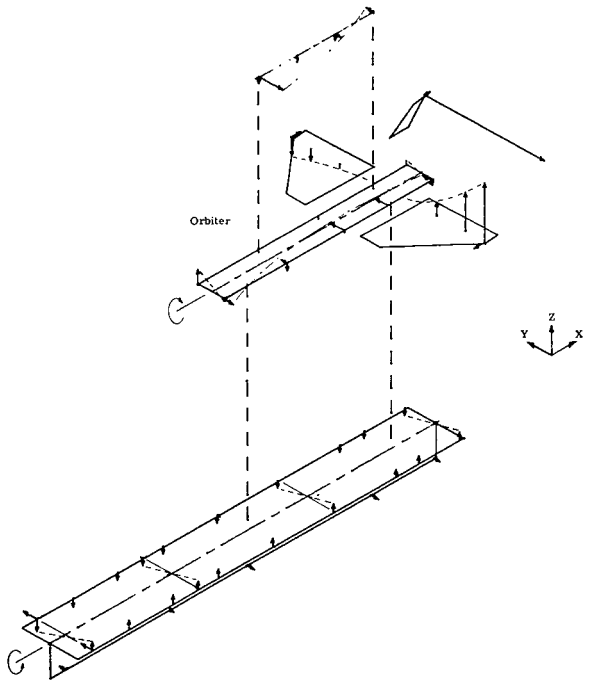

(c) 51.81 Hz, mode 7.

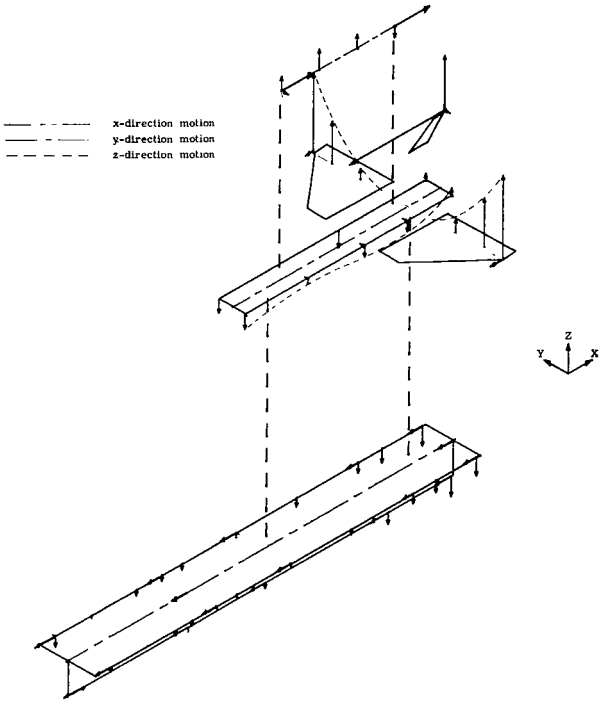

(d) 54.86 Hz, mode 8.

Figure 37.- Supplementary mode shapes for 1/8-scale shuttle model at end-burn (before ET jettison).

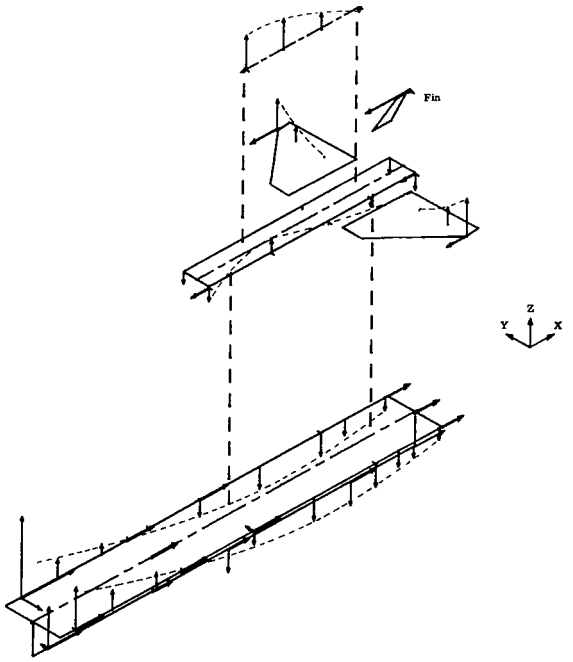

(e) 59.74 Hz, mode 9.

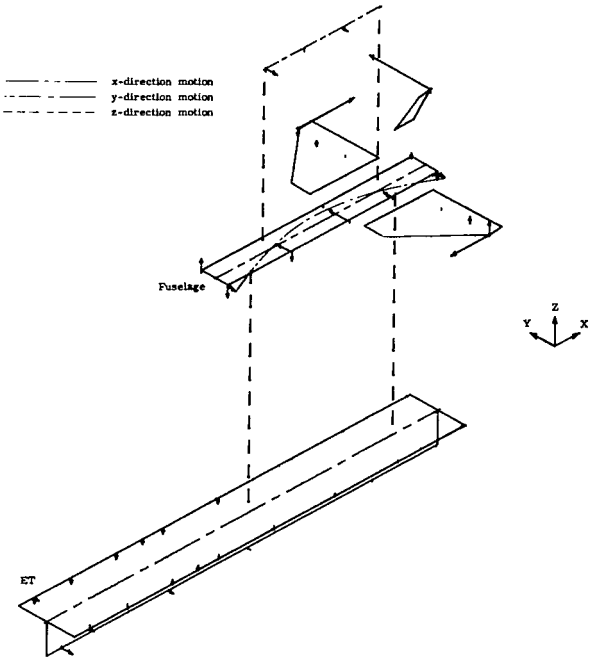

(f) 61.21 Hz, mode 10.

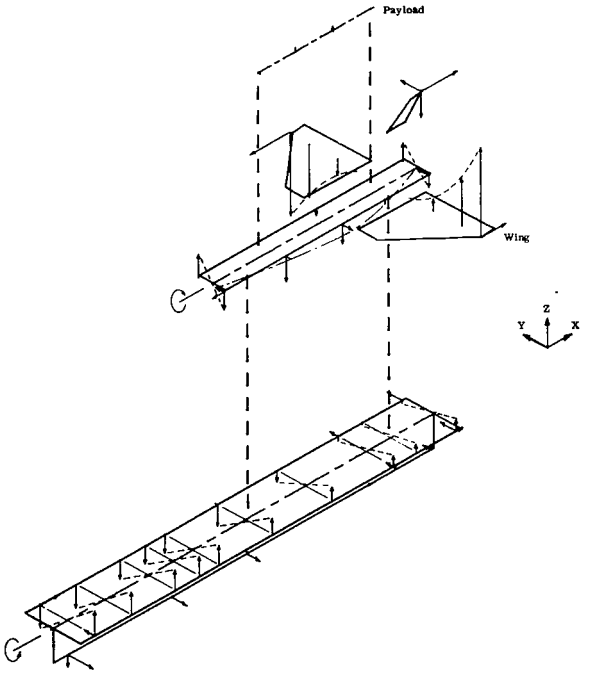

(g) 77.45 Hz, mode 13.

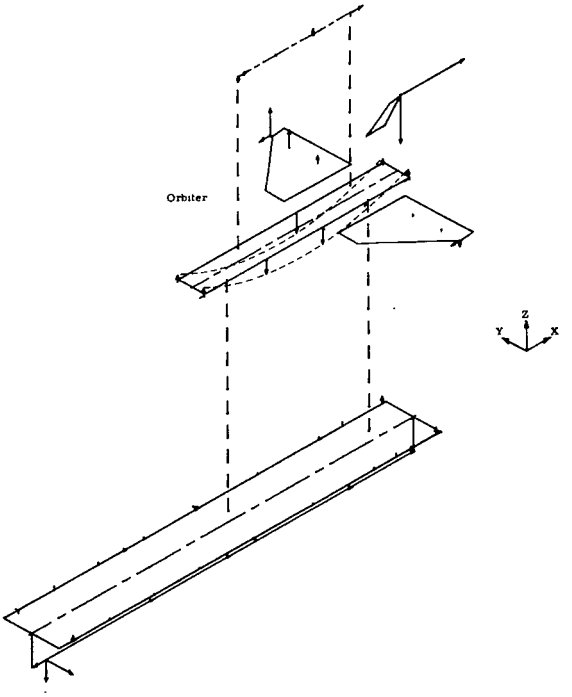

(h) 80.10 Hz, mode 14.

Figure 37.- Continued.

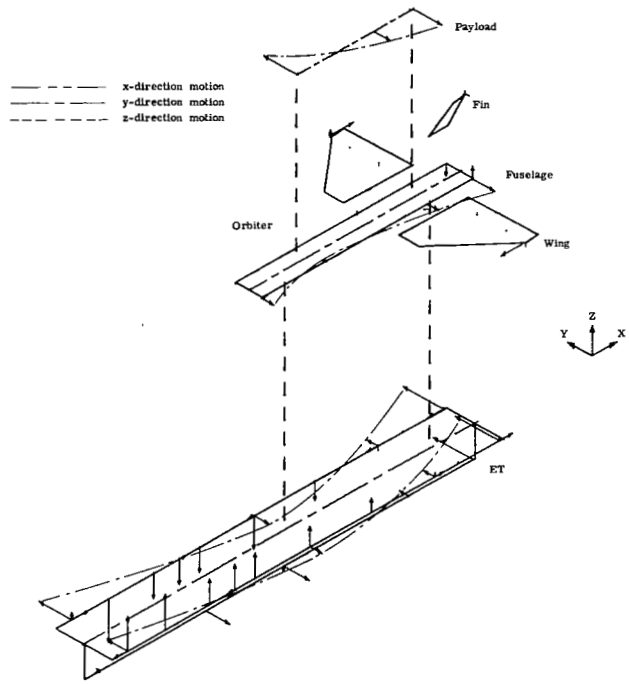

(i) 93.61 Hz, mode 15.

Figure 37.- Concluded.

577 C01 C1 U D 770819 S00903DS
DEPT OF THE AIR FORCE
AF WEAPONS LABORATORY
ATTN: TECHNICAL LIBRARY (SUL)
KIRTLAND AFB NM 87117

"The aeronautical and space activities of the United States shall be conducted so as to contribute . . . to the expansion of human knowledge of phenomena in the atmosphere and space. The Administration shall provide for the widest practicable and appropriate dissemination of information concerning its activities and the results thereof."

—NATIONAL AERONAUTICS AND SPACE ACT OF 1958

NASA SCIENTIFIC AND TECHNICAL PUBLICATIONS

TECHNICAL REPORTS: Scientific and technical information considered important, complete, and a lasting contribution to existing knowledge.

TECHNICAL NOTES: Information less broad in scope but nevertheless of importance as a contribution to existing knowledge.

TECHNICAL MEMORANDUMS: Information receiving limited distribution because of preliminary data, security classification, or other reasons. Also includes conference proceedings with either limited or unlimited distribution.

CONTRACTOR REPORTS: Scientific and technical information generated under a NASA contract or grant and considered an important contribution to existing knowledge.

TECHNICAL TRANSLATIONS: Information published in a foreign language considered to merit NASA distribution in English.

SPECIAL PUBLICATIONS: Information derived from or of value to NASA activities. Publications include final reports of major projects, monographs, data compilations, handbooks, sourcebooks, and special bibliographies.

TECHNOLOGY UTILIZATION PUBLICATIONS: Information on technology used by NASA that may be of particular interest in commercial and other non-aerospace applications. Publications include Tech Briefs, Technology Utilization Reports and Technology Surveys.

Details on the availability of these publications may be obtained from:

SCIENTIFIC AND TECHNICAL INFORMATION OFFICE

NATIONAL AERONAUTICS AND SPACE ADMINISTRATION

Washington, D.C. 20546